

**DIFFERENTIAL CROSS SECTION MEASUREMENT OF
Z BOSON IN LEPTONIC DECAYS AT $\sqrt{s} = 13$ TeV
WITH CMS DETECTOR AT LHC**

A THESIS

**Submitted to the
FACULTY OF SCIENCE
PANJAB UNIVERSITY, CHANDIGARH
for the degree of**

DOCTOR OF PHILOSOPHY

2018

RIDHI CHAWLA

**DEPARTMENT OF PHYSICS
CENTRE OF ADVANCED STUDY IN PHYSICS
PANJAB UNIVERSITY
CHANDIGARH, INDIA**

DEPARTMENT OF PHYSICS
Centre of Advanced Study in Physics
PANJAB UNIVERSITY, CHANDIGARH-160 014 (INDIA)

Fax: ++91-172-2783336




Phone: ++91-172-2541741


EPABX: ++91-172-2534466, 2534446

Email: casphypu.ac.in

CORRECTION CERTIFICATE

It is certified that there were no specific corrections recommended by the examiner of **Ms. Ridhi Chawla** in her Ph.D. thesis "**Differential Cross Section Measurement of Z Boson in Leptonic Decays at $\sqrt{s} = 13$ TeV with CMS Detector at LHC**". The thesis submitted by **Ms. Ridhi Chawla** in the present form, is acceptable.


(Prof. R.K. Puri)
Chairperson,
Dept. of Physics,
P.U., Chandigarh
Department of Physics
(Chairman)
Panjab University
Chandigarh-160014


(Prof. Manjit Kaur)
Department of Physics
P.U., Chandigarh
(Supervisor)

Acknowledgement

I take immense pleasure to acknowledge and extend my sincere gratitude to all those people who helped in building the foundation of my academic career and made this Ph.D. thesis a reality.

I thank the Almighty for granting me the wisdom, health and strength to undertake this research task and complete it within the target time period.

First and foremost I would like to express my heart-felt gratitude to my supervisor Prof. Manjit Kaur for guiding me through my research work and teaching many riveting aspects of particle physics. I appreciate all her efforts to make my Ph.D. experience productive and stimulating. The enthusiasm she has for research was motivational for me during the tough times. Her insightful comments and encouragement spurred me to widen the spectrum of my research to include various aspects. Her constant guidance, cooperation and support has always kept me going. I am grateful for the excellent example she has provided as a successful physicist and a professor. I owe a lot to her since she was always there for me and I feel privileged to be associated with a person like her during my research period.

I would like to thank my co-supervisor Prof. Slawomir Marek Tkaczyk for his constant motivation and support during the course of my research work. With his intelligent ideas and thought provoking discussions, I was able to make observations in the right direction and convert them to new possibilities.

I am extremely grateful to the present and former Chairpersons, Department of Physics, Panjab University, Chandigarh for providing academic support and adequate facilities to work in the department. I am highly obliged to the faculty members of PU-EHEP for creating a healthy working environment and generously sharing their time for useful discussions. I am thankful to the India-CMS Collaboration for organizing regular meetings and assisting me in the course of this work. I would like to thank the administrative and technical staff members who have been kind enough to advise and help me in their respective roles. I acknowledge the Department of Sci-

ence and Technology (DST), Government of India for providing with the necessary financial support through out the research period.

I extend my word of thanks to the CMS Collaboration for providing an excellent atmosphere to carry out research in the international community. I would like to thank all the members of CMS Standard Model group for their expert suggestions and useful discussions. I acknowledge Arun Kumar, Hwi Dong Yoo, Kyeongpil Lee, Ilya Kravchenko, Andrius Juodagalvis and other members of the Drell-Yan group who consistently extended their research expertise throughout my work. This research would have not been possible without their inputs. My heart-felt thanks to my fellow colleagues for always being helpful and providing their support through interactions at various points of my research program.

I take this opportunity to thank my confidant, Anterpreet Kaur for being there with me during the challenging period of my career. We share a special bond built with respect, care and understanding. My special gratitude to my companion Shabnam Thakur for being with me in thick and thin of life. She has always been an inspiration to me. I find myself lucky to have friends like them in my life.

Lastly, I feel deeply indebted to my parents Harish Chawla and Suman Chawla, who encouraged and helped me at every stage of my personal and academic life, and longed to see this achievement come true. I thank my brother Vaibhav Chawla and sister Surbhi Chawla for their unconditional love and support. A special acknowledgement goes to my fiance Aman Arora who has been a pillar of support in my journey. He shares a special place in my heart for being the most wonderful person I have ever known.

Date :

(Ridhi Chawla)

Abstract

The proton-proton collisions in the Large Hadron Collider built at the European Center for Nuclear Research is the beginning of a new era in high energy physics. It allows to test the predictions of the Standard Model with high precision and to search for new physics which has yet not been explored. The Drell-Yan process is one of the most fundamental Standard Model processes which occurs in high energy collisions. It proceeds via the exchange of virtual photon or Z boson when a quark anti-quark pair annihilates to produce a pair of oppositely charged leptons. The production cross section of the Drell-Yan process is established up to next-to-next-leading order accuracy and provides the very first validation of the Standard Model at this new energy arena. The Drell-Yan process is an irreducible background for various searches beyond the Standard Model, including the high-mass dilepton resonance, Higgs and other exotica searches, which makes it necessary to accurately measure the production cross section of the Drell-Yan process with the new collider data.

In this thesis, the first measurement of the Drell-Yan process is reported in dielectron final state at the center-of-mass energy $\sqrt{s} = 13$ TeV. The differential cross section is obtained using the proton-proton collision data collected by the Compact Muon Solenoid experiment during the year 2015. The analyzed data corresponds to an integrated luminosity of 2.3 fb^{-1} . The cross section measurement is performed in the bins of dielectron invariant mass in the range $15 < m < 3000$ GeV. The measured yield is corrected for the migration effects due to limited detector resolution, coverage of detector, selection inefficiencies and the final state radiation effects. The experimental cross section is computed in the full phase space and within the detector acceptance region. The corrected results are compared with various theoretical predictions of the Standard Model available at next-to-leading order and next-to-next-leading order.

Contents

List of Figures	xv
-----------------	----

List of Tables	xxv
----------------	-----

1	Introduction	1
2	Theoretical Framework	5
2.1	The Standard Model	5
2.1.1	Electroweak Theory	8
2.1.2	Quantum Chromodynamics	12
2.2	Proton-Proton Collisions	13
2.2.1	Parton Distribution Functions	14
2.2.2	Underlying Events and Pileup Contribution	16
2.3	Drell-Yan Production	17
2.3.1	Cross Section	18
2.3.2	Perturbative QCD Corrections	20
2.3.3	Electroweak Corrections	23
3	Experimental Details	25
3.1	The Large Hadron Collider	25

3.1.1	LHC Design	26
3.1.2	Luminosity and Machine Parameters	28
3.1.3	The Compact Muon Solenoid	29
3.1.4	Coordinate Conventions	31
3.1.5	Superconducting Magnet	33
3.1.6	Inner Tracking System	33
3.1.7	Electromagnetic Calorimeter	36
3.1.8	Hadron Calorimeter	39
3.1.9	Muon System	43
3.1.10	Trigger System	45
3.1.10.1	Electron Triggers	48
4	Event Simulation and Reconstruction	49
4.1	Event Generators	50
4.1.1	MADGRAPH	51
4.1.2	PYTHIA	51
4.1.3	POWHEG	52
4.2	Detector Simulation	52
4.3	Event Reconstruction	53
4.3.1	Primary Vertex Reconstruction	54
4.3.2	Pileup Corrections	55
4.3.3	Electron Reconstruction	56
4.3.3.1	Clustering	57
4.3.3.2	Track Reconstruction and Charge Determination	59
4.3.4	Energy Scale	60
4.3.5	Electron Selection Strategy	61

4.3.5.1	Identification	61
4.3.5.2	Isolation Requirement	62
4.3.6	Software and Computing	64
4.3.6.1	CMSSW	64
4.3.6.2	ROOT	64
4.3.6.3	Computing Model	65
5	Measurement of Drell-Yan Differential Cross section	67
5.1	Data and Monte-Carlo Samples	68
5.1.1	Collision Data	68
5.1.2	Drell-Yan Signal	68
5.1.3	Background Processes	70
5.2	Reweightings	74
5.2.1	Pileup Reweighting	74
5.2.2	Scale Corrections	75
5.3	Drell-Yan Event Selection	76
5.4	Background Estimation	80
5.4.1	Measurement of Dielectron Background using $e\mu$ Method	81
5.4.2	Measurement of Dielectron Background using Fake Rate Method	85
5.5	Corrections	91
5.5.1	Unfolding	92
5.5.2	Acceptance and Efficiency	94
5.5.3	Selection Efficiency	95
5.5.3.1	Reconstruction Efficiency	97

5.5.3.2	Identification and Isolation Efficiency	97
5.5.3.3	Trigger Efficiency	98
5.5.4	Final State Radiation Effects	100
5.6	Systematic Uncertainties	101
5.6.1	Luminosity Uncertainty	101
5.6.2	Statistical Uncertainty	102
5.6.3	Scale Correction	103
5.6.4	Background Estimation	103
5.6.5	Detector Resolution	104
5.6.6	Acceptance Correction	105
5.6.7	Efficiency Correction	105
5.6.8	FSR Correction	107
5.6.9	Total Uncertainty	107
5.7	Results	109
5.7.1	Z -peak Cross Section Measurement	109
5.7.2	Differential Cross Section Measurement	110
5.7.2.1	Dielectron Channel	110
5.7.2.2	Combined Channel	114
6	Summary	119
7	Hardware and Software Activities Undertaken	123
7.1	Upgrade of Hadron Outer Calorimeter	124
7.1.1	Silicon Photo Multipliers	124
7.1.2	SiPM Operation	125
7.1.2.1	Relative Variation in Gain	126
7.1.2.2	Relative Variation in Breakdown Voltage	126

7.2	HCAL Back-End Upgrade	127
7.2.1	MicroTCA	128
7.2.2	Testing of Power Mezzanines	129
7.3	Other Activities	130
Appendix A		133
A.1	A and R in data-driven $e\mu$ Method	134
A.2	Systematic Uncertainties	135
A.3	Full Phase Space Measurement	136
A.4	Fiducial Measurement	137
A.5	Full Phase Space Measurement	138
Bibliography		139
List of Publications		155
Reprint		161

List of Figures

2.1	The elementary particles of the Standard Model are presented along with their masses.	6
2.2	A symbolic representation of the DGLAP evolution equation for quark.	14
2.3	The parton distribution functions for quarks, anti-quarks and gluons for energy scale $Q^2 = 1.9 \text{ GeV}^2$ (left) and $Q^2 = 10 \text{ GeV}^2$ (right). The distributions are determined from global fits to data from the H1 and ZEUS Collaborations.	15
2.4	A schematic representation of $2 \rightarrow 2$ hard scattering event.	16
2.5	The Drell-Yan $q\bar{q} \rightarrow Z/\gamma^* \rightarrow l^+l^-$ production in a proton-proton collision. $P_{1,2}$ are the four-momenta of the protons, $p_{1,2}$ are the four-momenta of the partons which initiate the hard scattering, depending on the momentum fractions $x_{1,2}$	18
2.6	The leading order and next-to-leading order Feynman diagrams for the Drell-Yan process. The solid, spiral and wavy lines correspond to quarks anti-quarks, gluons and Z/γ^* , respectively.	21
3.1	Accelerator Complex at CERN. The protons originating from the hydrogen tank are injected into a series of accelerators which accelerate the protons step by step before getting introduced into the main ring.	27

3.2	Total integrated luminosity delivered by LHC and recorded by CMS at a center-of-mass energy $\sqrt{s} = 13$ TeV, during the year 2015.	29
3.3	A schematic diagram of the Compact Muon Solenoid. The detector consists of the inner tracker system, the calorimetry system, the muon identification system and a large superconducting magnet.	31
3.4	The CMS coordinate system is defined with respect to the LHC ring. The x-axis points inward towards the center of the ring, the y-axis points vertically upward and the z-axis points in the direction of the beam. The azimuthal angle ϕ is measured from the x-axis in the x-y plane where the radial coordinate is denoted by r. The polar angle θ is defined with respect to the z-axis in the r-z plane.	32
3.5	The CMS tracking system consists of Pixel detector and Silicon strip tracker comprising of Tracker Inner/Outer Barrel, Tracker Inner Disc and Tracker Endcap sub-detectors.	34
3.6	Tracker material thickness as a function of pseudorapidity η , expressed in relative radiation length x/X_0 of the different components of the tracker.	36
3.7	Layout of the CMS Electromagnetic Calorimeter which shows arrangement of the crystal modules, supermodules and endcaps along with the preshower detector.	37
3.8	Longitudinal view of CMS Electromagnetic Calorimeter which shows the barrel ($ \eta < 1.479$) and endcap ($1.479 < \eta < 3$) regions.	38
3.9	A quarter slice of the CMS Hadronic Calorimeter. The calorimeter is divided into three sub-detectors in barrel, endcap and forward regions and one sub-detector in the outer region, that lies outside the solenoid.	40

3.10	The CMS Muon system consists of Drift Tube, Cathode Strip and Resistive Plate chambers which are placed outside the solenoid magnet and embedded in the iron return yoke.	43
3.11	The CMS Trigger and Data Acquisition System consist of Level 1 and High Level Trigger.	47
4.1	Flowchart of the electron reconstruction chain.	56
4.2	Illustration of electron reconstruction. The electron candidate traverses the pixel and strip tracker, and deposits its energy in the electromagnetic calorimeter. The energy measured in the calorimeter is aligned in η but spread in the ϕ direction due to the axial magnetic field of the CMS detector.	57
4.3	Domino construction step in the Hybrid algorithm used in the barrel region of Electromagnetic Calorimeter.	58
4.4	The schematic overview of the CMS computing model. The data collected by CMS is stored in the Tier-0 site at CERN which is transferred to various Tier-1 centres. The reconstructed and simulated data is further distributed to Tier-2/3 sites, where it is available for physics analysis.	65
5.1	Leading order Feynman diagram of Drell-Yan process.	69
5.2	Generator-level mass distribution of the Drell-Yan signal sample. . . .	69
5.3	Leading order Feynman diagram for τ decay.	71
5.4	Leading order Feynman diagram for the $t\bar{t}$ pair production.	72
5.5	Leading order Feynman diagrams of the single top processes. From left to right: s-channel, t-channel and tW-channel.	72
5.6	Leading order Feynman diagram for diboson production contributions from s-channel (left) and t-channel (right).	73

5.7	Leading order Feynman diagram for W +jets production.	73
5.8	The distribution for number of reconstructed primary vertices in data (black circles) and Monte-Carlo prediction (stacked histograms) before (left) and after (right) applying the pileup reweighting.	75
5.9	The left and right plots show the mass distribution for the Z -peak region, before and after applying the energy scale and smearing corrections, respectively for data (black circles) and Monte-Carlo prediction (yellow histogram). The Drell-Yan signal is normalized to the number of data events.	76
5.10	Electron identification variables for data (black circles) and Monte-Carlo prediction (stacked histograms) listed in Table 5.3.	78
5.11	Electron kinematic variables p_T , η and ϕ after pre-selection (kinematic and identification cuts) in data (black circles) and Monte-Carlo prediction (stacked histograms).	79
5.12	Dielectron kinematic variables p_T , y and ϕ after pre-selection (kinematic and identification cuts) in data (black circles) and Monte-Carlo prediction (stacked histograms).	80
5.13	Drell-Yan mass distribution in data (black circles) and Monte-Carlo prediction (stacked histograms) in the dielectron invariant mass range 15 GeV to 3000 GeV.	81
5.14	Kinematic variables p_T , η and ϕ for electron (left) and muon (right) candidates after pre-selection (kinematic and identification cuts for $e\mu$ selection) in data (black circles) and Monte-Carlo prediction (stacked histograms).	83

5.15	Left: The number of observed e^+e^- events from Monte-Carlo prediction (stacked histograms) and the number of estimated e^+e^- events obtained from $e\mu$ MC (blacks circles). Right: The number of observed $e\mu$ events in data (black circles) and Monte-Carlo prediction (stacked histograms).	85
5.16	The number of observed e^+e^- events from Monte-Carlo prediction (stacked histograms) and the number of estimated e^+e^- events obtained from $e\mu$ data (blacks circles) using the $e\mu$ method.	86
5.17	E_T distribution of the HLT photon object before (red) and after (black) applying the trigger prescale. The distribution is common after $E_T = 175$ GeV, which is the maximum threshold of single photon trigger.	87
5.18	Electron fake rate obtained as a function of p_T in barrel and endcap regions, after performing the electroweak subtraction from Monte-Carlo prediction.	88
5.19	The number of dielectron events for QCD (left) and W +jets (right) backgrounds estimated from data using the fake rate method.	89
5.20	The observed dielectron invariant mass spectra for data (black circles) and Monte-Carlo (stacked histograms) events and the corresponding ratio of observed to expected yields. EW means the contribution from WW, WZ, ZZ and $DY \rightarrow \tau\tau$, Fakes correspond to the contribution from QCD and W +jets.	90
5.21	The fraction of the number of dielectron events from each background process with respect to the total observed number of data events. ‘Total’ corresponds to the combined fraction for all the backgrounds estimated from data-driven techniques and Monte-Carlo simulation.	91

5.22	The response matrix computed within the detector acceptance from aMC@NLO simulation to unfold the background subtracted yield. . .	93
5.23	Closure test: The comparison of measured (reconstruction-level) distribution and unfolded yield from Monte-Carlo simulation to the true (generator-level) distribution in bins of dielectron invariant mass using D'Agostini's iteration method with 21 iterations.	94
5.24	Detector acceptance, event efficiency and their product as a function of post-FSR dielectron invariant mass.	96
5.25	Reconstruction Efficiency in data and the corresponding scale factors obtained after dividing the efficiencies for data and Monte-Carlo simulation as a function of p_T (left) and supercluster η_{sc} (right). . . .	98
5.26	Electron Identification and Isolation Efficiency in data and the corresponding scale factors obtained after dividing the efficiencies for data and Monte-Carlo simulation as a function of p_T (left) and supercluster η_{sc} (right).	98
5.27	HLT Efficiency for the trigger <i>HLT_Ele23_WPLoose_Gsf</i> in data and the corresponding scale factors obtained after dividing the efficiencies for data and Monte-Carlo simulation as a function of p_T (left) and electron η (right).	99
5.28	The response matrix computed in full phase space from aMC@NLO simulation to correct for the Final State Radiation (FSR) effects using the iterative D'Agostini unfolding method.	101
5.29	Closure test: The comparison of generator-level (post-FSR) invariant mass distribution and FSR corrected unfolded yield from Monte-Carlo simulation to the dressed mass (pre-FSR) distribution in bins of dielectron invariant mass using D'Agostini's iteration method with 21 iterations.	102

5.30	The statistical, luminosity, acceptance and the total systematic uncertainties obtained in the bins of dielectron invariant mass.	108
5.31	The Drell-Yan differential cross section measurement corrected for radiation effects in full phase space as a function of dielectron invariant mass compared to the NNLO theoretical prediction from FEWZ (blue) and the NLO prediction from MADGRAPH5_AMC@NLO (red). The coloured band in the middle and bottom plots denotes theoretical uncertainty and the shaded band denotes total uncertainty which is the combination of statistical, systematic and luminosity uncertainties. . .	111
5.32	The Drell-Yan differential cross section measurement performed in the fiducial region without FSR correction as a function of dielectron invariant mass compared to the NLO theoretical prediction from MADGRAPH5_AMC@NLO. The red band in the bottom plot denotes theoretical uncertainty and the shaded band denotes total uncertainty which is the combination of statistical, systematic and luminosity uncertainties.	112
5.33	The Drell-Yan differential cross section measurement performed as a function of dielectron invariant mass compared to the NNLO theoretical prediction from FEWZ for the full phase space. The bottom plot shows the ratio between data and theoretical prediction where the coloured box denotes theoretical uncertainty.	113
5.34	Ratio of theory to experimental data for the differential cross section as a function of dielectron invariant mass in the range $m < 200$ GeV (left) and $m > 200$ GeV (right). The blue band denotes the theoretical uncertainty on the ratio. In the right plot, the contribution from Photon-Induced backgrounds is shown in red colour and has a visible effect in the high mass region.	113

5.35	Ratio between experimental result and theoretical prediction from various PDFs for $m > 200$ GeV. The coloured band in the plot denotes theoretical uncertainty and the shaded band denotes total experimental uncertainty.	114
5.36	The Drell-Yan differential cross section measurement performed as a function of combined invariant mass compared to the NNLO theoretical prediction from FEWZ for the full phase space. The bottom plot shows the ratio between data and theoretical prediction where the coloured box denotes theoretical uncertainty.	115
5.37	Ratio of theory to experimental data for the differential cross section as a function of combined invariant mass in the range $m < 200$ GeV (left) and $m > 200$ GeV (right). The blue band denotes the theoretical uncertainty on the ratio. In the right plot, the contribution from Photon-Induced backgrounds is shown in red colour and has a visible effect in the high mass region.	115
5.38	Ratio between experimental result and theoretical prediction from various PDFs for $m > 200$ GeV. The coloured band in the plot denotes theoretical uncertainty and the shaded band denotes total experimental uncertainty.	116
7.1	Photographs of the two sides of the Mounting Board.	125
7.2	Relative variation of the gain determined over time using the pedestal method for one Readout Module (18 channels).	126
7.3	Relative variation of the breakdown voltage determined over time using LED settings for one Readout Module (18 channels).	127

7.4	The μ TCA crate layout showing the data links from front-end electronics to the μ HTR cards, connections between the μ HTR cards and the calorimeter trigger and data acquisition system connected to the AMC13.	128
7.5	The set-up used for the testing of power mezzanines and auxiliary power mezzanines for a period of 39 hours. The communication between the test board and the computer is enabled through SUB-20 module via I2C protocol.	130
7.6	The power mezzanine (PM/AMP) testing set-up installed at the Department of Physics, Panjab University (Chandigarh).	131
7.7	The plots show the total luminosity delivered by LHC, recorded by CMS and certified as good for physics analysis during the year 2016 (up) and 2017 (down). The luminosity validated for performing physics analysis corresponds to data recorded at center-of-mass energy $\sqrt{s} = 13$ TeV, with all sub-detectors and physics objects showing good performance.	132

List of Tables

2.1	The four fundamental interactions in physics and their properties. . .	7
5.1	Names of the single electron data samples used in the Drell-Yan analysis.	68
5.2	Names of the datasets and corresponding cross section values for the Monte-Carlo signal and background samples used in the Drell-Yan analysis.	70
5.3	Summary of Medium Working Point for the electron identification using cut-based approach in the barrel and endcap regions.	79
5.4	Summary of Tight Identification and Particle Flow Isolation for the selection of muon in the $e\mu$ method.	84
5.5	Total number of $e\mu$ and e^+e^- events observed in data and Monte-Carlo prediction and the estimated number of e^+e^- events from data and Monte-Carlo simulation, where all errors are statistical.	85
5.6	Total number of dielectron events observed in Monte-Carlo prediction and the estimated number of dielectron events from data.	89
5.7	Tag and Probe selection criteria for measuring the Identification and Isolation efficiency.	99
5.8	Absolute cross section measurements in full phase space and fiducial region (within the detector acceptance) for the Z -peak region $60 < m < 120$ GeV along with the associated uncertainties.	110

A.1	The values of A and R obtained as a function of dielectron invariant mass. These numbers are used to estimate the true dielectron backgrounds from the data-driven $e\mu$ method by using the formulae described in Sec. 5.4.1.	134
A.2	Systematic uncertainties for $d\sigma/dm$ measurement in the dielectron channel. ‘Total’ refers to the quadrature sum of all sources of uncertainties except for the uncertainty from the acceptance correction. . .	135
A.3	Full phase space $d\sigma/dm$ measurement in the dielectron channel. ‘Total’ refers to quadrature sum of statistical, experimental and theoretical uncertainties.	136
A.4	Fiducial $d\sigma/dm$ measurement in the dielectron channel. ‘Total’ refers to quadrature sum of statistical and experimental uncertainties. . . .	137
A.5	Full phase space $d\sigma/dm$ measurement in the combined channel. ‘Total’ refers to quadrature sum of statistical, experimental and theoretical uncertainties without luminosity uncertainty.	138

Chapter 1

Introduction

The field of high energy physics aims at understanding the fundamental constituents of matter and interactions between them to explain their behaviour. The knowledge of these constituents is important to describe the physical laws that shape our universe. In past centuries, the particle physicists discovered different theories, one of them being the most precise, which led to a remarkable description of the fundamental particles along with their dynamics. This theory was known as the Standard Model (SM) of particle physics. The SM has been well tested throughout the years by many high energy experiments. This model accurately describes how everything observed in this universe is made from fundamental particles called the fermions categorized into quarks and leptons. These particles interact via four fundamental forces namely gravitation, electromagnetism, strong and weak. The carriers of these forces called the vector bosons govern the interaction between the matter particles.

Despite being the most well described and successful theory, the SM is inconsistent with some of the existing observations, which points to the possibilities of physics searches beyond the Standard Model (BSM). In order to describe new physics, accurate calculations obtained using well defined theories need to be compared to experimental measurements performed at high center-of-mass energies. These theories illustrate the interactions between quarks via mediating gluons or

weak bosons, respectively known as the Quantum Chromodynamics (QCD) and the Electroweak theory. This led scientists to build the Large Hadron Collider (LHC) with a designed center-of-mass energy of 14 TeV. To establish the non-SM outcomes at this collider experiment, it is essential to validate the predictions of the SM at new energy regime. This is done by studying the already known and well understood Drell-Yan (DY) process, which is one of the most important SM processes. It occurs in high energy hadron-hadron collisions when a quark and an anti-quark annihilate to produce a pair of oppositely charged leptons in s -channel¹ via the exchange of virtual photon or Z boson. The DY production cross section has been measured by the D0 and CDF experiments at the Tevatron [1]. The precise prediction of the DY production rate can be used as a confirmation of the SM at high energies.

The study of production of lepton pairs offers many interesting and important features of SM at the hadron colliders. Theoretical calculations of the differential cross section of DY processes are well established and a comparison with experimental measurements allows for the tests of perturbative QCD. The measurement also provides useful constraints on the parton distribution functions (PDFs) of the proton which help in the tuning of parameters in theoretical calculations for various tools like “Fully Exclusive W and Z production” (FEWZ) [2]. The observed forward-backward asymmetry of the charged leptons which arises in DY lepton pairs due to vector and axial-vector couplings can be potentially used as an input to the PDF fits from data. These measurements will eventually lead to a more precise determination of weak mixing angle [3]. In addition, the lepton-pair production from the DY process is a major source of background for the top quark measurement and various diboson physics analyses as well as for BSM searches which include the Z' resonance searches, providing the indications of extra dimensions.

The reasonably large production cross sections for leptonic final states at the LHC, can be used for the commissioning of physics tools as well as for the tuning

¹ s -channel represents a scattering process in which the two incoming particles join into an intermediate particle that consequently decays into two outgoing particles.

of Monte-Carlo methods. The DY process in muonic and electronic final states, can be used for the momentum and energy scale calibrations through the Z boson mass measurement ($m_Z = 91.2$ GeV). Hence, a precise knowledge of the DY cross section at the LHC is crucial to establish the predictions of the SM as well as for new physics searches BSM.

The measurement of differential cross section $d\sigma/dm$ was first performed at the LHC with 7 TeV [4, 5] data within the invariant mass range $15 < m < 600$ (1500) GeV in 13 (40) variable width mass bins, providing a precise measurement in the low mass and Z -peak regions. Another measurement was performed at 8 TeV [6], which extended the mass range to 2000 GeV. Additionally, the double differential cross section measurement $d^2\sigma/dmd|y|$ was performed over the mass range $20 < m < 1500$ GeV in 6 variable width mass bins and absolute value of the dilepton rapidity $0 < |y| < 2.4$ in 24 rapidity bins of width 0.1, at 7 TeV and 8 TeV center-of-mass energies. The single differential cross section measurement was performed in both dimuon and dielectron final states at the two energies. However, the double differential cross section measurement at 7 TeV was performed only in dimuon final state, while at 8 TeV the measurement was performed with both final states. The mass range was further extended from 2000 GeV to 3000 GeV to study the differential cross section in the dimuon final state with 13 TeV [7] data.

In this thesis, the measurement of the DY differential cross section $d\sigma/dm$ is presented in the dielectron final state within the mass range $15 < m < 3000$ GeV in 43 variable width mass bins, using the data collected by the Compact Muon Solenoid (CMS) experiment at the LHC. The data correspond to an integrated luminosity of 2.3 fb^{-1} at a center-of-mass energy $\sqrt{s} = 13$ TeV during the year 2015. The measurement of the differential cross section in the bins of invariant mass allows to estimate the shape of the DY spectrum and a high electron energy resolution (up to TeV scale) results in a precise determination of the cross section. The differential cross section obtained in the dielectron channel is combined with

that in the dimuon channel [7], to obtain total cross section in the leptonic channel with a greater precision.

The present work is organized² into seven chapters, with a brief introduction of each as described below:

Chapter 2 describes the fundamental principles of the SM, theories which govern the interactions between elementary particles and other theoretical concepts that are relevant for performing the DY cross section measurement.

Chapter 3 gives an overview of the experimental apparatus, the LHC and the CMS along with their parameters. In this chapter, the CMS detector, its various sub-detectors and their construction have been discussed in detail. It also describes the trigger system and the central data acquisition system which are used to store data to be further analyzed by the physicists.

Chapter 4 presents the importance of simulation processes categorized into event generation and detector simulation. This chapter describes the reconstruction of physics objects via dedicated reconstruction algorithms, selection and identification of objects which are used in this analysis.

Chapter 5 describes the workflow of the analysis performed for the measurement of the DY differential cross section in the bins of invariant mass. This chapter discusses the event selection, background estimation using data-driven methods and various techniques used to correct the experimental data. It presents the cross section measurement and its comparison with various SM theoretical predictions.

Chapter 6 summarizes and concludes the DY differential cross section measurement presented in this thesis.

Chapter 7 provides the participation in various hardware and software activities.

²The physical units in this thesis are taken from the International System of Units (SI), including the non-SI units like electron volt (eV) and barn (b). In accordance with special theory of relativity and quantum mechanics, the particle physics convention in which the speed of light c and the reduced Planck constant \hbar are set to unity is adopted, i.e. $c = \hbar = 1$.

Chapter 2

Theoretical Framework

The high energy processes provide the most crucial information about theoretical and phenomenological concepts of particle physics. The Standard Model is a powerful theoretical framework which well describes the observed phenomena in the universe. Various studies are performed to understand this model, amongst which the Drell-Yan (DY) process forms an essential part. This chapter describes theoretical concepts of the particle physics, physics behind the proton-proton collisions and the cross section measurement of the DY process.

2.1 The Standard Model

The Standard Model (SM) of particle physics [8–10] describes the fundamental constituents of matter, the elementary particles and the interactions between them. The first class of elementary particles is composed of spin- $\frac{1}{2}$ fermions, known as matter particles and the second class is formed by spin-1 bosons, known as gauge bosons which are the carriers of the fundamental interactions. In addition, the spin-0 particle, known as the Higgs boson is a key part of the SM that endows massive particles with their mass. Figure 2.1 gives an overview of the elementary particles and their properties which constitute the SM.




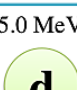








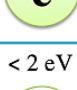
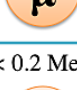



		Generations of Fermions (spin = ½)			Force Carrier Bosons (spin = 1)		
		I	II	III	weak force weak charge	electro-magnetic force (QED) electric charge	strong color force (QCD) color charge
Quarks	charge						
	+2/3 e	2.5 MeV 	1.29 GeV 	172.9 GeV 	0 e 91.2 GeV		
	-1/3 e	5.0 MeV 	100 MeV 	4.19 GeV 		0e; massless	
	-1 e	0.511 MeV 	106 MeV 	1.78 GeV 	$\pm 1 e$ 80.4 GeV		
Leptons	0 e	< 2 eV 	< 0.2 MeV 	< 18 MeV 			
					Higgs Boson (spin = 0) 		

Figure 2.1: The elementary particles of the Standard Model³ are presented along with their masses [11].

Elementary fermions are divided into three generations of quarks and leptons, each made up of a quark doublet and a charged lepton with an associated neutrino. The particles belonging to three generations have similar properties, except that the masses of the particles increase from lower to higher generation as well as within each generation. The quarks and leptons are classified according to their mass, electrical charge and quantum numbers. There are six different kinds of quarks called flavors arranged as - up and down (u, d); charm and strange (c, s); top and bottom (t, b). These carry fractional electrical charge of $+\frac{2}{3}$ or $-\frac{1}{3}$ times the charge of electron and each quark has an associated anti-particle called anti-quark which carries the same mass and spin, but an opposite charge. The quarks/anti-quarks can combine in doublets and triplets to form composite particles namely mesons ($q\bar{q}$) and baryons (qqq or $\bar{q}\bar{q}\bar{q}$) [12], respectively together known as hadrons. Quarks carry an additional charge known as color charge which comes in three forms - red (r), green

³Source : J. Hauptman, Particle physics experiments at high energy colliders.

(g) and blue (b). The hadrons which are formed by the combinations of quarks or anti-quarks are color neutral and hence, colored states are not observed. The three generations of leptons consists of electronic leptons (e, ν_e); muonic leptons (μ, ν_μ); tauonic leptons (τ, ν_τ) with six corresponding anti-particles called anti-leptons. The electron is the only stable lepton with a mass of 0.511 MeV [11], while the heavier leptons, muons and taus, eventually decay to electrons and neutrinos.

Table 2.1: The four fundamental interactions in physics and their properties.

Force	Range (in m)	Strength	Mediators (mass in GeV)	Participants
Strong	10^{-15}	$\alpha_s \approx 1$	8 gluon (0)	quarks and gluons
Weak	10^{-18}	$\approx 10^{-5}$	W^\pm, Z (80.94, 91.2)	quarks and gluons
Electron.	∞	$\alpha \approx \frac{1}{137}$	photon (0)	electrically charged particles
Gravity	∞	$\approx 10^{-39}$	graviton (0)	all particles

Each fundamental force is transmitted through force-carrying bosons, as described in Table 2.1. The strong nuclear force which is responsible for holding the nuclei together and binding together the quarks inside protons and neutrons, is mediated by the exchange of gluon (g). The electromagnetic force which acts between charged particles and is responsible for binding the electrons with the nuclei to form atoms is mediated by neutral photon (γ). The weak nuclear force which is responsible for radioactivity is mediated by massive W^\pm and Z bosons. The gravitational force which acts between all types of particles that have mass is mediated by a hypothetical graviton hence, not included in the SM yet. Quarks are the only fundamental particles which interact via all three SM forces, while leptons interact via electromagnetic and weak interactions only. The electromagnetic and strong interactions are described by theories known as Quantum Electrodynamics [13] and Quantum Chromodynamics [14,15], respectively while the electromagnetic and weak interactions can be merged into a single force by a theory called electroweak the-

ory [16, 17]. In 1970, physicists described a unified theory, called Grand Unification Theory (GUT) [18] which aimed at the unification of three fundamental forces of the SM, the electromagnetic, weak and strong interactions, at very high energies.

The SM is mathematically expressed using the local gauge theory which describes the unification of three forces based on symmetries. The Lagrangian corresponding to each fundamental interaction is invariant under the $SU(3)_C \times SU(2)_L \times U(1)_Y$ gauge symmetry group⁴. $SU(n)$ is the collection of all $n \times n$ unitary matrices that have determinant 1 ($U^\dagger U = I$, U^\dagger is the transpose conjugate). Here, $SU(3)_C$, $SU(2)_L$ and $U(1)_Y$ terms give rise to strong, weak and electromagnetic forces, respectively. $SU(2)_L \times U(1)_Y$ gauge group that corresponds to electroweak theory, could not explain the occurrence of massive weak gauge bosons. This phenomena was described by the Higgs Mechanism [19–21] which predicts the existence of the Higgs boson. The scalar boson named after Peter Higgs, provides mass to the fundamental particles by the spontaneous symmetry breaking of the electroweak group to electromagnetic subgroup,

$$SU(3)_C \times SU(2)_L \times U(1)_Y \rightarrow SU(3)_C \times U(1)_{QED} \quad (2.1)$$

The Higgs Mechanism explains the existence of massive vector bosons (W^\pm and Z) and the essential constituent of the SM, the Higgs boson. ‘4 July 2012’ marked the discovery [22, 23] of a new particle, found to be compatible with the properties of Higgs boson.

2.1.1 Electroweak Theory

The Quantum Electrodynamics (QED) is the quantum field theory which describes the electromagnetic interactions by the abelian gauge group $U(1)$. The local invariance under $U(1)$ leads to a massless vector boson γ .

⁴ C , L and Y represent color charge, left-handedness and weak hyper-charge, respectively.

The theory of electroweak (EW) interactions is a unified description of electromagnetic and weak interactions of the SM. Mathematically, the electroweak theory is described by the Yang-Mills⁵ model based on the non-abelian gauge group $SU(2)_L \times U(1)_Y$ which was proposed by S. Glashow, S. Weinberg and A. Salam. The hyper-charge⁶ operator, Y is the generator of $U(1)_Y$ symmetry. The $SU(2)_L$ group of weak isospin has three generators $T^{1,2,3}$ which satisfy the commutation relation,

$$[T^a, T^b] = if^{abc}T^c \quad (2.2)$$

where, f_{abc} are structure constants. The gauge field associated with the $U(1)$ is denoted by B_μ and couples via Y , while the gauge fields of the $SU(2)$ are $W_\mu^{1,2,3}$ and couple to left-handed fermions only.

The Lagrangian corresponding to the electroweak theory is defined as,

$$\mathcal{L} = \bar{\psi}i\gamma_\mu D^\mu - \frac{1}{4}B_{\mu\nu}B^{\mu\nu} - \frac{1}{2}\text{Tr}(W_{\mu\nu}W^{\mu\nu}) \quad (2.3)$$

here, ψ represents the Dirac field of a spin- $\frac{1}{2}$ particle. The first term in the Lagrangian describes the kinematics of the fermion field ψ , where D_μ , the gauge covariant derivative, ensures local invariance under the symmetry transformation $SU(2)_L \times U(1)_Y$. It is defined as⁷,

$$D_\mu = \partial_\mu - igW_\mu^a T^a + ig'B_\mu Y \quad (2.4)$$

The gauge fields W_μ^a and B_μ are massless vector fields and invariant under Lorentz transformation, where a runs over three generators of the $SU(2)$ group. Hence, if any mass term of the gauge fields is added to the Lagrangian, the local gauge invariance $SU(2)_L \times U(1)_Y$ will be violated.

⁵Yang-Mills theory is a gauge theory based on the $SU(n)$ group.

⁶ $Y = 2(Q - T^3)$, where Q is the electric charge and T_3 is the third component of weak isospin.

⁷ g and g' are respectively the gauge coupling constants of the $SU(2)$ and $U(1)$ groups.

In eq. 2.3, the second term describes the kinematics of the vector field B_μ . The field tensor $B_{\mu\nu}$ is invariant under gauge transformation, defined as,

$$B_{\mu\nu} = \partial_\mu B_\nu - \partial_\nu B_\mu \quad (2.5)$$

The field tensors of the $SU(2)$ group are also defined similarly, however they contain an additional term which arises due to the self-interaction of gauge fields in the non-abelian group,

$$W_{\mu\nu}^a = \partial_\mu W_\nu^a - \partial_\nu W_\mu^a + gf_{abc}W_\mu^b W_\nu^c \quad (2.6)$$

The gauge fields represent the mediator particles γ and W^\pm , Z of the electromagnetic and weak interactions, respectively. Thus, the Lagrangian of the EW theory describes the dynamics of fermions and gauge bosons, as well as the interactions between them. To preserve the local gauge symmetry, fermions and gauge bosons are predicted to be massless. The experimental evidence, however shows that the weak gauge bosons are massive. The mass generation mechanism is therefore, connected with the symmetry violation and requires extension in the model.

In order to generate masses for the weak gauge bosons, the Higgs mechanism which employs the concept of spontaneous symmetry breaking is used and introduces a massive scalar boson field corresponding to the Higgs particle.

The Lagrangian of this external scalar field ϕ is given by,

$$\mathcal{L}_\phi = |D_\mu \phi|^2 - V(\phi) - \frac{1}{4}F_{\mu\nu}F^{\mu\nu} \quad (2.7)$$

where, $F_{\mu\nu} = \partial_\mu A_\nu - \partial_\nu A_\mu$ represents the electromagnetic field tensor and describes the kinematics of gauge field A_μ . The self-interaction of the Higgs field is given by the scalar potential $V(\phi)$,

$$V(\phi) = \mu^2 \phi^\dagger \phi + \lambda(\phi^\dagger \phi)^2 \quad (2.8)$$

where, μ is a mass parameter and λ is a self-coupling constant. If $\mu^2 > 0$, $\lambda > 0$, then the potential has minima at the origin. However for $\mu^2 < 0$, $\lambda > 0$, we obtain a continuous set of minima at $\phi_1^2 + \phi_2^2 \equiv v^2$ and the symmetry can be broken with any particular choice of minima defined by non-vanishing vacuum expectation value,

$$|\phi_0|^2 = \frac{\phi_1^2 + \phi_2^2}{2} = -\frac{\mu^2}{2\lambda} \equiv v \quad (2.9)$$

The scalar field is quantized by expansion around the minima resulting in one massless and three massive bosons, the later known as Goldstone bosons [24]. Inserting the above expressions in eq. 2.7 results in mass eigenstates which correspond to gauge bosons, given by the orthogonal superposition of B_μ and W_μ^3 ,

$$W_\mu^\pm = \frac{1}{\sqrt{2}}(W_\mu^1 \mp iW_\mu^2), \quad Z_\mu = \frac{1}{\sqrt{g^2 + g'^2}}(g'W_\mu^3 - gB_\mu), \quad A_\mu = \frac{1}{\sqrt{g^2 + g'^2}}(g'W_\mu^3 + gB_\mu) \quad (2.10)$$

The masses of the gauge bosons are therefore given by,

$$m_W = g\frac{v}{2}, \quad m_Z = \sqrt{g^2 + g'^2}\frac{v}{2} \quad \text{and} \quad m_A = 0 \quad (2.11)$$

The mixing between the two neutral components of the gauge fields W_μ^3 and B_μ can be represented as,

$$A_\mu = B_\mu \cos\theta_W + W_\mu^3 \sin\theta_W, \quad Z_\mu = -B_\mu \sin\theta_W + W_\mu^3 \cos\theta_W \quad (2.12)$$

where, θ_W is the Weinberg or weak mixing angle. Using the above expressions, it can be shown that the masses of W and Z bosons are connected by the θ_W and represented as $m_Z \cos\theta_W = m_W$. More details on the theory of EW interactions can be found in [25].

2.1.2 Quantum Chromodynamics

The Quantum Chromodynamics (QCD) is the quantum field theory which describes the strong interactions based on the non-abelian gauge group $SU(3)$. This theory explains the interactions between six quark flavors ($f = u, d, s, c, b, t$) mediated by eight gluons. The particles effected by strong coupling need an additional color charge (r, g, b) in order to preserve the Pauli Exclusion principle.

The QCD Lagrangian can be described in analogy to eq. 2.3 as,

$$\mathcal{L} = \sum_{i=1}^{N_c} \sum_{f=1}^{N_f} \bar{q}_{fi} (i\gamma^\mu D_\mu - m_f) q_{fi} - \frac{1}{4} F_{\mu\nu}^a F^{a\ \mu\nu} \quad (2.13)$$

where, the sum runs over quark flavors N_f and all color states N_c . q_{fi} represents the quark fermion field. The last term describes the dynamics of the gluon field A_μ and contains triple and biquadratic gluon self-interaction terms $\sim A^3, A^4$ occurring due to the structure of non-abelian $SU(3)$ gauge group. This term is also known as Yang-Mills term,

$$\mathcal{L} = -\frac{1}{2} \text{Tr}(F_{\mu\nu} F^{\mu\nu}) = -\frac{1}{4} F_{\mu\nu}^a F^{a\ \mu\nu} \quad (2.14)$$

The field tensors in QCD, $F_{\mu\nu}^a$ can be described in analogy to eq. 2.6. The strength of the strong force is defined in terms of a coupling constant α_s which has a characteristic property of showing different behaviours in low and high energy regimes. At high energies i.e. shorter distances, force between the quarks decreases and they start behaving as free particles. As a result, α_s decreases due to self-interaction of gluons, which causes an anti-screening of color charge of the quarks. This phenomena is known as asymptotic freedom. While at low energies, the coupling is large due to stronger force between the quarks which confines them inside the hadrons. This effect is known as confinement. The strong coupling constant is

not a constant and acquires the name running coupling due to its dependence on the energy scale Q^2 . At leading order (LO), α_s can be written as [14],

$$\alpha_s(Q^2) = \frac{12\pi}{(33 - 2N_f) \ln \frac{Q^2}{\Lambda_{QCD}^2}} \quad \text{for } Q^2 \gg \Lambda_{QCD}^2 \quad (2.15)$$

where, the parameter $\Lambda_{QCD} \sim 200$ MeV has been determined experimentally. In the limit of asymptotic freedom $\alpha_s(Q^2 \rightarrow \infty) \rightarrow 0$, the cross section can be expanded in powers of α_s . In the limit of confinement, $\alpha_s(Q^2 \rightarrow \Lambda_{QCD}^2) \rightarrow \infty$, at a separation distance of the diameter of a hadron $\sim 10^{-15}$ cm, the strong interaction becomes so large that new quark anti-quark pairs are produced. These quarks and anti-quarks form mesons and baryons, collectively measured as hadrons inside a particle detector.

2.2 Proton-Proton Collisions

To determine the properties of elementary particles and to study BSM physics, large particle accelerators and particle detectors are utilized. The experiments at LHC study various processes occurring in proton-proton collisions at a high center-of-mass energy. The DY lepton pair production is an important process which is used to perform the tests of perturbative QCD (pQCD) [26, 27]. Prior to LHC, the DY production cross section was measured at the Tevatron by the D0 and CDF experiments and the results were compared to pQCD calculations [1, 28]. The LHC experiments, however, allow a precision measurement of the theory with increased center-of-mass energy than the previous collider experiments at Tevatron.

The physics of proton-proton collisions is complex and involves various fundamental processes. The parton model [29] is used to describe the structure of protons and their interactions inside colliding hadrons which defines the hard interaction. The factorization theorem [26, 27] of QCD, which will be discussed later in details,

allows to calculate the hard scattering cross section in hadron collisions and involves the information from parton model as an input. A parton radiates virtual gluons which can themselves emit gluons or produce quark anti-quark pairs, a process termed as parton showering. Eventually, hadronization occurs in which partons combine to form colorless hadrons. A collimated bunch of particles constituting hadrons is referred to as jets [30,31].

This section describes the structure of protons defined in terms of parton density functions and various processes which occur in proton-proton collisions.

2.2.1 Parton Distribution Functions

The proton is composed of elementary particles called partons, comprising three quarks (uud) referred to as valence quarks embedded in an infinite sea of quark anti-quark pairs (sea quarks) and gluons. The probability density of a parton i to carry a fraction x of proton's longitudinal momentum when probed at a momentum transfer scale Q^2 is defined as $f_i(x, Q^2)$. These functions are known as parton distribution functions (PDF) and can be extracted by fitting observables from experimental data using the Dokshitzer-Gribov-Lipatov-Altarelli-Parisi (DGLAP) evolution equations [32–34].

$$\frac{dq(x, Q^2)}{d \log Q^2} = \frac{q(y, Q^2)}{P_{qq}\left(\frac{x}{y}\right)} + \frac{g(y, Q^2)}{P_{qg}\left(\frac{x}{y}\right)}$$

Figure 2.2: A symbolic representation of the DGLAP evolution equation for quark. Taken from [35].

Figure 2.2 represents the DGLAP equation and expresses that the momentum

fraction of a quark, x in $q(x, Q^2)$, could have come from a parent quark or gluon with momentum fractions, y in $q(y, Q^2)$ or $g(y, Q^2)$ [35], respectively. The splitting function $P_{qq}(x/y)$ represents the probability of a quark to emit a gluon and become a quark with momentum reduced by a fraction x/y . Similarly, $P_{gq}(x/y)$ represents the probability of a gluon decaying to $q\bar{q}$ pair. In the DGLAP equation, the PDF, in terms of the probing energy scale $q(x, Q^2)$, is obtained by summing over all possible momentum fractions y ($> x$) of the parent multiplied by the split functions and the strong coupling constant.

The relevant PDF sets for LHC physics are CTEQ [36], MSTW [37], HERAPDF [38] and NNPDF [39, 40]. Figure 2.3 shows the PDFs of the partons at two different energy scales $Q^2 = 1.9 \text{ GeV}^2$ and $Q^2 = 10 \text{ GeV}^2$, calculated from fits to data from H1 and ZEUS experiments. It can be observed that, with increasing energy scale, the PDFs become significantly larger at small x , allowing to probe gluons and sea quarks at such smaller distances.

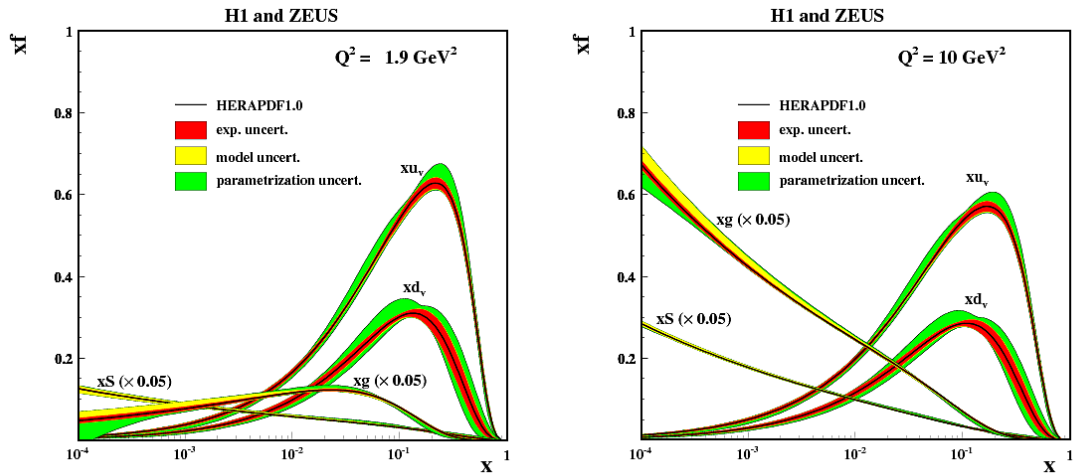


Figure 2.3: The parton distribution functions for quarks, anti-quarks and gluons for energy scale $Q^2 = 1.9 \text{ GeV}^2$ (left) and $Q^2 = 10 \text{ GeV}^2$ (right). The distributions are determined from global fits to data from the H1 and ZEUS Collaborations⁸.

⁸Source : <https://arxiv.org/abs/0911.0884>

2.2.2 Underlying Events and Pileup Contribution

The hadronic final states of proton-proton collisions consist of an overlay of several contributions [41], as shown in Fig. 2.4 which are not associated to the hard scattering process. These effects are referred to as soft scattering or Underlying Event (UE), a combination of soft parton radiation, additional parton scatterings and additional scatters of the beam remnants which are the leftovers of hard collision. The UE activity increases with an increase in the center-of-mass energy.

In addition, partons which initiate the hard process can emit additional partons in the initial state of a hadron collision, due to the presence of color charge. This process is known as initial-state radiation (ISR). Similarly, radiation is possible for the final-state partons emerging from multiple soft scatters after the hard scattering has occurred, known as final-state radiation (FSR). In the DY lepton pair production, the QCD effects enter only in the initial-state which provides an opportunity to study parton shower effects due to ISR [42].

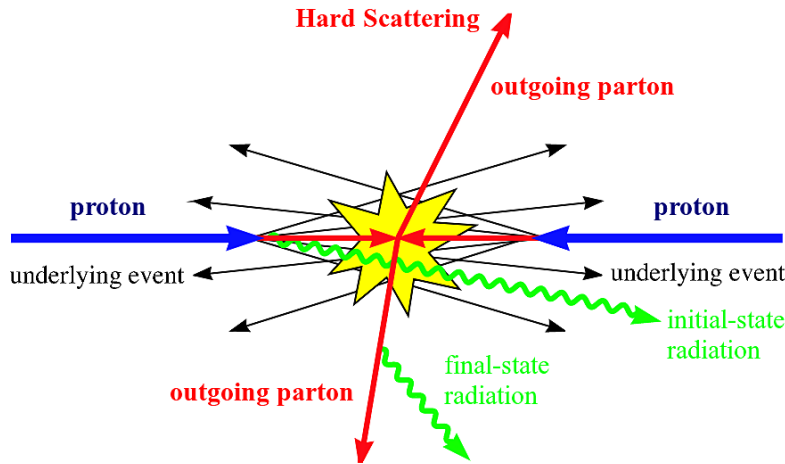


Figure 2.4: A schematic representation of $2 \rightarrow 2$ hard scattering event. Taken from [43].

In addition to the hard $2 \rightarrow 2$ parton-parton scattering, multiple parton scatterings of softer partons can occur, known as Multi Parton Interaction (MPI) [44].

This produces hadrons predominantly along the direction of the initial protons having smaller transverse momentum and hence, have a least effect on the physics observables. The phenomena is non-perturbative and leads to a substantial amount of soft particles which get added to the event content, hence require a proper modeling.

A beam in high energy colliders like LHC, is not a continuous string of particles, but divided into chunks which are few centimetres long and are known as bunches. The number of bunches is proportional to the luminosity in the collider. The nominal number of bunches in the LHC is 2808. Each bunch consists of about a hundred billion protons. The average number of events per bunch crossing depend on the total cross section, luminosity and bunch spacing. With a high total cross section for the minimum bias (MB)⁹ interactions, there is an increased probability of multiple proton-proton collisions. The additional energy from proton-proton interactions other than the hard-scatter event is called pileup. While pileup itself cannot be measured directly, it can be correlated to many other directly measurable quantities for e.g., the number of primary vertices (N_{PV}) is directly correlated to the amount of pileup; the greater the N_{PV} , the more pileup energy is added to the event.

2.3 Drell-Yan Production

The production of a lepton pair l^+l^- with invariant mass $m^2 = (p_{l^+} + p_{l^-})^2 \gg 1 \text{ GeV}^2$ by the annihilation of quark anti-quark pair is called Drell-Yan process. It was first described in 1970 by Drell and Yan [45]. In proton-proton collisions, the quark and anti-quark are constituents of the two incoming protons and can create an off-mass-shell virtual boson (Z or γ^*) as shown in Fig. 2.5, which directly decays into a lepton pair, immediately after its production. In the following section, the DY production cross section is first calculated using the parton model and then including the perturbative corrections, following the calculations in [14, 46].

⁹Minimum bias events are inelastic events selected by a high energy experiment's loose or minimum bias trigger with as little bias as possible.

2.3.1 Cross Section

In a high energy proton-proton collision, the process of hard scattering is initiated by two partons from the two colliding protons. Figure 2.5 describes an illustration for the production of a Z/γ^* resonance and its decay to a lepton pair. The square

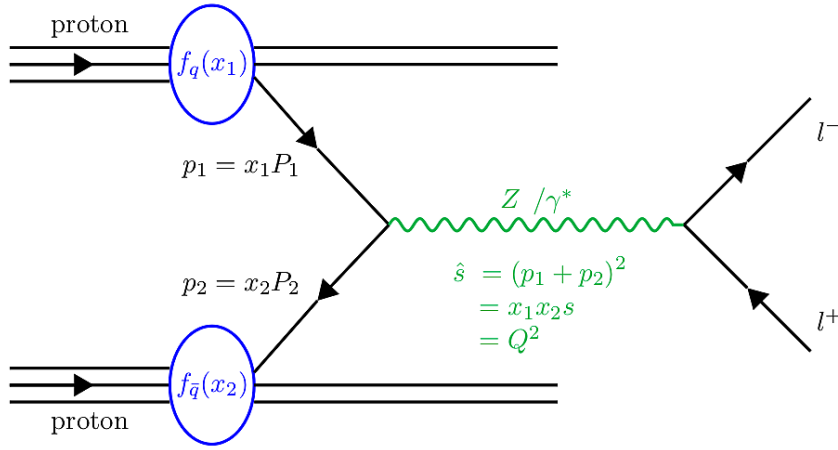


Figure 2.5: The Drell-Yan $q\bar{q} \rightarrow Z/\gamma^* \rightarrow l^+l^-$ production in a proton-proton collision. $P_{1,2}$ are the four-momenta of the protons, $p_{1,2}$ are the four-momenta of the partons which initiate the hard scattering, depending on the momentum fractions $x_{1,2}$. Taken from [14].

centre-of-mass energy of the proton-proton collision is given by,

$$s = (P_1 + P_2)^2 \quad (2.16)$$

where, P_i is the four-momentum of proton i , for $i = 1, 2$. In the collinear approximation [14], the four-momenta of the two partons can be obtained as,

$$p_1 = \frac{\sqrt{s}}{2}(x_1, 0, 0, x_1), \quad (2.17)$$

$$p_2 = \frac{\sqrt{s}}{2}(x_2, 0, 0, -x_2) \quad (2.18)$$

where, x_i represents the parton momentum fraction of parton i . The squared centre-of-mass energy of the parton scattering is obtained as,

$$\hat{s} = (p_1 + p_2)^2 = x_1 x_2 s = m_{l^+ l^-}^2 = Q^2 \quad (2.19)$$

The cross section of a QCD process can be calculated by using the collinear factorization theorem [47]. The theorem states that the cross section can be divided into two parts: the hard interaction between two colliding partons and the corresponding PDFs. This theorem, therefore, separates the short-distance contributions which can be calculated perturbatively and include QCD radiations, and the long-distance contributions including hadronization, PDF and soft interactions, which cannot be calculated in pQCD and require phenomenological models [43] for precise determination. Hence, the total cross section can be written as the convolution of hard scattering cross section and PDFs of colliding partons.

The DY production cross section in the proton-proton collisions is obtained by weighting the partonic cross section $\hat{\sigma}$ for the sub-process $q\bar{q} \rightarrow l^+ l^-$ with the PDFs $f_q(x_1)$ and $f_{\bar{q}}(x_2)$,

$$\sigma_{pp} = \sum_q \int dx_1 dx_2 f_q(x_1) f_{\bar{q}}(x_2) \hat{\sigma}_{q\bar{q} \rightarrow l^+ l^-} \quad (2.20)$$

where the sum runs over all combinations of quark anti-quark pairs and $\hat{\sigma}_{q\bar{q} \rightarrow l^+ l^-}$ is the cross section for the sub-process $q\bar{q} \rightarrow l^+ l^-$.

At lowest-order in pQCD, the cross section of $q\bar{q} \rightarrow l^+ l^-$ can be obtained as,

$$\hat{\sigma}_{q\bar{q} \rightarrow l^+ l^-} = \frac{4\pi\alpha^2}{3\hat{s}} \frac{1}{N_c} Q_q^2 \quad (2.21)$$

where, N_c ($= 3$) is the number of quark colors, $\alpha = \frac{e^2}{4\pi}$ is the electromagnetic coupling constant and Q_q is the electrical charge of the quark. The lepton pair can

be produced with different invariant masses which corresponds to the production of a virtual boson, $q\bar{q} \rightarrow Z/\gamma^* \rightarrow l^+l^-$, depending on the energy of the incoming quark anti-quark pair. Hence, the differential lepton pair invariant mass m distribution is obtained,

$$\frac{d\hat{\sigma}}{dm^2} = \frac{4\pi\alpha^2}{3m^2} \frac{1}{N_c} Q_q^2 \delta(\hat{s} - m^2) \quad (2.22)$$

The differential cross section of the lepton pair production in the DY process obtained from eq. 2.20, derived in the parton model gives,

$$\begin{aligned} \frac{d\sigma}{dm^2} &= \int_0^1 dx_1 dx_2 \sum_{q=1}^{N_f} \{f_q(x_1)f_{\bar{q}}(x_2) + f_{\bar{q}}(x_1)f_q(x_2)\} \frac{d\hat{\sigma}}{dm^2}(q\bar{q} \rightarrow l^+l^-), \\ &= \frac{4\pi\alpha^2}{3\hat{s}} \frac{1}{N_c} \int_0^1 dx_1 dx_2 \delta(x_1 x_2 s - m^2) \left[\sum_{q=1}^{N_f} \{f_q(x_1)f_{\bar{q}}(x_2) + f_{\bar{q}}(x_1)f_q(x_2)\} \right], \\ &= \frac{4\pi\alpha^2}{3\hat{s}} \frac{1}{N_c} \int_0^1 dx_1 dx_2 \delta(x_1 x_2 s - m^2) P_{q\bar{q}}(x_1, x_2) \end{aligned} \quad (2.23)$$

The sum runs over N_f quark flavours and the term $f_{\bar{q}}(x_1)f_q(x_2)$ represents the additional contribution arising from anti-quark quark pairs. The dependence on the PDFs is defined in the combined $q\bar{q}$ probability function $P_{q\bar{q}}(x_1, x_2)$ [46].

2.3.2 Perturbative QCD Corrections

The DY production cross section needs perturbative QCD corrections in order to account for the additional parton emissions in high energy hadron-hadron collisions. At the LO, only the quark anti-quark annihilation occurs $q\bar{q} \rightarrow Z \rightarrow l^+l^-$ which constitutes the dominant production of Z boson. However, at next-to-leading order (NLO), due to the initial-state gluon radiation, (anti)quark-gluon scatterings are

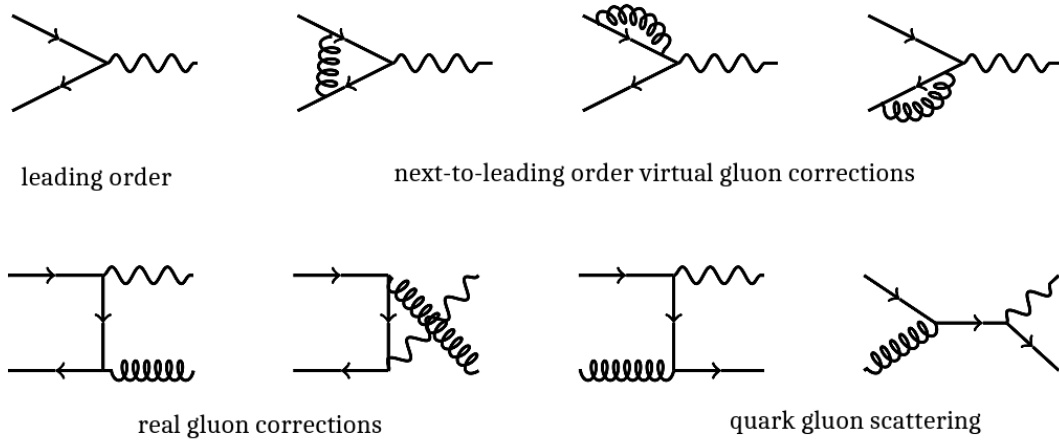


Figure 2.6: The leading order and next-to-leading order Feynman diagrams for the Drell-Yan process. The solid, spiral and wavy lines correspond to quarks anti-quarks, gluons and Z/γ^* , respectively.

also considered.

The LO and NLO Feynman diagrams of the DY process are shown in Fig. 2.6. In general, eq. 2.20 is obtained as a perturbative expansion in powers of strong coupling, at the invariant lepton pair mass scale,

$$\begin{aligned}
 \sigma_{\text{pp}} = \sum_q \int dx_1 dx_2 f_q(x_1, m^2) f_{\bar{q}}(x_2, m^2) \\
 \times \left[\hat{\sigma}_{LO} + \frac{\alpha_s m^2}{2\pi} \hat{\sigma}_{NLO} + \left(\frac{\alpha_s m^2}{2\pi} \right)^2 \hat{\sigma}_{NNLO} + O(\alpha_s^3) \right]_{q\bar{q} \rightarrow l^+ l^-}
 \end{aligned}
 \tag{2.24}$$

The evaluation of higher-order QCD corrections gets complicated, when the momenta of the virtual particles in the loop are not constrained which makes the associated integrals to become divergent, leading to infinite cross sections. There are three types of divergences:

1. *Ultraviolet divergences* when the energy of the emitted parton tends to infinity.
2. *Infrared divergences* due to soft-gluon emissions, when the energy of emitted gluon is small and tends to zero.

3. *Collinear divergences* induced by the parton splittings of initial-state partons, when the energy of the emitted gluon is very close to the parent quark.

The ultraviolet infinities are handled using the dimensional regularization procedure [48]. The technique defines the divergences in terms of a physical parameter, the dimensional renormalization scale μ_r , which gives a well-defined meaning to the perturbative expansion. This is the first step of renormalization and is known as regularization procedure. The reparameterization of the free parameter α_s , is performed such that the regularized divergences are absorbed in the definition of α_s , thus acquiring renormalization dependence. A measurable cross section, however, should be independent of μ_r , defined by the renormalization group equation (RGE),

$$\mu_r \frac{d\sigma}{d(\ln \mu_r)} = 0 \quad (2.25)$$

which can be obtained at some reference scale μ_0 . The reference value $\alpha_s(\mu)$ is determined by computing a cross section to certain order in pQCD and using the above equation to derive RGE for α_s in terms of a β -function. Hence, the physical quantity, the cross section, remains finite after renormalization to any order in the perturbative expansion.

However, the infrared collinear divergences are absorbed in the parton densities, when the partonic cross section is convoluted with the PDFs, redefining them as,

$$f_i(x, \mu_f) = f_i(x) c_i^{divergent}(x, \alpha_s, \mu_f) \quad (2.26)$$

The normalized PDFs are the measurable quantities which depend on the factorization scale μ_f . These calculations are verified by the factorization theorem, by including the divergent part of the cross section in the non-perturbative part.

The cross section for the DY process has been theoretically calculated up to next-to-next-to-leading order (NNLO). The fully differential cross section with

NNLO QCD corrections is obtained using the FEWZ [2] generator. At the NNLO, additional contributions from gluon-gluon fusion and quark anti-quark scatterings are included which complicates the NNLO calculations. The corrections which are considered include 1) real-virtual corrections, 2) double real contributions and 3) two-loop virtual corrections [49].

2.3.3 Electroweak Corrections

The electroweak corrections comprise weak and photonic virtual one-loop corrections as well as real photon radiation to the parton-level process $q\bar{q} \rightarrow Z/\gamma^* \rightarrow l^+l^-$. At energies $\hat{s} \sim m_Z$, electroweak radiative corrections are dominated by large electromagnetic effects from initial-state radiation. With the increase in center-of-mass energy beyond the EW scale $\sim \mathcal{O}(100 \text{ GeV})$, the incoming particles radiate plenty of gauge bosons and the impact of higher order EW radiative corrections becomes considerable, with respect to NLO and NNLO QCD effects. The purely weak part of the EW corrections [50, 51] produces leading corrections of the type $\alpha_W \log^2(\mu^2/m_W^2)$, where μ represents the energy scale. These logarithms arise from real or virtual gauge bosons emitted by the initial and final-state particles and correspond to the soft and collinear emissions. Hence, at high energies $\hat{s} \gg m_Z$, the gauge boson scatterings are quite interesting and the radiative effects are typically large which are taken into account using the EW corrections.

The DY production is one of the important processes in hadronic collisions. Hence, it is vital to understand the effect of higher order QCD and EW radiative corrections involved in the process. In this thesis, the DY differential cross section is measured as a function of dilepton invariant mass and compared with theoretical predictions of the SM at NLO and NNLO which include the EW corrections.

Chapter 3

Experimental Details

3.1 The Large Hadron Collider

The Large Hadron Collider (LHC) [52] built by the European Organization for Nuclear Research (CERN) is the largest particle accelerator and collider in the world. It is installed about 100 m underground in a tunnel of the former Large Electron Positron collider beneath the Swiss-French border. The LHC consists of a 27 km ring in which two high-energy beams are accelerated in opposite direction in two separate beam pipes. The experiments at LHC aim to answer some of the most fundamental questions in nature. With the very high energy provided by the LHC, it is possible to study cross sections of benchmark processes at an energy scale never investigated before.

The LHC is designed to accelerate two proton beams up to an energy of 7 TeV per beam to produce proton-proton collisions at a center-of-mass energy $\sqrt{s} = 14$ TeV with instantaneous luminosity of $10^{34} \text{cm}^{-2} \text{s}^{-1}$. The choice to have a proton-proton collider rather than electron-positron collider is mainly driven by the necessity to reach high energies without significant loss due to synchrotron radiations, that is inversely proportional to the fourth power of mass of the accelerated particles. Additionally, it can also accelerate lead ions up to an energy of 1.38

TeV per nucleon for studying lead-lead and lead-proton collisions at 2.76 TeV with instantaneous luminosity of $10^{-27} \text{cm}^{-2} \text{s}^{-1}$.

On 23 November 2009, LHC produced first collisions of protons in stable beams at an injection energy of 450 GeV. After few runs at beam energy of 1.18 TeV, the energy was ramped up to 3.5 TeV. The first proton-proton collisions at a centre-of-mass energy $\sqrt{s} = 7$ TeV took place on 30 March 2010, which marked the highest energy reached at a particle collider. In 2012, the centre-of-mass energy was increased to 8 TeV and in 2015 the energy was further increased to 13 TeV after a long shutdown of two years. Since then, the LHC is running successfully and collecting data from proton-proton collisions at $\sqrt{s} = 13$ TeV. Recently in 2017, LHC accelerated and collided xenon nuclei at the beam energy of 2.72 TeV per nucleon to record a short run of xenon-xenon collisions at a centre-of-mass energy of 5.44 TeV, in order to study the phenomena observed in Quark-Gluon Plasma.

3.1.1 LHC Design

The collider tunnel contains two adjacent parallel beam lines each containing a beam, travelling in the opposite direction. The particle collisions take place at four intersecting points around the ring. However, before reaching the collision point, the energy of particles is increased by a series of accelerators that successively increase their energy. The LHC protons originate from a tank in which electrons are stripped from the hydrogen atoms and injected into LINAC2, the Linear Particle Accelerator. LINAC2 accelerates the protons to 50 MeV which are fed to the Proton Synchrotron Booster (PSB), further accelerating them to 1.4 GeV. In the next step, protons are injected into Proton Synchrotron (PS) and Super Proton Synchrotron (SPS) which accelerate the protons to 26 GeV and 450 GeV, respectively.

The proton beams originating from the SPS are finally introduced into the main ring, where they are accumulated and accelerated to their peak energy before the collisions take place. The schematic view of the LHC accelerator chain is

shown in Fig. 3.1. The beams are guided by a strong magnetic field maintained by superconducting electromagnets throughout the accelerator ring. These includes a series of 1232 dipole magnets with magnetic fields up to 8.3 Tesla. The operating temperature of 1.9 K is maintained using 96 tonnes of superfluid helium, making LHC the largest cryogenic system in the world. In addition to the dipoles, there are about 392 quadrupole magnets which focus the proton beams while higher multi-pole orders are used to correct smaller imperfections in the field geometry. At full intensity, each beam consists of 2808 ellipsoidal bunches with $\sim 1.15 \times 10^{11}$ protons per bunch. During the nominal operation of the LHC, the proton bunches are 25 ns apart which provides a collision rate of 40 MHz with a given bunch crossing.

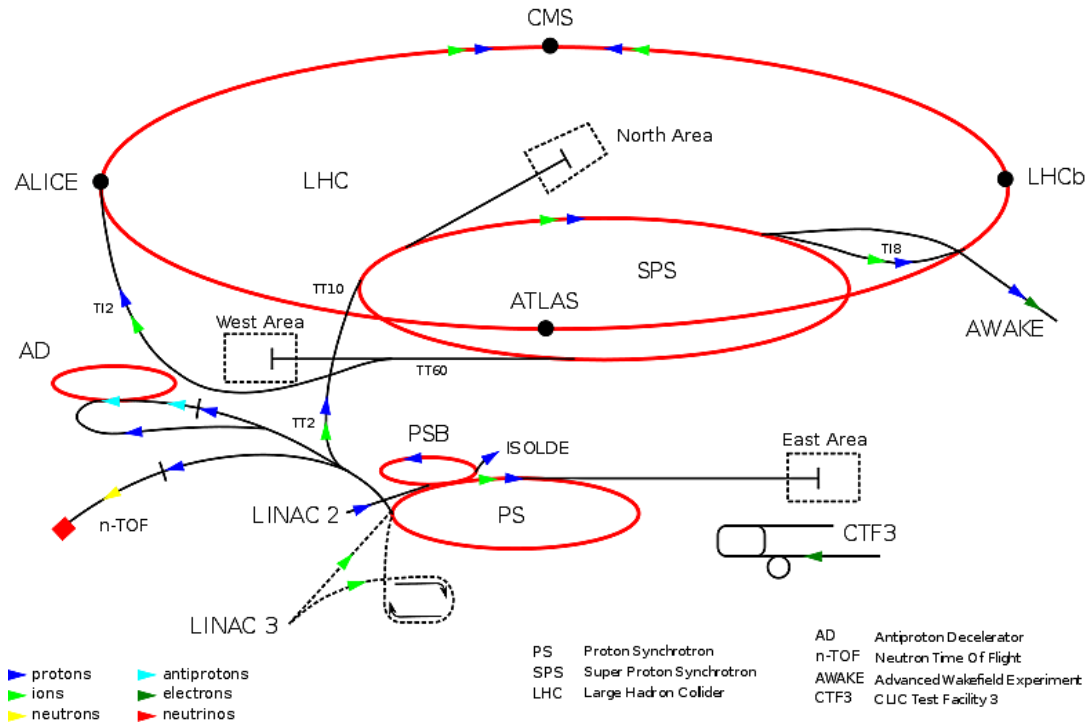


Figure 3.1: Accelerator Complex at CERN. The protons originating from the hydrogen tank are injected into a series of accelerators which accelerate the protons step by step before getting introduced into the main ring¹⁰.

The layout of the LHC is composed of eight arcs and eight straight sections.

¹⁰Source : https://en.wikipedia.org/wiki/Large_Hadron_Collider

Each section is equipped with an experimental apparatus. The two high luminosity experimental insertions at the LHC are located at diametrically opposite straight sections: A Toroidal LHC Apparatus (ATLAS) [53] and the Compact Muon Solenoid (CMS) [54] experiments located at Point 1 and Point 5, respectively. These two general purpose experiments with complementary detector technologies share the interaction point with Total Cross Section, Elastic Scattering and Diffraction Dissociation (TOTEM) [55] and Large Hadron Collider forward (LHCf) [56], which perform dedicated studies for cross section measurements and forward physics. The other two experiments A Large Ion Collider Experiment (ALICE) [57] and Large Hadron Collider beauty (LHCb) [58] are located at Point 2 and 8, respectively. The heavy ion experiment ALICE is dedicated to the study of quark-gluon plasma, the fluid form of matter while the LHCb collaboration performs specialized b-physics experiments to measure the parameters of CP violation in order to confirm possible physics BSM.

3.1.2 Luminosity and Machine Parameters

The luminosity [59] in collider physics quantifies the performance and intensity of the collisions. It defines the possibility for the production of a certain number of events of a process in a given time interval. The number of events per second (N_{event}) generated in a collision is defined by:

$$N_{event} = \mathcal{L} \cdot \sigma_{event} \quad (3.1)$$

where, σ_{event} is the cross section for the event type under study and \mathcal{L} is the instantaneous luminosity which depends upon the beam parameters and for a Gaussian beam distribution can be written as:

$$\mathcal{L} = \frac{N^2 n_b f_{rev} \gamma_r}{4\pi \epsilon_n \beta^*} F \quad (3.2)$$

where, f_{rev} is the revolution frequency of the bunches, N is the number of protons per bunch, n_b is the number of colliding bunches, γ_r is the Lorentz factor, ϵ_n is the normalized transverse beam emittance, β^* is the beta function at the collision point and F is the geometric reduction factor arising from crossing angle. The luminosity is therefore, totally dependent on the collider parameters and characterizes the performance of the machine. The continuous increase of the luminosity delivered by the LHC and recorded by the CMS at a center-of-mass energy $\sqrt{s} = 13$ TeV in the year 2015 is shown in Fig. 3.2.

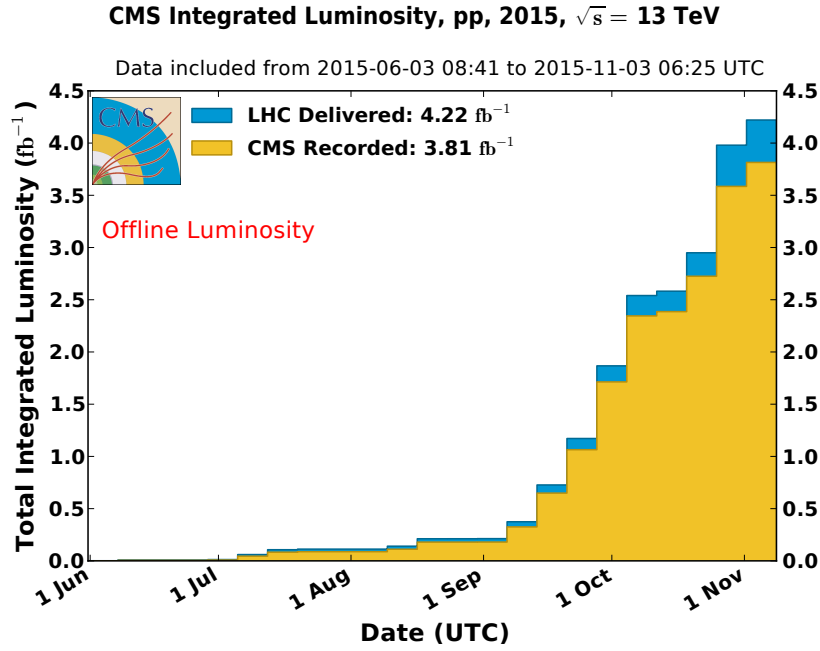


Figure 3.2: Total integrated luminosity delivered by LHC and recorded by CMS at a center-of-mass energy $\sqrt{s} = 13$ TeV, during the year 2015¹¹.

3.1.3 The Compact Muon Solenoid

The CMS is a general purpose particle detector designed for the physics environment provided by the LHC. It is situated about 100 m underground near the French village

¹¹Source : <https://twiki.cern.ch/twiki/bin/view/CMSPublic/LumiPublicResults>

of Cessy. The generic detector has a composite structure consisting of several sub-detectors inserted into each other, starting from the interaction point. It consists of two main parts: a cylindrical part known as the barrel and two circular parts known as the endcaps which are located on both sides of the barrel along the beam axis to ensure a maximum detection coverage. In order to achieve the goals of the LHC physics program, the CMS experiment should meet the following detector requirements:

- A highly efficient and high momentum resolution inner tracker to reconstruct and measure the charged-particle momentum.
- Good electromagnetic calorimeter with high energy resolution, diphoton and dielectron mass resolution $\approx 1\%$ at 100 GeV, a wide geometric coverage, photon detection from π_0 decay and highly efficient photon and lepton isolation at high luminosities.
- Good dijet mass and missing transverse energy resolution, requiring hadronic calorimeter with a large hermetic geometric coverage and fine lateral segmentation.
- Good identification and momentum resolution muon system, dimuon mass resolution $\approx 1\%$ at 100 GeV and efficient charge determination of muon with momentum up to 1 TeV.

The design of the CMS detector meets all the above mentioned requirements. As illustrated in the Fig. 3.3, there is a large bore superconducting solenoid with a 3.8 T magnetic field at the core of the detector surrounding silicon pixel and strip inner tracker, a lead-tungstate scintillating crystal homogeneous electromagnetic calorimeter, a brass scintillator sampling hadron calorimeter and a muon system with three types of detectors ensuring full geometric coverage. The iron yoke which serves as the return path of magnetic flux is interleaved with four muon stations. The overall dimensions of the CMS detector are a length of 21.6 m and a diameter

of 14.6 m with a total weight of about 1.25×10^7 kg.

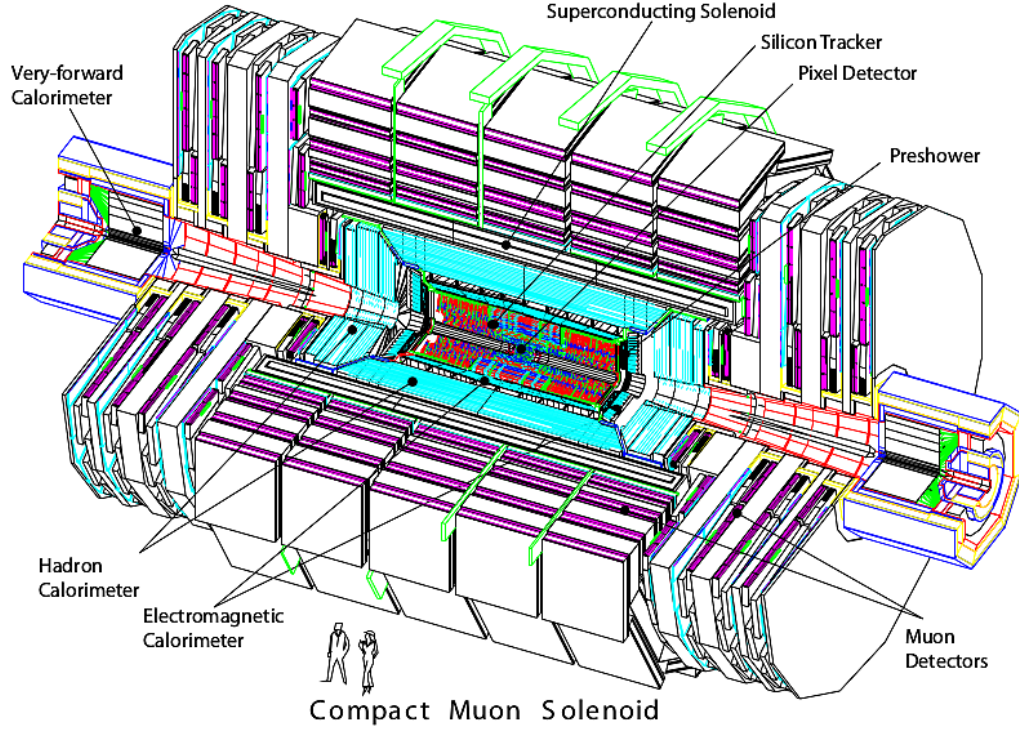


Figure 3.3: A schematic diagram of the Compact Muon Solenoid. The detector consists of the inner tracker system, the calorimetry system, the muon identification system and a large superconducting magnet. Taken from [60].

3.1.4 Coordinate Conventions

The adopted coordinate system for the CMS detector has the origin located at the nominal collision point which is the geometrical center of the detector. The x-axis points radially inward towards the center of the LHC ring, the y-axis points vertically upward perpendicular to the LHC plane and the z-axis points west along the counterclockwise traveling beam direction (seen from above) as shown in Fig. 3.4. The direction of the z-axis lies in the longitudinal plane. The x-y plane, orthogonal to the beam line is called transverse plane.

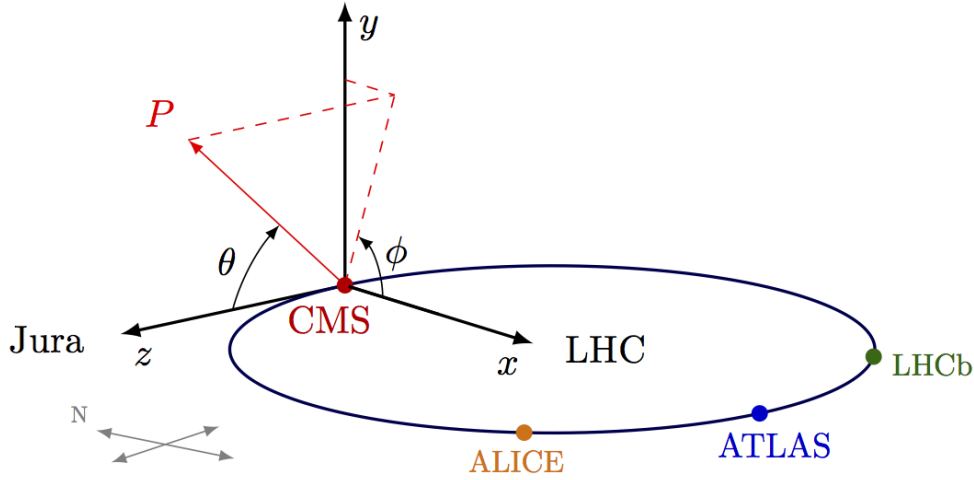


Figure 3.4: The CMS coordinate system is defined with respect to the LHC ring. The x-axis points inward towards the center of the ring, the y-axis points vertically upward and the z-axis points in the direction of the beam. The azimuthal angle ϕ is measured from the x-axis in the x-y plane where the radial coordinate is denoted by r . The polar angle θ is defined with respect to the z-axis in the r-z plane¹².

Information about momentum and energy is often given by its transverse components p_T and E_T which are linked to the cartesian coordinates in the following way,

$$p_T = \sqrt{(p_x^2 + p_y^2)} \quad (3.3)$$

$$E_T = E \frac{p_T}{\sqrt{(p_T^2 + p_z^2)}} \quad (3.4)$$

A widely used coordinate variable is the rapidity (y) or pseudorapidity (η). y has the property of being invariant under longitudinal boosts in the direction of z-axis and is defined as,

$$y = \frac{1}{2} \ln \frac{E + p_z}{E - p_z} \quad (3.5)$$

In relativistic limit i.e. for high energy or massless particles, y can be approx-

¹²Source : https://wiki.physik.uzh.ch/cms/latex:example_spherical_coordinates

imated by η as,

$$\eta = -\ln\left(\tan\frac{\theta}{2}\right) \quad (3.6)$$

where, the θ coordinate measures the angle with respect to the positive z -axis. $\eta = 0$ for the particles perpendicular to the z -axis and $\eta = \infty$ corresponds to the beam axis in $\pm z$ -direction. The azimuthal angle ϕ is measured with respect to the x -axis in the transverse plane and has the range $(-\pi, \pi)$. The angular distance between two particles is defined in the form of a Lorentz invariant ΔR variable,

$$\Delta R = \sqrt{\Delta\eta^2 + \Delta\phi^2} \quad (3.7)$$

3.1.5 Superconducting Magnet

The CMS detector requires a very strong magnetic field to be able to induce enough bending of the charged particles so that the momentum measurement can be performed up to the highest momentum particle expected at the LHC energy. The superconducting solenoid magnet [61] for the CMS is designed to reach a 4 T field in a cylindrical region of 12.5 m length and 6 m diameter. The magnetic flux is returned through a 10^7 kg yoke consisting of five barrel wheels and two endcaps on each side, composed of three layers. The superconducting high-purity aluminium-stabilized niobium-titanium (NbTi) coil is cooled down to a temperature below 4^0 K using a complex liquid helium cooling system. The bore of the magnet accommodates both the inner tracker and the calorimetry inside which limits the energy loss interactions, thus improving the energy resolution of the calorimeter.

3.1.6 Inner Tracking System

The inner tracking system [62, 63] has been built to operate in a harsh environment at the LHC, featuring high granularity and fast response. It provides a precise

and efficient measurement of the trajectories of charged particles emerging from the proton-proton collisions, as well as a precise reconstruction of primary and secondary vertices. The tracking system surrounds the interaction point and has a length of 5.8 m with a diameter of 2.5 m. The CMS tracking design is based entirely on the silicon detectors with about 200 m² active silicon area. Figure 3.5 shows a schematic of the CMS tracking system consisting of a pixel detector and silicon strip tracker, covering a pseudorapidity range of $|\eta| < 2.5$.

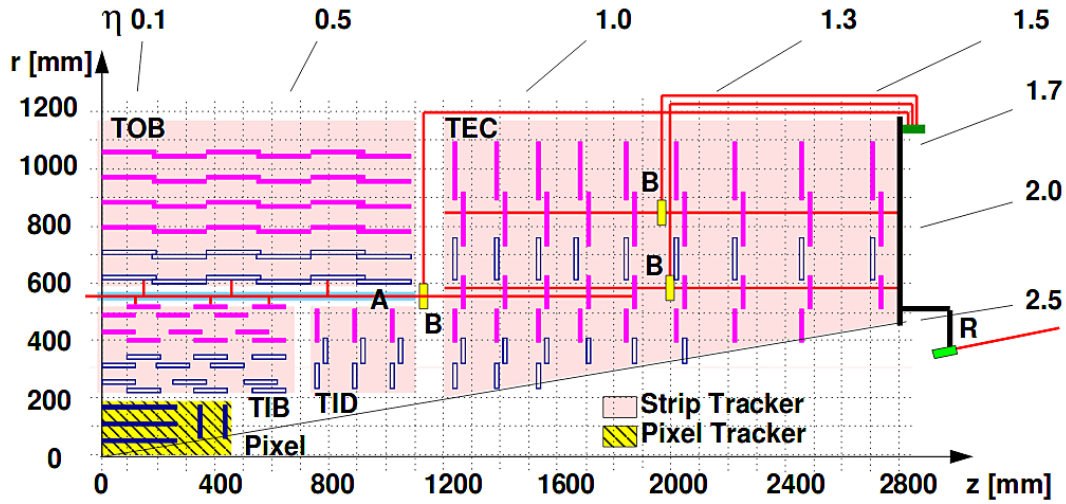


Figure 3.5: The CMS tracking system consists of Pixel detector and Silicon strip tracker comprising of Tracker Inner/Outer Barrel, Tracker Inner Disc and Tracker Endcap sub-detectors¹³.

Pixel Detector : The pixel detector contributes to a precise two-dimensional measurement of the particle position in r - ϕ and z and hence responsible for a small impact parameter (longitudinal and transverse distances from the primary vertex) resolution. It consists of 53 cm long, three cylindrical layers of hybrid pixel detector modules placed at radii of 4.4 cm, 7.3 cm and 10.2 cm from the interaction point in the barrel region, referred to as pixel barrels (BPix), complemented by two endcap

¹³Source : <https://arxiv.org/abs/0910.2505>

disks, referred to as forward pixels (FPix) on each side of the detector. A total of 768 pixel modules in BPix and 672 modules in FPix constitute the pixel detector. A single pixel in barrel module is readout using 16 read-out chips (ROC) while in endcap, the ROCs vary from 2 to 10. Each chip reads an array of 52×80 pixels. The modules are tilted by approximately 20° , resulting in a turbine-like geometry. Each module is made of 66 million square pixels, with a dimension $100 \times 150 \mu\text{m}^2$ of each pixel and an active area of around 1 m^2 , thus providing this sub-system a high granularity.

Silicon Strip Tracker : The silicon strip system is divided into four parts. The central region is covered by the Tracker Inner Barrel (TIB) and the Tracker Outer Barrel (TOB). The TIB is composed of four cylindrical layers of modules covering the region $25 \text{ cm} < r < 50 \text{ cm}$, while the TOB covers the region $50 \text{ cm} < r < 116 \text{ cm}$ and extends in z between $\pm 118 \text{ cm}$, with six cylindrical regions. The forward region is covered by the Tracker Inner Disks (TID), three disks on each side of TIB. The TIB/TID delivers up to 4 r - ϕ measurements for trajectory reconstruction. The TOB provides another set of 6 r - ϕ measurements. Beyond this, the Tracker Endcap (TEC) covers the rest of the region and is composed of 9 circular wheels covering the region $130 \text{ cm} < |z| < 270 \text{ cm}$ on each side along the z -axis (TEC+ and TEC-) and provides up to 9 ϕ measurements for trajectory reconstruction.

Particles crossing the tracker can interact with the material, especially electrons which radiate photons through Bremsstrahlung process and thus lose significant part of their energy within the tracker. Hence, it is important to have an estimate of the amount of tracker material. The thickness of the CMS tracker is expressed in units of radiation length x/X_0 as a function of η as shown in Fig. 3.6. The tracking system provides a good transverse momentum resolution of about 1-2% for high momentum (100 GeV) tracks up to $|\eta| \approx 1.6$ and becomes worse in the high η region. It increases from approximately 0.4 x/X_0 at $|\eta| = 0$ to about 1.8 x/X_0 at

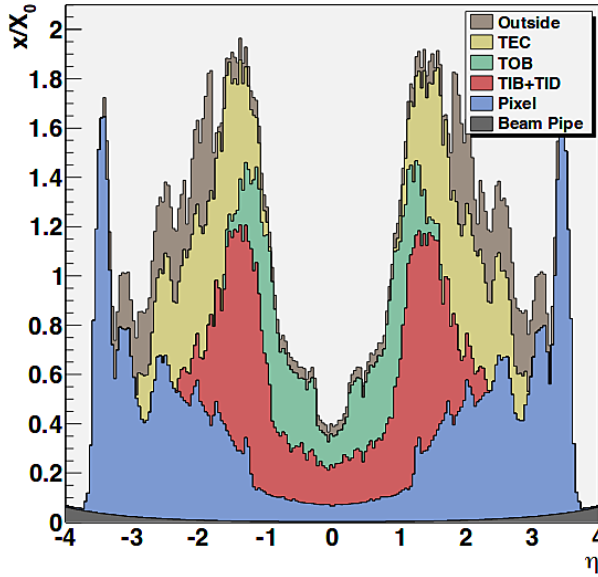


Figure 3.6: Tracker material thickness as a function of pseudorapidity η , expressed in relative radiation length x/X_0 of the different components of the tracker¹⁴.

$|\eta| = 1.4$, beyond which it falls to about $1.2 x/X_0$ at $|\eta| = 2.5$.

3.1.7 Electromagnetic Calorimeter

The principle of the CMS electromagnetic calorimeter (ECAL) [64,65] relies on the development of electromagnetic shower initiated by an electron or a photon interaction with a scintillating crystal via Bremsstrahlung process or pair production. Two quantities are used to quantify the development of an electromagnetic shower: the radiation length X_0 , which quantifies the longitudinal development, is the distance after which the electron has lost a fraction of its energy equal to $1/e$ and the Moliere radius r , which quantifies the lateral development.

The work presented in this thesis is based on the reconstruction of electrons which starts with the measurement of energy deposited by the electromagnetic showers in the ECAL and will be discussed in details in the next chapter.

The layout of ECAL is shown in Fig. 3.7 and the longitudinal view of ECAL

¹⁴Source : <http://stacks.iop.org/1748-0221/4/i=05/a=P05003>

is shown in Fig. 3.8. The choice of the design of ECAL lead to a compact and homogeneous lead tungstate ($PbWO_4$) [66,67] scintillating crystal calorimeter. The material used for the ECAL has a very high density 8.28 g/cm^3 , a small Moliere radius 21 mm and a short radiation length 0.89 cm, allowing for a compact design of the detector. It has a fast readout response with 80% of the light getting emitted in one bunch crossing i.e. 25 ns. The ECAL consists of 61200 crystals in the central region ($|\eta| < 1.479$) and 7324 crystals in each of the two endcaps ($1.479 < |\eta| < 3$).

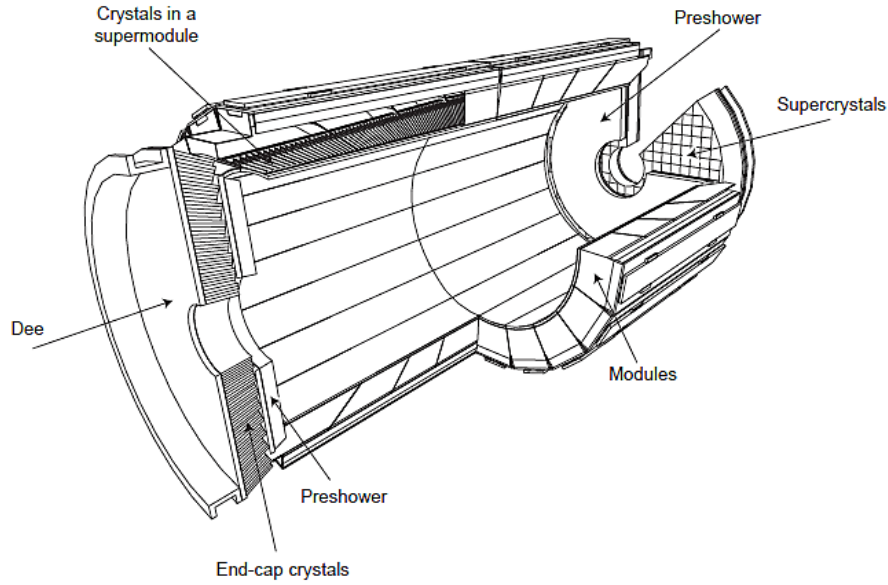


Figure 3.7: Layout of the CMS Electromagnetic Calorimeter which shows arrangement of the crystal modules, supermodules and endcaps along with the preshower detector¹⁵.

Barrel Electromagnetic Calorimeter

The barrel section of the ECAL (EB) has an inner radius of 129 cm. The crystals are mounted on thin-walled structures called submodules with a thickness of 0.1 mm, arranged further into modules and supermodules. The barrel crystal has trapezoidal shape with front dimensions of $22 \times 22 \text{ mm}^2$ and a radial length of 230 mm which corresponds to $25.8 X_0$. Scintillation light provided by the crystals is directed to the

¹⁵Source : <http://arxiv.org/abs/arXiv:1308.6064>

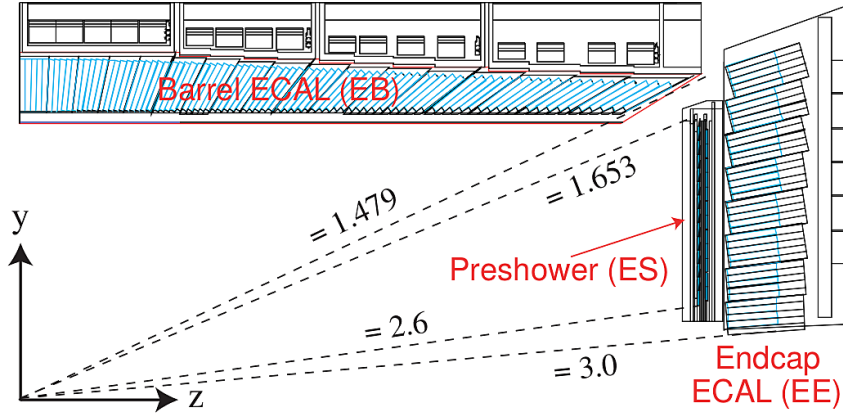


Figure 3.8: Longitudinal view of CMS Electromagnetic Calorimeter which shows the barrel ($|\eta| < 1.479$) and endcap ($1.479 < |\eta| < 3$) regions. Taken from [60].

avalanche photodiodes (APD) [68] which convert light into analog signals, amplify it and send it to outer electronics for further processing and trigger decision.

Endcap Electromagnetic Calorimeter

The endcaps in the ECAL (EE) are placed at a distance of 314 cm from the vertex. The endcap consists of identically shaped crystals arranged in bigger units of 5×5 crystals called supercrystals. Each EE is formed from two structures having a D shape called Dees and can hold 3662 crystals each. The crystal front dimensions are $28.6 \times 28.6 \text{ mm}^2$ with a radial length of 220 mm which corresponds to $24.7 X_0$. Due to the higher expected hadron fluency in the forward region, more radiation resistant device, the vacuum phototriode (VPT) [68] is used for light to analog signal conversion and preamplification.

In addition, a silicon/lead preshower detector (ES) is installed in front of the endcap calorimeter ($1.65 < |\eta| < 2.6$), in order to improve the γ/π_0 discrimination and vertex reconstruction of photons. The energy resolution of the ECAL can be parameterized as [69],

$$\left(\frac{\sigma}{E}\right)^2 = \left(\frac{S}{\sqrt{E}}\right)^2 + \left(\frac{N}{E}\right)^2 + C^2 \quad (3.8)$$

where, S is the stochastic term which represents the statistical error from electromagnetic shower evolution, N the noise term is the error in energy measurement due to noise from the electronics and pileup and C the constant term is related to the calorimeter calibration. The ECAL energy resolution in test beams using electrons of 20 to 250 GeV has been measured to be:

$$\left(\frac{\sigma}{E}\right)^2 = \left(\frac{2.8\%}{\sqrt{E}}\right)^2 + \left(\frac{12\%}{E}\right)^2 + (0.3\%)^2 \quad (3.9)$$

The contributions from different terms change at different pseudorapidities and with the luminosity of the machine. The constant term C is dominant at high energies and includes different contributions, like, the stability of the operating conditions (voltage and temperature), transparency loss of crystals and the inter-calibration errors.

3.1.8 Hadron Calorimeter

The hadron calorimeter (HCAL) [70] in the CMS is a sampling calorimeter which uses different materials for active and passive regions. It is formed of layers of plastic scintillating tiles with embedded optical fibers interleaved with brass layers. The brass is chosen as an absorber material for its high density 8.73 g/cm^3 . The hadronic calorimeter plays an important role in the identification of quarks and gluons by measuring the energy and direction of hadronic jets. Additionally, it provides an indirect measurement of uncharged, non-interacting neutrinos and other exotic particles which leave a signature in the form of missing transverse energy (MET), by using the conservation of momentum in the transverse plane. The HCAL is radially restricted between the outer extent of the ECAL and the inner extent of the solenoid which puts a limitation on the amount of absorber material used in the calorimeter. Hence, the HCAL design maximizes the material inside the magnet coil in terms of interaction lengths.

A schematic view of HCAL is shown in Fig. 3.9. The HCAL design is characterized by a cylindrical part called the barrel (HB) and two circular structures called the endcaps (HE), located on each side of the barrel. In addition, the hadron outer (HO), placed outside the coil, complements the barrel calorimeter in the central region, ensuring no energy leaks out undetected from the barrel part and the hadron forward (HF) extends the calorimeter acceptance in the forward region of the detector up to $|\eta| = 5.2$.

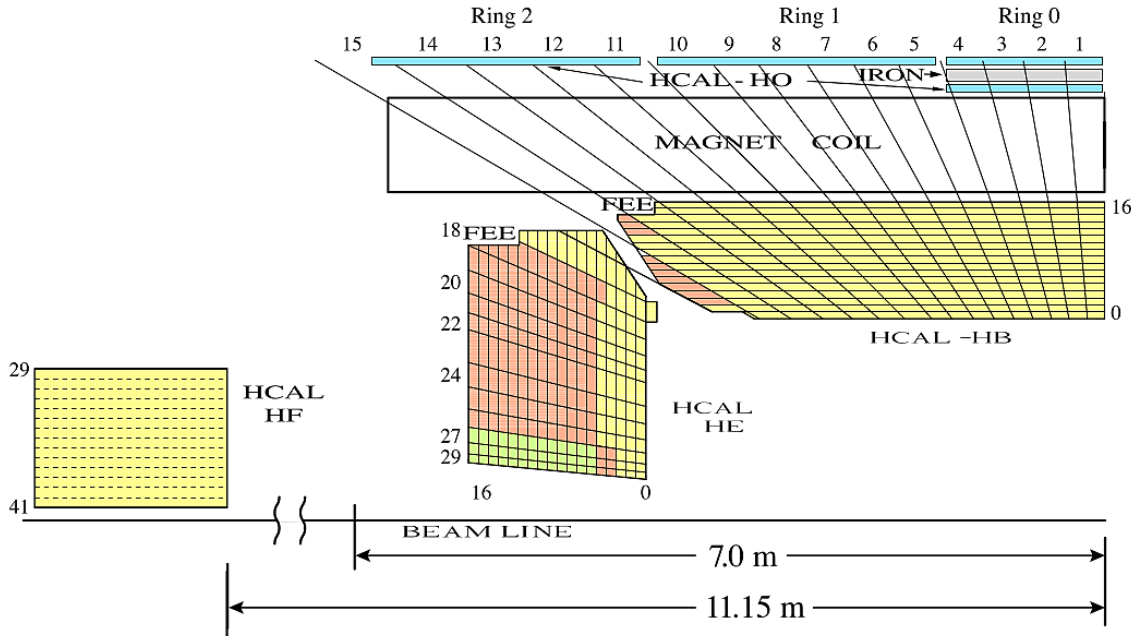


Figure 3.9: A quarter slice of the CMS Hadronic Calorimeter. The calorimeter is divided into three sub-detectors in barrel, endcap and forward regions and one sub-detector in the outer region, that lies outside the solenoid¹⁶.

Hadron Barrel

The hadron barrel consists of 32 towers and covers the pseudorapidity region $|\eta| = 1.3$, with $\Delta\eta \times \Delta\phi = 0.087 \times 0.087$ segmentation. It is made of two halves on the positive and negative side of the z -axis, each half divided into 18 identical wedges covering a ϕ region of 20° . A total of 17 plastic scintillators as active material in-

¹⁶Source : <https://cds.cern.ch/record/1481837>

terleaved with stainless steel and brass absorber plates, each with a thickness of 5 cm, constitute the HCAL barrel. The effective thickness of barrel increases with polar angle as $1/\sin\theta$, resulting in the total absorber thickness of 5.82 interaction lengths (λ_I) at $\theta = 90^\circ$, $\eta = 0$ and $10.6 \lambda_I$ at $|\eta| = 1.3$. All layers in one $\eta \times \phi$ cell are connected by wavelength shifting (WLS) fibers and read out as single channel, resulting in 2304 truncated pyramid shaped HCAL towers.

Hadron Endcap

Two circular structures complement the barrel in the forward pseudorapidity region $1.3 < |\eta| < 3.0$, also made of brass and plastic scintillator. The granularity of the crystals is $\Delta\eta \times \Delta\phi = 0.087 \times 0.087$ for $|\eta| \in (1.3, 1.6)$ and is doubled for the region $|\eta| \in (1.6, 3)$ with $\Delta\eta \times \Delta\phi = 0.17 \times 0.17$. The brass plates have a thickness of 79 mm with 9 mm gaps to house the plastic scintillators. The total length of the endcap calorimeter is about $10 \lambda_I$. The light is collected by WLS fibers and routed to the photo-sensors, hybrid photodiodes (HPDs).

Hadron Outer

To ensure adequate shower containment in the region $|\eta| < 1.3$, the HCAL is extended outside the magnet coil with an array of scintillators in the outer barrel calorimeter known as the Hadron Outer. The tail catcher is used to identify late starting showers and measure energies of the particles emerging at the ends of the solenoid. The inclusion of the HO detector extends the sampling depth of the calorimeter to a minimum of $11 \lambda_I$. The scintillation light is detected by the HPDs which are capable of operating in high axial magnetic fields. The light is converted by WLS fibers which are embedded in the scintillator tiles and transmitted to front-end photodetectors over clear fibers. However, the HPDs were later replaced by the Silicon Photo Multipliers (SiPMs) as the photo-sensors due to performance and operational reasons and will be discussed later in this thesis.

The HO is divided into 5 sections along η , called rings. The central ring (ring

0) contains two layers of HO scintillators at a radial distance of 3.82 m and 4.07 m, on either side of a 19.5 cm thick piece of iron. The other four rings (rings ± 1 and ± 2) contain a single layer of HO scintillator at 4.07 m of radial distance. One of the major contributors in the fabrication of scintillation counters for HO are the Panjab University group (Chandigarh), along with Tata Institute of Fundamental Research group (Mumbai).

Hadron Forward

The region between $3.0 < |\eta| < 5.0$ is covered with the Hadron Forward calorimeter on each side of the z-axis. The two HF calorimeters (HF+ and HF-) are composed of quartz fibers encased in cylindrical steel matrices with an outer radii of 130 cm. As the shower of charged particles propagate through the quartz fibres, they emit Cherenkov light which is converted into current by the photomultiplier tubes (PMTs). There are 13 towers along η , with a size $\Delta\eta \approx 0.175$, except for the lowest and the highest η towers with $\Delta\eta \approx 0.1$ and $\Delta\eta \approx 0.3$, respectively. The ϕ segmentation of all the towers is 10° , except $\Delta\phi = 20^\circ$ for the highest η tower. This leads to a total of 900 towers and 1800 channels in both HF modules. The HF calorimeter improves the measurement of the MET and enables very forward jets to be identified and reconstructed.

The energy resolutions for different parts of the HCAL are given by [71]:

$$\left(\frac{\sigma_E}{E}\right)^2 = \left(\frac{84.7\%\sqrt{\text{GeV}}}{\sqrt{E}}\right)^2 + (7.4\%)^2 \quad \text{for HB, HE and HO}, \quad (3.10)$$

$$\left(\frac{\sigma_E}{E}\right)^2 = \left(\frac{198\%\sqrt{\text{GeV}}}{\sqrt{E}}\right)^2 + (9.0\%)^2 \quad \text{for HF} \quad (3.11)$$

3.1.9 Muon System

The detection of muons is a powerful tool for understanding the signatures of interesting processes over the high background rate present at the LHC. The muons get less affected by radiative losses due to the tracker material budget, hence emphasizing the discovery potential of muonic final states and the essential detection of muons with large angular coverage.

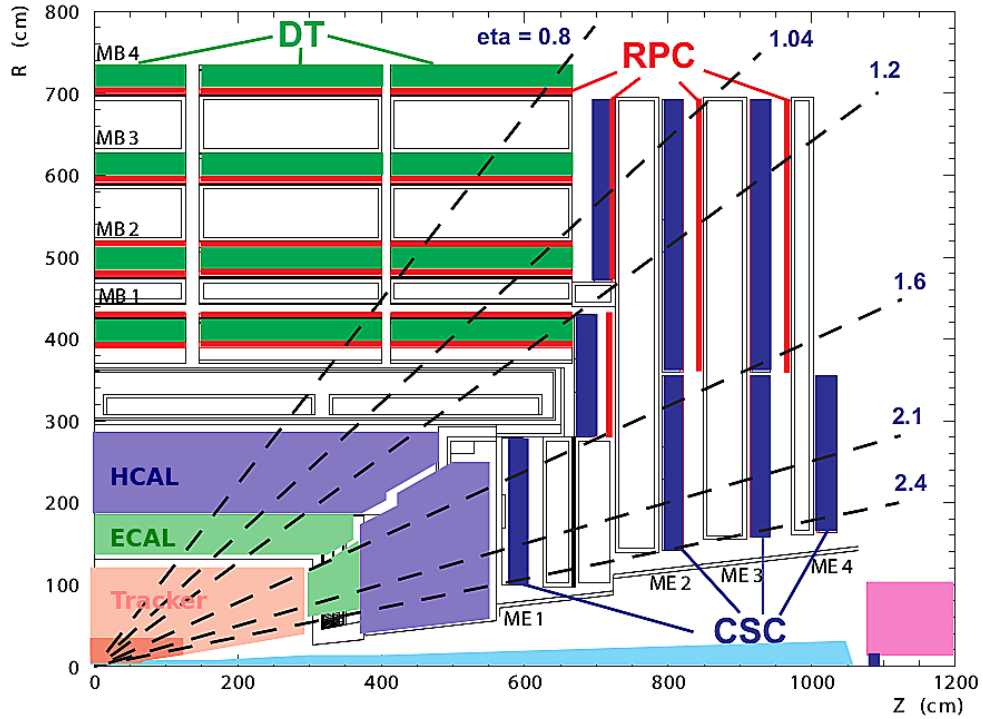


Figure 3.10: The CMS Muon system consists of Drift Tube, Cathode Strip and Resistive Plate chambers which are placed outside the solenoid magnet and embedded in the iron return yoke. Taken from [60].

The muon spectrometer [72] is placed outside the magnet coil in the region $|\eta| < 2.4$ and is interleaved with the iron return yoke. The CMS muon system has been constructed to efficiently identify, trigger and measure muon charge and momenta over the entire kinematic range. Good momentum resolution and trigger capability are enhanced by the high field solenoidal coil and its flux return yoke. A

sketch of the muon system is shown in Fig. 3.10. Three different gaseous particle detectors are used for the identification and measurement of muons. In the barrel region $|\eta| < 1.2$, the muon rate and the residual magnetic field is low, hence drift tube (DT) chambers are used. However, in the two endcaps, where the muon rate is high and the magnetic field is high and non-uniform, cathode strip chambers (CSC) are used in the region up to $|\eta| < 2.4$. Additionally, resistive plate chambers (RPC) are used in both the barrel and endcap regions $|\eta| < 1.6$, providing a fast response with good time resolution but a coarser position resolution than DTs or CSCs.

Drift Tube Chambers

In the muon barrel (MB) region, four stations of muon detectors are arranged in cylinders embedded in the iron yoke. Each chamber with an average size of 2×2.5 m, is made up of twelve aluminium layers which are grouped in three independent subunits called the superlayers (SL), forming the smallest independent unit of the design called the cell. A drift cell is made up of two electrode plates filled with a non-flammable gas mixture of Ar-CO₂ with 85% Ar and 15% CO₂ at atmospheric pressure. The anode wires in the two outer SLs are parallel to the beam line, providing track measurement in the $r - \phi$ plane. In the inner SL, the wires are however, orthogonal to the beam line and provide a measurement of the longitudinal coordinate z . This third z -measuring inner SL is not present in the fourth DT station, which therefore measures the ϕ coordinate only.

Cathode Strip Chambers

The muon endcap (ME) system consists of 234 CSCs on each side of the detector. The CSCs have multiwire proportional chambers made of negatively charged cathode plane segmented into strips and running orthogonal to the positively charged anode wires. With a short drift path, the CSC chambers have a fast response time, reducing the sensitivity to the non-uniform magnetic field which provides a precision muon measurement and make them suitable for triggering. CSC chambers consist

of four endcap stations placed between the iron discs of the yoke. Each chamber is built by six trapezoidal shaped layers, with strips along the radial direction at a constant $\Delta\phi$ width, which provides a precise measurement of the azimuthal coordinate as well as accurate matching of the tracks with those in the tracker. The spatial resolution provided by each chamber is approximately $200\ \mu\text{m}$ in r and z and approximately $10\ \text{mrad}$ in ϕ . The muons in the pseudorapidity range $|\eta| \in (1.2, 2.4)$ cross at least three CSC layers. In the barrel-endcap overlap range of $|\eta| \in (0.9, 1.2)$, muons are detected by both the DTs and CSCs.

Resistive Plate Chambers

The RPCs installed in the barrel and the endcap regions, can be operated at high particle rates up to $10\ \text{kHz}/\text{cm}^2$ with a good time resolution and response much faster than $25\ \text{ns}$. Hence, they enable unambiguous assignment of signals to the correct bunch crossing despite of high background present at the LHC. The signals from these devices also provide the trigger information by measuring the position of a muon hit with the required accuracy. They cover the acceptance region $|\eta| < 1.6$ and are double-gap chambers filled with a $\text{C}_2\text{H}_2\text{F}_4$ and C_4H_{10} gas mixture, operating in avalanche mode. Their excellent time resolution is countered by their coarse position resolution, poorer than the other muon detectors. The RPCs are grouped in stations like the DTs and CSCs, with four stations in the barrel region and three in the endcap. The innermost barrel stations have two RPC layers along the outside of the DT chambers, with each layer divided into two or three partitions in η . The RPC endcap stations are divided into three rings with increasing radial distance from the beam line, with 36 chambers in each ring covering the full azimuthal range.

3.1.10 Trigger System

The LHC bunch crossing rate of $40\ \text{MHz}$ and the CMS event size of approximately $1\ \text{MB}$ lead to a massive amount of delivered data which is too large to be stored

and analyzed. In order to process this data, there is a need of reduction in the rate to make its size equivalent to the offline storage limit, $\mathcal{O}(100\text{Hz})$. Hence, one of the most important and difficult aspects of this experiment is the designing and achieving a Trigger and Data Acquisition (DAQ) system [73] to transfer the data to storage for further processing.

The CMS trigger system performs a fast online selection of potentially interesting events, lowering the rate of recorded events eventually to approximately 300 Hz. This reduction by a factor of more than 10^5 does not limit the discovery potential of CMS since the cross sections of processes, such as the cross section measurements of W/Z boson, top quark or other diboson processes, Higgs physics or other exotic BSM studies, are even smaller compared to the total proton-proton cross section. The design of CMS trigger and data acquisition system is illustrated in Fig. 3.11. The selection of events is based on their physics content, such that the online algorithms are developed sophisticatedly, making them comparable to that of the offline reconstruction keeping the efficiency for physics objects high. The CMS trigger has two levels: The Level 1 Trigger and the High Level Trigger.

Level 1 Trigger

The Level 1 (L1) trigger system consists of custom designed, highly programmable hardware electronics. It uses coarsely segmented data from calorimeters and muon system as well as a correlation of information to perform the first level of online event selection. The algorithms process and hold the high-resolution data in pipelined memories with negligible deadline and a design output rate limit of 100 kHz. The allowed latency between a bunch crossing and the transmission of the trigger decision to the detector electronics is $3.2 \mu\text{s}$. The trigger decision at the L1 level is based on the presence of physics objects such as photons, electrons, muons and jets with p_T above a certain threshold as well as characteristics such as the amount of experimental MET.

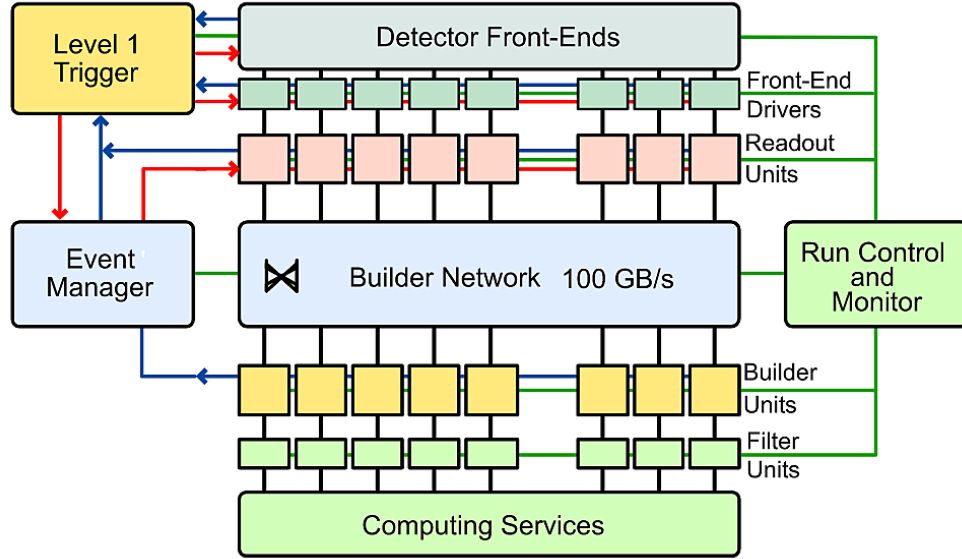


Figure 3.11: The CMS Trigger and Data Acquisition System consist of Level 1 and High Level Trigger. Taken from [54].

High Level Trigger

The High Level Trigger (HLT) is a software based system employing event filter units of about 1000 commercial processors with a latency of approximately 30 ms. The information which is not available in the time scale of L1 trigger decision is used by the HLT and includes the complete information from the tracker and the calorimeters. The HLT, therefore uses the full event data to make a decision. It works on the principle of regional reconstruction in order to avoid the complete event reconstruction and fast event rejection by discarding the uninteresting events as fast as possible. If an event is accepted by the L1 trigger known as L1 accept (L1A), the data is transferred further to HLT which applies a predefined set of requirements, reducing the rate of events to 100 Hz. Upon being accepted, the data from the event is transferred for storage and further processing by the physicists. Since the HLT is software-based, reconstruction algorithms and selection requirements can be quickly adjusted during operation. The HLT algorithms depend strongly on the expected instantaneous luminosity and need a prescale factor in order to reduce the output

rate for high luminosity runs.

3.1.10.1 Electron Triggers

Various triggers are designed depending on the analysis to be performed. At the L1 level, the local trigger uses information from the energy deposited in the ECAL and the HCAL calorimeters, called the calorimeter trigger. This information is transferred to the regional trigger which combines the information from each sub-detector's local trigger and passes the information further to global trigger. At this level, a decision is taken to accept or reject the event based on a set of defined algorithms for a physics object. These algorithms, known as Trigger Menu, gather a detailed information which includes not only the transverse momentum or transverse energy but also the location of trigger object. The menu contains different trigger paths, where each path corresponds to a certain criteria for the selection of events.

The triggers based on electron properties are important for studying the Drell-Yan process in dielectron decay channel. In this thesis, since the final state consists of two electrons, dedicated electron triggers are employed. The definition of L1 electron trigger used in the current analysis, requires the presence of an isolated electron object to deposit a minimum transverse energy of 20 GeV in the ECAL. At the HLT level, the trigger condition requires the transverse energy of a loosely identified (average identification and isolation efficiency of $\sim 90\%$) electron deposited in the ECAL, to be greater than 23 GeV.

Chapter 4

Event Simulation and Reconstruction

Event simulation is a vital component in the operation of an experiment. The simulation study of a detector is quite important before and even after the beginning of real data taking. All the reconstruction algorithms, analysis strategies and trigger paths for various processes as well as the operational details of an experiment are well optimized in the simulation process. This helps to understand the performance of different components of the detector and to fine-tune the event generators which is important to check the modeling of detector in the simulation. The experimental output from real data analysis is compared to the simulation study obtained using the Monte-Carlo (MC) method [74], in order to interpret and validate the results.

The general structure of a simulation process consists of the generation of a collision event starting from the proton-proton interaction until the production of final decay products and propagation through different layers of the detector. Physics event generation and detector simulation constitute the earliest steps involved in the event processing chain that leads to MC samples suitable for an analysis. The event generation procedure and the modeling of physics processes is discussed in the following sections.

4.1 Event Generators

The generation of a high energy collision event uses a procedure that is based on the generation of random numbers and probability statistics. Starting with the initial conditions, the event generation is performed by constructing the matrix elements according to the Feynman rules [14] and subsequently calculating the cross section of a process at LO or NLO. The hard interaction often contains parton emissions which emerge from initial and final states and are thus, included in the event generation procedure. Hence, a general structure of the event generator involves the simulation of a hard scattering process, evolving through parton showering and hadronization step and the decay of the unstable particles.

The incoming as well as the outgoing partons of the hard interaction can radiate soft and hard gluons, which can further emit gluons or quark anti-quark pairs by the process known as parton showering. Partons shower until energy scale of the shower reaches an infrared cutoff at which a non-perturbative transformation of colored partons into color-singlets takes place at the hadronization scale. There are various MC event generators that comprise different hadronization treatment. However, the most commonly used fragmentation models in the high energy physics are the Lund String [75–77] and the Cluster [78] model.

The accuracy of MC event generator depends on the choice of its free parameters which must be tuned such that the generator describes the experimental data in the best possible way. This is referred to as generator tuning. Such parameters are available all the way from perturbative domain (hard interaction), to non-perturbative domain (hadronization). The majority of parameters however, are found in the non-perturbative models of physics. A systematic approach to MC tuning is used, to constrain first the perturbative parameters and thereafter the non-perturbative ones. The MC generators that have been used in the present work are illustrated.

4.1.1 MADGRAPH

MADGRAPH [79] is a tool for generating matrix elements for high energy $2 \rightarrow n$ collisions at LO. The event information of the hard process is interfaced with parton shower programs which models the parton showering, hadronization and other steps of event generation. While the previous versions of MADGRAPH were written in FORTRAN77, MADGRAPH5 [80] is written in Python which implements a number of efficient algorithms with improved performance and functionality. It is capable of handling tree-level calculations for any user defined Lagrangian.

There is a method which can match the Parton Shower Monte-Carlo (SMC) generator to the NLO computations of a QCD process. The tool known as MC@NLO [81] has various features for generating fully exclusive events with hadronization using the MC models and computing the total exclusive rates up to NLO accuracy. With this method, a small fraction of negative weights is generated which are handled with an available unweighting technique. A unique framework which merges all the features of MADGRAPH5 and MC@NLO includes several possibilities that can perform NLO plus shower computations, with the MC@NLO formalism. In the current study, MADGRAPH5-AMC@NLO [82] event generator, referred as aMC@NLO, with tune CUETP8M1 [83] has been used and the samples are produced with NNPDF3.0 [39, 40] PDF. The FxFx technique [84] is used to merge the jet multiplicities.

4.1.2 PYTHIA

PYTHIA is a parton shower based MC event generator. The matrix elements are calculated at LO and the higher order processes are modeled by parton showers. The showering is based on DGLAP evolution scheme [32–34] and the emissions are ordered in terms of transverse momentum. The phenomena of hadronization is described using the Lund String model. PYTHIA was originally written in FOR-

TRAN77, called PYTHIA6 [85], while the C++ based version PYTHIA8 [86] was introduced later in 2007 with an improved model for multi-parton interactions. In this thesis, PYTHIA8 with tune CUETP8M1 has been used.

4.1.3 POWHEG

POWHEG [87–90] stands for P*OS*itive Weight Hard Emission Generator. It can generate the hardest emission with a technique that yields events with positive weights using NLO matrix elements. The POWHEG output can be interfaced with any SMC program which allows the modeling of the parton shower and non-perturbative effects. The SMC generator should either be p_T ordered or able to apply a p_T veto so as not to double count the first hard emission when interfacing with the parton shower. In this thesis, POWHEG interfaced with PYTHIA8 has been used for event generation and hadronization.

4.2 Detector Simulation

Simulation of high energy events is the first step in the MC event processing chain. The MC generators discussed in Sec 4.1 model the physics processes only at parton level. To compare the real collision events to the prediction, MC simulation should be available on the detector level providing information on the interaction of particles with the detector material. The primary goal of the simulation program is to efficiently model the interactions involved, the detector performance and the event reconstruction such that simulated events are as close as possible to the real data events. The CMS full simulation is based on GEANT4 [91,92] software toolkit which is interfaced to a wide collection of MC event generators and includes a full event reconstruction.

GEANT4 provides various tools for modeling full detector geometry and sensitive detector response, when a particle is generated in the detector volume by

physics processes including the electromagnetic and the hadronic interactions. It provides interface required for tuning and monitoring the information from tracking of particles through the detector. GEANT4 uses the standard CMS software framework and utilities, described later in the chapter. The simulation program starts with an input provided by the event generators in HEPMC format and then adds to itself the collection of simulated tracks and vertices, hits recorded in each sub-system, digitization data and reconstructed objects. The simulated hits can be overlaid with additional low p_T hadronic events in order to include the effect of pileup. The digitization step involves the modeling of detector electronic response provided by custom code which describes the conversion of the energy deposit in the sensitive elements of the detector into digital signal. The output is the simulated data in a format identical to real collision events which is used to simulate L1 and HLT decisions using the same algorithms implemented online in the CMS Trigger system. The data are then converted in a format which can be processed by the reconstruction algorithms.

In some cases, a parametric approach is used to simulate and reconstruct events with the CMS detector which uses a fast simulation [93] package. In this approach, detector effects are parametrized instead of being simulated as done in full simulation. The purpose of fast simulation is to reduce the CPU time overhead in cases where a huge amount of data need to be produced and the complete simulation of CMS with GEANT4 is rather time consuming. This step generates an output file in a format ready for comparison to the real data.

4.3 Event Reconstruction

In order to perform a precise measurement of particles recorded by the detector, a high quality reconstruction is needed for decay objects. The reconstruction algorithms use information from one or more sub-detectors of the CMS experiment to build different classes of particle candidates.

The process for the CMS event reconstruction is based on local reconstruction within the individual detector modules, global reconstruction inside the whole detector and combination of the two to produce physics objects. The input to the local reconstruction unit is the raw data collected by the detector and the corresponding output is reconstructed hits. These hits known as RecHits are basically position measurements in tracking detectors and calorimetric clusters in calorimeter systems. The RecHits are used as an input to the global reconstruction system in which the information from different sub-detectors is combined within the sub-detector. In the final step, the output from individual sub-detectors is grouped to produce reconstructed objects suitable for physics analysis, for e.g. the electron candidates from calorimeter system are matched to tracks from the tracker system.

This section is dedicated to the study of various reconstruction algorithms and identification criteria of physics objects studied in this analysis along with the software and computing tools used in the CMS. Identification is a method to efficiently distinguish between real physical objects and nonphysical objects, commonly called fakes. The fakes get misreconstructed or mismeasured in the detector for example, a jet depositing its energy in ECAL and hence getting reconstructed as an electron. Every physics object has a set of characteristic variables which can be used for its identification and selection of these is based on the efficiency of signal acceptance and background rejection.

4.3.1 Primary Vertex Reconstruction

With an increase in the instantaneous luminosity at the LHC, there is a likelihood to have more than one hard interactions between partons in the same bunch crossing. Thus, it is necessary to measure precisely the position of these interactions. The offline primary vertex reconstruction is performed in two steps. First, the tracks are selected and grouped in clusters based on the z-coordinate closest to the beam line. The clustering of tracks is performed using the Deterministic Annealing (DA)

method [94]. Second, an iterative reweight fit method is used to perform a three dimensional vertex fit, known as the Adaptive Vertex Fitter. In this fit, each track is assigned a weight w corresponding to the i -th track, defined as $0 \leq w_i \leq 1$. Based on these track weights, each vertex is assigned the number of degrees of freedom ($ndof$). A minimum requirement is to have at least four tracks associated with the vertex, $ndof > 4$. The outcome of the above procedure leads to multiple possibilities for the primary vertex to which further requirements are applied:

- z-position < 24 cm, with respect to the nominal detector center
- r-position < 2 cm, with respect to the beam spot¹⁷

All reconstructed primary vertices are ordered by the sum of squares of transverse momenta $(p_T)^2$ of the tracks associated with each vertex. From the set of these reconstructed vertices, vertex with the maximum sum is chosen as the primary vertex corresponding to the hard process.

4.3.2 Pileup Corrections

The MC samples are generated to match the observed instantaneous luminosity profile. However, due to the increasing luminosity at the LHC, as discussed in Sec. 2.2.2, multiple interactions occur simultaneously which makes it hard to reproduce the same number of reconstructed primary vertices in simulation as observed in data. In order to match the observed distribution of primary vertices in data, the MC samples must be reweighted to mimic the LHC conditions. The reweighting is performed as a function of number of pileup interactions instead of the number of primary vertices, since the distribution of reconstructed primary vertices is sensitive to the implementation of primary vertex reconstruction.

The pileup¹⁸ events in simulation are generated from a distribution of pileup

¹⁷Beam Spot is the luminous region produced by the collisions of proton beams.

¹⁸The pileup in the same bunch crossing is called ‘in time’ pileup while the one in the previous or following bunch crossing is called ‘out of time’ pileup.

events expected in data. For a given range of analyzed runs, the mean number of pileup interactions per bunch crossing is estimated for a given luminosity section using the instantaneous luminosity provided by the LHC, integrated over the entire run range. The obtained distribution is used to reweight the pileup distribution in the MC samples. The weight factor is defined as the ratio of the number of pileup interactions from data (n_{PUI}^{data}) and the number of pileup interactions from simulation (n_{PUI}^{mc}),

$$w_{PUI} = \frac{n_{PUI}^{data}}{n_{PUI}^{mc}} \quad (4.1)$$

4.3.3 Electron Reconstruction

In the study of dielectron invariant mass spectrum, electron reconstruction is the key aspect of the analysis. The electron reconstruction [95, 96] is determined by the measurement of energy deposits in the electromagnetic calorimeter. The reconstruction process gets complicated due to the large material budget in front of the calorimeter which results in high rates of bremsstrahlung emission. The procedure used for the reconstruction of electrons in the CMS is summarized in Fig. 4.1 and discussed in the following sections.

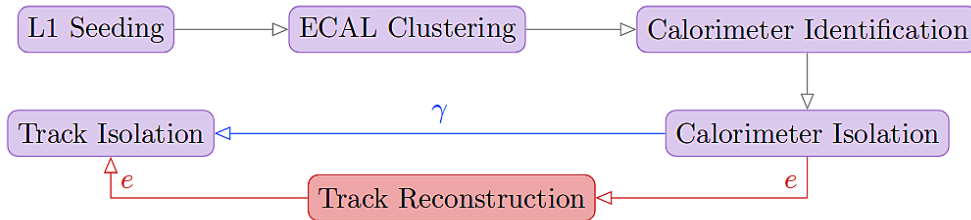


Figure 4.1: Flowchart of the electron reconstruction chain¹⁹.

¹⁹Source : <http://dx.doi.org/10.1088/1742-6596/664/8/082001>

4.3.3.1 Clustering

Electron and photon showers deposit their energy in the ECAL crystals. The reconstruction algorithms are based on the clustering of energy deposits in the crystals and the estimation of position and energy of electrons from this information. The spread in energy deposit depends on the material budget in front of the calorimeter which causes the electrons to undergo bremsstrahlung. In order to measure the actual energy of the electron, energy of radiated photons should be collected. Due to the magnetic field, this energy gets spread in ϕ direction with respect to electron's initial direction, as shown in Fig. 4.2. A dedicated algorithm is used for this purpose which uses different clustering techniques in barrel and endcap regions, due to different geometric arrangement of crystals between the two regions.

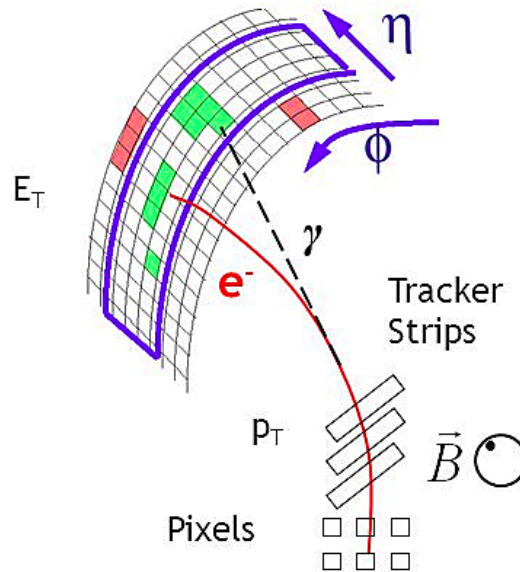


Figure 4.2: Illustration of electron reconstruction²⁰. The electron candidate traverses the pixel and strip tracker, and deposits its energy in the electromagnetic calorimeter. The energy measured in the calorimeter is aligned in η but spread in the ϕ direction due to the axial magnetic field of the CMS detector.

²⁰Source: Lindsey Gray, “ $Z\gamma$ Generator and Background Studies”, <http://slideplayer.com/slide/4495952/>

The Hybrid algorithm in the barrel

The Hybrid algorithm [96] is used in the barrel part of the ECAL detector with a simple $\eta - \phi$ geometry, collecting the electron energy in a small η and an extended ϕ window. It looks for seed crystals which are the local energy maxima with transverse energy above a given threshold $E_{Tseed} > E_{Tseed}^{threshold}$. Crystal dominoes aligned in η with the seed crystal are formed, the central crystal being at the same η_{seed} as of the seed crystal. This procedure is repeated $\pm N_{steps}$ in both ϕ directions around ϕ_{seed} . The domino size is 3x1 or 5x1 in $\eta \times \phi$ plane, depending on the seed crystal energy. The dominoes with energy not greater than $E^{threshold}$ are eliminated and the others are grouped in clusters. The clusters of dominoes are gathered to form superclusters. The domino construction step is illustrated in Fig. 4.3.

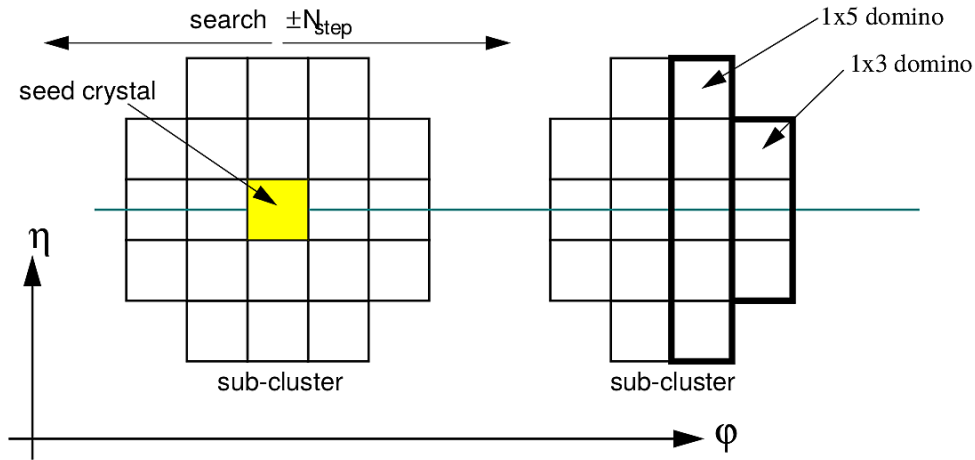


Figure 4.3: Domino construction step in the Hybrid algorithm used in the barrel region of Electromagnetic Calorimeter²¹.

The Multi5x5 algorithm in the endcap

The Mutli5x5 algorithm [96] is used in the endcaps which do not follow the $\eta - \phi$ geometry. The algorithm aims to build fixed size clusters of 5x5 crystal arrays around a seed crystal with a local maximal energy with respect to the surrounding four

²¹Source : <https://cds.cern.ch/record/687345>

neighbouring crystals, which verifies $E_{Tseed} > E_{Tcluster}^{threshold}$. The 5x5 crystals are then grouped if their transverse energy is above a given threshold, $E_{Tcluster} > E_{Tcluster}^{threshold}$ aligned in η and ϕ with the seed cluster within $\Delta\eta$ - $\Delta\phi$ window. The preshower energies corresponding to the 5x5 clusters are added to the supercluster energy.

The total supercluster energy is computed from the sum of energies of individual crystals which form the supercluster (sub-clusters) and the position is obtained from the energy weighted mean of the sub-clusters.

4.3.3.2 Track Reconstruction and Charge Determination

The electron track reconstruction should be able to collect hits in the tracker and access the parameters of the track associated with the energy deposited in the ECAL. The tracking algorithm is designed and tuned to perform the reconstruction of a track that is found to be compatible with the supercluster information.

The first step in the electron track reconstruction is the trajectory seeding. It consists of finding a pair of hits or triplet, called a seed, in the pixel detector, which is compatible with the energy and position of the supercluster. Two algorithms are used for this purpose: the ECALDriven seeding starts from the supercluster and back-propagates the trajectory followed in the magnetic field, towards the inner layers of the pixel detector; the TrackerDriven seeding starts from the trajectory seeds extrapolated towards the supercluster.

The TrackerDriven algorithm used in the current analysis starts with the tracks reconstructed using a Kalman Filter (KF) method [97], which proceeds through each layer of the silicon tracker and adds measured hits in the subsequent layer, consistent with the propagated trajectory. The electron energy losses are modeled using a dedicated Bethe-Heitler function [98]. To account for the high rate of bremsstrahlung emission and to improve the track finding efficiency, a very loose requirement on the track hit position compatibility with the prediction is used. Since the KF is unable to follow the change in curvature of the electron trajectory due to the emission of

photon radiations, a Gaussian Sum Filter (GSF) [99] fit to the KF track is performed in order to estimate the track parameters.

The GSF is a non-linear generalization of the KF, which describes the distributions of all errors as a Gaussian mixture. This method approximates the loss of energy in each layer with a mixture of Gaussian distributions rather than a single Gaussian. To each Gaussian distribution a weight describing the associated probability is attributed. The hits are collected efficiently along the full trajectory, at both ends of the track which yields a good estimation of the track parameters at the ECAL entrance. The GSF filter is applied to all the track hit candidates in both directions, outside-in and inside-out, which helps in the evaluation of the fractional energy carried away by the bremsstrahlung photons from outermost and innermost track parameters.

The electron charge determination [96] suffers from the bremsstrahlung radiation and photon conversions. In order to minimize the misidentification rate, the electron charge is evaluated by combining several charge estimates using: the GSF track curvature, the associated KF track matched with the GSF track, and the relative position of supercluster and the innermost tracker hit. The charge of the electron candidate is obtained as the value given by two out of the three methods in agreement.

4.3.4 Energy Scale

The measurement of electron energy provided by the supercluster algorithms is obtained by adding the deposits measured in the ECAL crystals. The ϕ spread of the energy depends on the amount of radiations emitted by the electron due to the interactions with tracker material before reaching ECAL. The reconstructed energy, E_{meas}/E_{true} has a peak at a few percent less than unity due to the unrecovered energy from bremsstrahlung emission resulting in discrepancies between data and simulated energy. These discrepancies depend on the detector conditions and the quality of

electrons, as they vary differently for different regions of the ECAL detector. Hence, the electron energy scale is corrected such that the mass of Z boson agrees well between data and simulation. These corrections are obtained using the standard CMS technique and the detailed description can be found in [100].

4.3.5 Electron Selection Strategy

In physics analyses with dielectron final state, it is crucial to identify isolated signal electrons and separate them from the background electrons, mainly originating from photon conversion or jets faking electrons. The high magnetic field and a tracker with thick material have a great impact on the electron selection. The following section describes the strategies developed in CMS for the identification and isolation of electrons.

4.3.5.1 Identification

Electron identification is based on simple algorithms which use a set of discriminating variables to distinguish between real and background electrons. Three main categories of variables are used. The pure calorimetric observables which help in separating real electrons from objects like jets in the electromagnetic component. These variables differ from the hadronic jets in the shape of electromagnetic shower and hence, based on the shower shape in the ECAL. The pure tracking observables which help to discriminate between electrons and charged hadrons and make use of the tracking information provided by the KF and the GSF. Lastly, the track-cluster matching observables which require consistent information between the ECAL and the tracker. The matching can either be geometrical or based on the comparison between the energy deposit in the ECAL (supercluster) and the momentum of track (GSF track). A cut based selection is applied on the variables described hereafter:

- H/E : Ratio between the energy deposits in HCAL and ECAL.

- $\sigma_{i\eta i\eta}$: Calorimeter shower shape variable, measures the spread in η for the energy deposited inside a 5x5 ECAL crystal matrix that is centered on the highest energy crystal of the supercluster.
- E/p_{in} , E_{seed}/p_{in} and E_{seed}/p_{out} : Energy-momentum matching variables between the total energy of the supercluster (E) or the supercluster seed (E_{seed}) and the momentum of the track measured at the vertex (p_{in}) or the calorimeter entrance (p_{out}).
- $\Delta\eta$ and $\Delta\phi$: Geometrical matching between the supercluster position in the ECAL and the direction of track at the vertex extrapolated to the supercluster.
- d_0 and d_z : Transverse and longitudinal impact parameter of the electron track with respect to the reconstructed primary vertex.

A criteria for the rejection of secondary electrons originating from the bremsstrahlung emission due to high photon conversion rates and the separation of converted photons from a prompt electron is also applied:

- *Missing Hits*: Number of crossed layers without compatible hits in the innermost tracker layers.
- *Conversion Veto*: A veto to reject the electrons from converted photons.

4.3.5.2 Isolation Requirement

A large fraction of real to fake electrons exist due to the misidentification of electrons as jets. The electron candidates have a considerable flow of energy around them and isolating these electrons from nearby activity of charged particles or energy deposits can reduce the contamination from these background sources. The tracks are matched to calorimeter deposits which allows the individual tracks to be identified as objects like electrons or charged hadrons, where as the unmatched

calorimeter deposits are identified as photons or neutral hadrons. This procedure known as the Particle Flow (PF) algorithm [101, 102] results in a global description of an event with all the particles reconstructed. These PF candidates are used for defining the isolation variables for the electron. A cone is defined in the $\eta - \phi$ coordinate space around the direction of electron with a requirement to have $\Delta R = \sqrt{(\Delta\eta)^2 + (\Delta\phi)^2} < R_0$, where R_0 is defined to be 0.3 or 0.4. Three different observables based on the type of reconstructed particles are used to define the isolation requirement on the electron: charged particles, photons and neutral hadrons. Once the three isolation observables are obtained, these are summed to form an isolation quantity which is required to be less than some fraction of electron p_T . The particle flow isolation (Iso) is then defined as following:

$$\text{Iso} = \sum p_T^{\text{charged had}} + \max\left(\sum p_T^{\text{neutral had}} + \sum p_T^\gamma - A_{eff} \cdot \rho, 0\right) \quad (4.2)$$

here, the sums run over the charged particles originating from the primary vertex and on the neutral particles, including hadrons and photons both.

The isolation variables are quite sensitive to the extra energy in the event due to pileup, which can affect the isolation efficiency at high number of interactions in a bunch crossing. However, once the candidates compatible with the primary vertex are chosen, charged candidate becomes independent of the pileup effect. In order to remove this effect for the neutral candidates of isolation, a correction ($\rho \cdot A_{eff}$) is applied by using the average energy density (ρ) and effective area (A_{eff}) which normalizes the estimator such that the neutral candidates become independent of the number of pileup interactions. This procedure uses the FASTJET technique [103–105] which performs reconstruction of jets using the anti- k_T jet clustering algorithm [106].

4.3.6 Software and Computing

The CMS software and computing system aims to cover a broad range of activities including the design, construction and calibration of the detector; the storage, reconstruction and analysis of data.

4.3.6.1 CMSSW

The collection of software used in the CMS, referred to as CMSSW [107] consists of a number of sub-packages which are created to provide an extensive toolkit to perform software related tasks. The CMSSW software is built around a framework, called the Event Data Model (EDM), and services needed by the simulation and reconstruction modules that process the event data which can be used by physicists to perform data analysis. These modules can be plugged into the software framework during run time, with no dependence on the computing environment. The model is centered around the concept of an Event that is based on C++ object-oriented methodology and passes information from one module to another, during data processing.

4.3.6.2 ROOT

ROOT is a software framework designed at CERN for performing data processing and statistical analysis. It is an object-oriented programming that has been written in C++ and integrated with other languages like Python. ROOT is very flexible and provides a programming interface which can be used in applications as well as a graphical user interface for performing interactive data analysis. There are many pre-defined classes and methods available in ROOT, which help to quickly access large amounts of data using the C++ interpreter. It has a wide range of applications, including histogram making to view and analyze distributions and functions, curve fitting, storing data in the form of ROOT files, various mathematical and statistical tools for data operation.

4.3.6.3 Computing Model

To store a huge amount of data produced at the LHC, the computing environment has been constructed as a distributed computing and data storage infrastructure, known as the Worldwide LHC Computing Grid (WLCG) [108]. The set of grid services comprise the computing and connectivity resources which are used by the CMS to perform data processing, MC event generation and all types of computing-related activities. The CMS computing model constitutes a primary Tier-0 centre at CERN along with Tier-1 and Tier-2/3 computing centres at various national laboratories and universities worldwide, as shown in Fig. 4.4. The raw collision data collected by the CMS detector is converted into primary datasets based on trigger information and stored in the Tier-0 site at CERN. The processed data is then transferred to the Tier-1 centre which runs various reconstruction algorithms on the primary data. The reconstructed and simulated data is further distributed to Tier-2/3 sites, where it is used by the analysts for performing physics analyses.

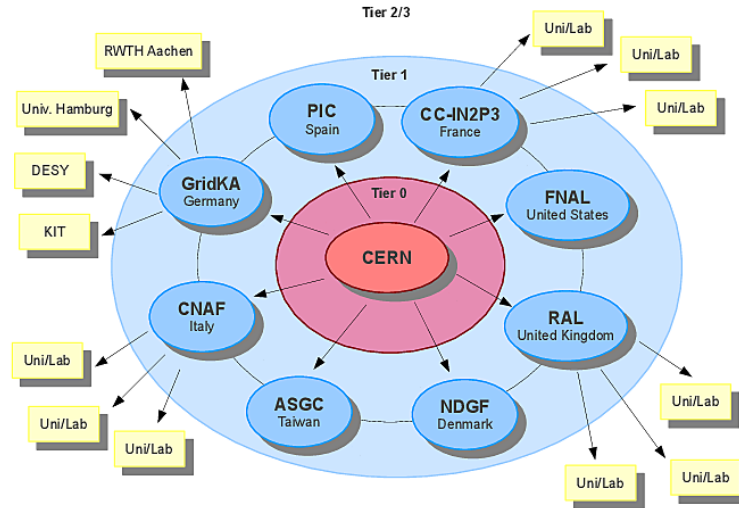


Figure 4.4: The schematic overview of the CMS computing model. The data collected by CMS is stored in the Tier-0 site at CERN which is transferred to various Tier-1 centres. The reconstructed and simulated data is further distributed to Tier-2/3 sites, where it is available for physics analysis. Taken from [108].

Chapter 5

Measurement of Drell-Yan Differential Cross section

In high energy particle physics, the cross section measurement provides the probability of collision of two particles. This chapter describes the Drell-Yan (DY) differential cross section measurement performed in the bins of dielectron invariant mass $d\sigma/dm$ within the range $15 < m < 3000$ GeV. The differential cross section is measured at a center-of-mass energy $\sqrt{s} = 13$ TeV using an integrated luminosity of 2.3 fb^{-1} of proton-proton collision data collected using the CMS detector at the LHC during the year 2015.

The cross section per mass bin is calculated using the following formula:

$$\sigma^i = \frac{N_u^i}{A^i \cdot \epsilon^i \cdot \rho^i \cdot \mathcal{L}_{int}} \quad (5.1)$$

where, each quantity is calculated in a given invariant mass bin i . N_u^i denotes the background subtracted yield corrected for the detector resolution and final-state radiation (FSR) effects, A^i and ϵ^i are the acceptance and efficiency for signal events, ρ^i is the efficiency scale factor and \mathcal{L}_{int} is the integrated luminosity of 2015 dataset.

5.1 Data and Monte-Carlo Samples

The measurement of the differential cross section presented in this chapter is based on the understanding of signal and background processes. MC samples are used for the determination of efficiencies, acceptances and various systematic errors and to validate the data-driven techniques which are used to estimate and perform the background study in this analysis. These samples are generated using a variety of generators and processed with the CMS detector simulation based on GEANT4, including the trigger simulation and a full chain of event reconstruction, as in Sec. 4.3.

5.1.1 Collision Data

The data sample used in this analysis is based on proton-proton collisions recorded in 2015 with the CMS detector at a center-of-mass energy $\sqrt{s} = 13$ TeV. A list of data samples is provided in Table 5.1. The data events collected using single electron triggers during 2015 runs are analyzed. The recorded data correspond to an integrated luminosity of 2.3 fb^{-1} .

Table 5.1: Names of the single electron data samples used in the Drell-Yan analysis.

Dataset	Run range
/SingleElectron/Run2015C_25ns-16Dec2015-v1/MINIAOD	254227-254914
/SingleElectron/Run2015D-16Dec2015-v1/MINIAOD	256630-260627

5.1.2 Drell-Yan Signal

The DY signal is manifested by the presence of two isolated, well reconstructed and identified electrons as shown in Fig. 5.1. The DY signal samples are simulated using the aMC@NLO generator and are split into eleven different samples based on the invariant mass of the dilepton. A list of signal samples used in this analysis is provided in the Table 5.2. The 50 GeV DY sample is simulated without any upper

limit on the mass of two reconstructed electrons. Hence, a cut ($m < 100$ GeV) is applied on the dielectron mass in order to truncate this sample at 100 GeV, such that it can be combined with the next sample having reconstructed mass in the range 100-200 GeV. Figure 5.2 shows the generator-level dielectron mass distribution obtained after combining all the DY samples used in this analysis and normalized to the integrated luminosity.

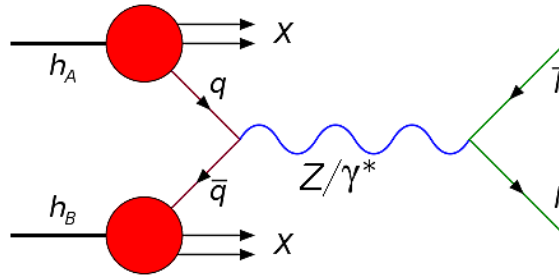


Figure 5.1: Leading order Feynman diagram of Drell-Yan process²².

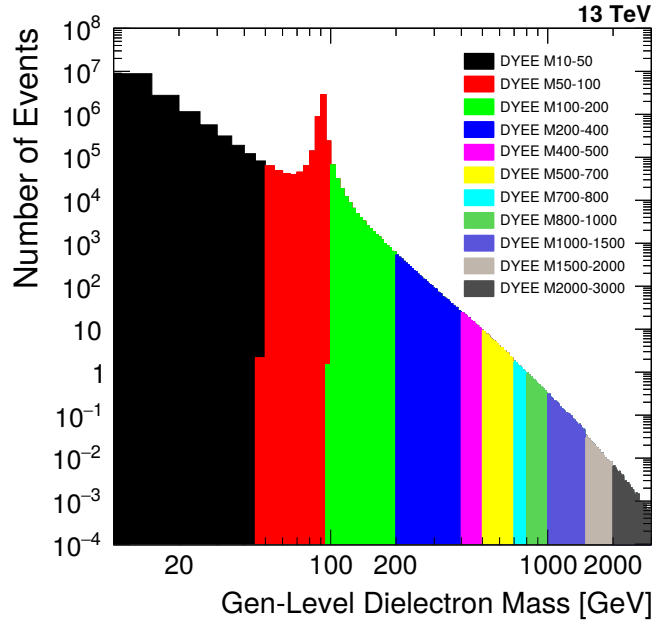


Figure 5.2: Generator-level mass distribution of the Drell-Yan signal sample.

²²Source : https://en.wikipedia.org/wiki/Drell-Yan_process

Table 5.2: Names of the datasets and corresponding cross section values [109] for the Monte-Carlo signal and background samples used in the Drell-Yan analysis.

Process	Sample	σ (pb)
$DY \rightarrow \ell\ell$	/DYJetsToLL_M-10to50_TuneCUETP8M1_13TeV-amcatnloFXFX-pythia8/RunIIFall15 MiniAODv2-PU25nsData2015v1_76X_mcRun2_asymptotic_v12_ext3-v1/MINIAODSIM	18610
	/DYJetsToLL_M-50_TuneCUETP8M1_13TeV-amcatnloFXFX-pythia8/RunIIFall15 MiniAODv2-PU25nsData2015v1_76X_mcRun2_asymptotic_v12-v1/MINIAODSIM	6025.2
	/DYJetsToLL_M-100to200_TuneCUETP8M1_13TeV-amcatnloFXFX-pythia8/RunIIFall15 MiniAODv2-PU25nsData2015v1_76X_mcRun2_asymptotic_v12_ext1-v1/MINIAODSIM	226
	/DYJetsToLL_M-200to400_TuneCUETP8M1_13TeV-amcatnloFXFX-pythia8/RunIIFall15 MiniAODv2-PU25nsData2015v1_76X_mcRun2_asymptotic_v12_ext1-v1/MINIAODSIM	7.67
	/DYJetsToLL_M-400to500_TuneCUETP8M1_13TeV-amcatnloFXFX-pythia8/RunIIFall15 MiniAODv2-PU25nsData2015v1_76X_mcRun2_asymptotic_v12_ext1-v1/MINIAODSIM	0.423
	/DYJetsToLL_M-500to700_TuneCUETP8M1_13TeV-amcatnloFXFX-pythia8/RunIIFall15 MiniAODv2-PU25nsData2015v1_76X_mcRun2_asymptotic_v12_ext1-v1/MINIAODSIM	0.24
	/DYJetsToLL_M-700to800_TuneCUETP8M1_13TeV-amcatnloFXFX-pythia8/RunIIFall15 MiniAODv2-PU25nsData2015v1_76X_mcRun2_asymptotic_v12_ext1-v1/MINIAODSIM	0.035
	/DYJetsToLL_M-800to1000_TuneCUETP8M1_13TeV-amcatnloFXFX-pythia8/RunIIFall15 MiniAODv2-PU25nsData2015v1_76X_mcRun2_asymptotic_v12_ext1-v1/MINIAODSIM	0.03
	/DYJetsToLL_M-1000to1500_TuneCUETP8M1_13TeV-amcatnloFXFX-pythia8/RunIIFall15 MiniAODv2-PU25nsData2015v1_76X_mcRun2_asymptotic_v12_ext1-v1/MINIAODSIM	0.016
	/DYJetsToLL_M-1500to2000_TuneCUETP8M1_13TeV-amcatnloFXFX-pythia8/RunIIFall15 MiniAODv2-PU25nsData2015v1_76X_mcRun2_asymptotic_v12_ext1-v1/MINIAODSIM	0.002
	/DYJetsToLL_M-2000to3000_TuneCUETP8M1_13TeV-amcatnloFXFX-pythia8/RunIIFall15 MiniAODv2-PU25nsData2015v1_76X_mcRun2_asymptotic_v12_ext1-v1/MINIAODSIM	0.00054
$t\bar{t}$	/TT_TuneCUETP8M1_13TeV-powheg-pythia8/RunIIFall15 MiniAODv2-PU25nsData2015v1_76X_mcRun2_asymptotic_v12_ext3-v1/MINIAODSIM	831.76
tW	/ST_tW_top_5f_inclusiveDecays_13TeV-powheg-pythia8_TuneCUETP8M1/RunIIFall15 MiniAODv2-PU25nsData2015v1_76X_mcRun2_asymptotic_v12-v1/MINIAODSIM	38.09
$\bar{t}W$	/ST_tW_antitop_5f_inclusiveDecays_13TeV-powheg-pythia8_TuneCUETP8M1/RunIIFall15 MiniAODv2-PU25nsData2015v1_76X_mcRun2_asymptotic_v12-v1/MINIAODSIM	38.09
WW	/WW_TuneCUETP8M1_13TeV-pythia8/RunIIFall15 MiniAODv2-PU25nsData2015v1_76X_mcRun2_asymptotic_v12-v1/MINIAODSIM	118.7
WZ	/WZ_TuneCUETP8M1_13TeV-pythia8/RunIIFall15 MiniAODv2-PU25nsData2015v1_76X_mcRun2_asymptotic_v12-v1/MINIAODSIM	47.13
ZZ	/ZZ_TuneCUETP8M1_13TeV-pythia8/RunIIFall15 MiniAODv2-PU25nsData2015v1_76X_mcRun2_asymptotic_v12-v1/MINIAODSIM	16.523
W +jets	/WJetsToLNu_TuneCUETP8M1_13TeV-amcatnloFXFX-pythia8/RunIIFall15 MiniAODv2-PU25nsData2015v1_76X_mcRun2_asymptotic_v12-v1/MINIAODSIM	61526

5.1.3 Background Processes

Various physical processes that have same signature in the final state can be misidentified as DY electrons and are considered as background processes. A large contamination from these processes can be reduced with well chosen selection requirements. However, the remaining background contribution needs to be handled properly in

order to differentiate it from the signal. Different background processes which play an important part in this analysis can be classified into following categories:

- The true dielectron backgrounds which have two real electrons in the final state. This background category contains the electroweak processes namely $DY \rightarrow \tau\tau$, top production ($t\bar{t}$, single-top) and dibosons (WW , WZ , ZZ).
- The fake electron backgrounds which have at least one jet faking a real electron. This background category contains QCD multijet and W +jets.
- The photon-initiated (PI) background process in which the photons radiated by the initial-state partons get misreconstructed as electrons.

The various background processes with corresponding production Feynman diagrams are described below.

$DY \rightarrow \tau\tau$

The leptonic decay $\tau \rightarrow \nu_\tau e \nu_e$ has a branching ratio of 17%. The real electrons coming from $DY \rightarrow \tau\tau$ have an invariant mass lower than m_Z opposed to the direct decay of Z boson into two electrons ($Z \rightarrow ee$). Hence, this background is a dominant source in the low and intermediate mass region $\sim 15 < M_{ee} < 70$ GeV. The leading order Feynman diagram of this process is shown in Fig. 5.3.

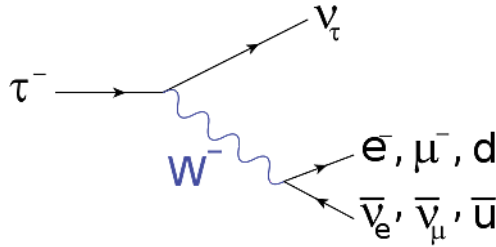


Figure 5.3: Leading order Feynman diagram for τ decay²³.

²³Source : [https://en.wikipedia.org/wiki/Tau_\(particle\)](https://en.wikipedia.org/wiki/Tau_(particle))

$t\bar{t}$ decay

The dominant top quark production channel at LHC is the pair-production of top-antitop quark pair ($t\bar{t}$) as seen in Fig. 5.4 which represents the leading order Feynman diagram of $t\bar{t}$ production. The top quark decays into a W boson in association with a bottom quark. The final state of $t\bar{t}$ decay consists of missing transverse energy and two well identified real electrons from the decay of W bosons. This is a dominant background process in the high mass region of the DY mass spectrum.

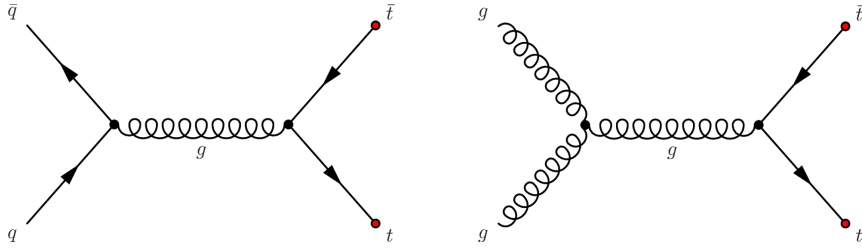


Figure 5.4: Leading order Feynman diagram for the $t\bar{t}$ pair production²⁴.

Single-top production and decay

The production diagrams of top quark via weak interaction are shown in Fig. 5.5 and include s -channel, t -channel and tW -channel²⁵ production. The maximum contribution comes from tW ($\bar{t}W$) processes which lead to the production of two electrons via the leptonic decay of W boson. However, this background is minimal with a small contribution to the mass spectrum.

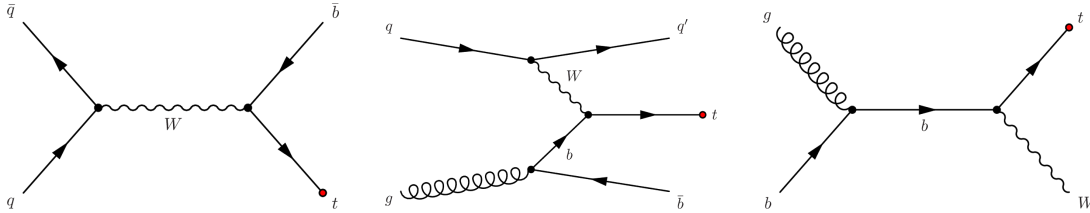


Figure 5.5: Leading order Feynman diagrams of the single top processes. From left to right: s -channel, t -channel and tW -channel²⁶.

²⁴Source : https://en.wikipedia.org/wiki/Top_quark

²⁵The production of single top quarks via weak interaction can take place in several ways defined as channels.

²⁶Source : https://en.wikipedia.org/wiki/Top_quark

Dibosons

The diboson processes WW , WZ and ZZ constitute the irreducible background to this analysis. These processes decay with two real electrons in the final state from $Z \rightarrow ee$ or $W \rightarrow e\nu$. However, since the cross section of these processes is not large, the fraction of background contribution is relatively small. The diboson production from $q\bar{q}$ is shown in Fig. 5.6.

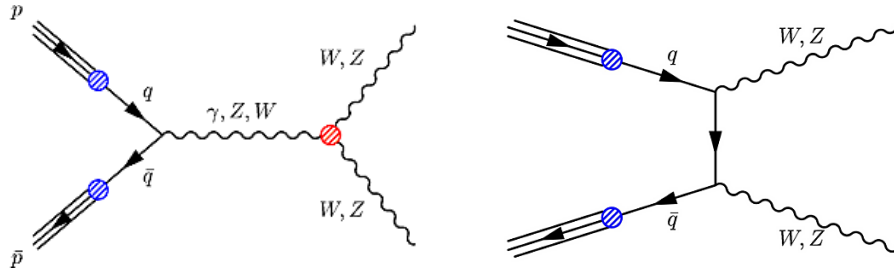


Figure 5.6: Leading order Feynman diagram for diboson production contributions from s-channel (left) and t-channel (right)²⁷.

W +jets

This is a sub-dominant background process which can be reduced by the selection requirement. The production of W +jets process is described in Fig. 5.7. The W boson decaying leptonically to an electron along with missing transverse energy can be a background source when the associated jet fakes an electron.

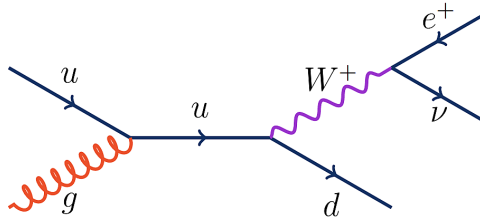


Figure 5.7: Leading order Feynman diagram for W +jets production²⁸.

²⁷Source : <https://www-cdf.fnal.gov/physics/ewk/2008/WZatgc/>

²⁸Source : <http://cds.cern.ch/record/1376067>

QCD hadronic decay

With a large production rate at the LHC energy, the QCD process becomes an important background to this analysis. The QCD events with multiple jets contribute maximally at the low DY invariant mass region and dedicated techniques are used in order to remove the contamination from jets. However, since these events do not survive the dielectron selection thresholds, they get highly suppressed at the event selection stage.

A list of background samples relevant to this analysis are listed in Table 5.2. All samples are processed using PYTHIA8 or POWHEG, except the W +jets background sample which is generated with aMC@NLO.

5.2 Reweightings

There exist several corrections which improve the agreement between data and simulation and lead to a precise measurement of the DY differential cross section, hence form an important part of this study. These corrections and reweight techniques have already been described in the previous chapters and will be discussed in more detail in this section.

5.2.1 Pileup Reweighting

The simulation does not reproduce the distribution of the number of reconstructed primary vertices as observed in data since the pileup depends on the beam conditions which are unknown during MC sample generation.

As discussed in Sec. 4.3.2, a weight factor is applied to the events in order to correct the MC distribution. These corrections applied as an event weight to the MC are calculated from the distribution of number of pileup interactions in the data and simulation using the standard technique followed by the CMS. This technique considers a MB cross section of 69.0 mb at $\sqrt{s} = 13$ TeV.

Figure 5.8 compares the number of primary vertices in data and MC samples used in this analysis. It can be seen that, the pileup reweighting considerably improves the data-MC agreement.

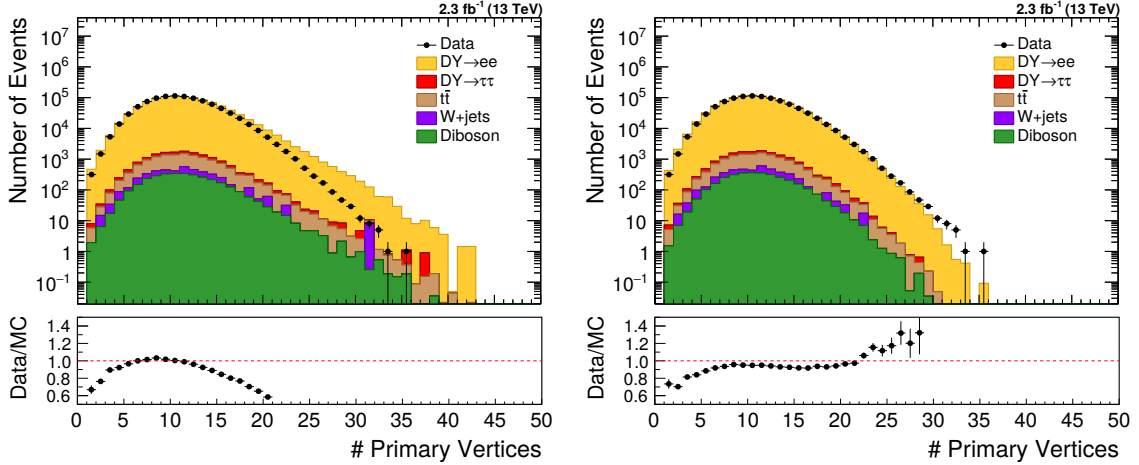


Figure 5.8: The distribution for number of reconstructed primary vertices in data (black circles) and Monte-Carlo prediction (stacked histograms) before (left) and after (right) applying the pileup reweighting.

5.2.2 Scale Corrections

The electron energy is obtained primarily from the measurement of the energy deposited by electrons in the ECAL. The energy deposition depends on the alignment, synchronization and other aspects of detector operation which can affect the reconstruction of dielectron invariant mass. In order to recover the difference between data and MC simulation, the electron energy scale is corrected as discussed in detail in Sec. 4.3.4.

The effect of these corrections is visible in the Z -peak region and can be seen in Fig. 5.9. The data/MC ratio plot shows a better agreement between data and simulation after the energy scale corrections are applied.

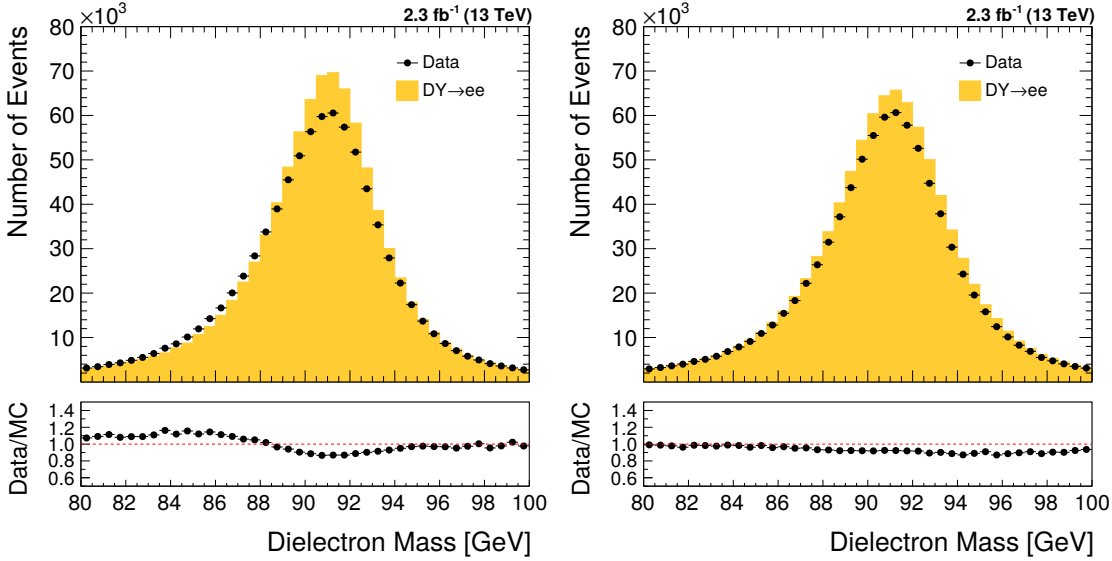


Figure 5.9: The left and right plots show the mass distribution for the Z -peak region, before and after applying the energy scale and smearing corrections, respectively for data (black circles) and Monte-Carlo prediction (yellow histogram). The Drell-Yan signal is normalized to the number of data events.

5.3 Drell-Yan Event Selection

The selection of dielectron events for the DY cross section measurement begins with a requirement to pass the unprescaled²⁹ trigger having a minimum threshold on the transverse momentum (p_T) of electron candidate. The single electron trigger *HLT_Ele23_WPLoose_Gsf*, with a p_T requirement of 23 GeV on loosely identified GSF electron is used to select the signal events. In order to tighten the selection criteria, a trigger matching is implemented between offline electron selected by the single electron trigger and HLT object. The $\Delta R = \sqrt{(\Delta\eta)^2 + (\Delta\phi)^2}$ is required to be within 0.1 for either of the two electrons by applying an ‘OR’ condition. This ensures purity of the sample used to perform the cross section measurement.

In order to reduce the backgrounds at the event selection stage, various kinematical and identification requirements are imposed on the electron candidates.

²⁹The HLT algorithms depend on the expected instantaneous luminosity and need a prescale factor in order to reduce the output rate for high luminosity runs.

Kinematics

The leading electron in the event is required to have $p_T > 30$ GeV and the sub-leading electron $p_T > 10$ GeV. The p_T cut on the leading electron allows to operate on the plateau region of the trigger efficiency. The ECAL fiducial region is obtained from the pseudo-rapidity of the supercluster (η_{sc}) with $|\eta_{sc}| < 1.4442$ (barrel) and $1.566 < |\eta_{sc}| < 2.5$ (endcap). The barrel-endcap gap region ($1.4442 < |\eta_{sc}| < 1.566$) is partially shadowed by cables and therefore have degraded resolution and efficiency. The transition region is hence, excluded in this analysis.

Identification

The electrons are identified using a set of cuts applied on the discriminating variables, discussed in detail in Sec. 4.3.5.1. The variables determine the characteristics of calorimeter and tracker. These are based on the distribution of electromagnetic shower shape in the ECAL, a matching trajectory of an electron track with the clusters in the ECAL and consistency with the origin of the track from the primary vertex in order to reduce the misidentification rate. The cut values are defined separately for the barrel and endcap regions of the calorimeter and are summarized in the Table 5.3. This analysis uses the Medium Working Point (WP) [110] for the identification of electrons with a requirement to pass the particle flow isolation, discussed in Sec. 4.3.5.2, defined within a cone of $\Delta R < 0.3$ around the direction of electron. The distribution for various identification variables is presented in Fig. 5.10.

In Fig. 5.11 and 5.12, the kinematic variables p_T , η (y) and ϕ of the electrons (dielectrons) are presented. The electron yields from data and MC events obtained in the bins of dielectron invariant mass can be seen in Fig. 5.13. These plots represent the detector level information after correcting for electron energy scale and pileup effects as discussed in Sec. 5.2. A good agreement is observed between data and MC prediction.

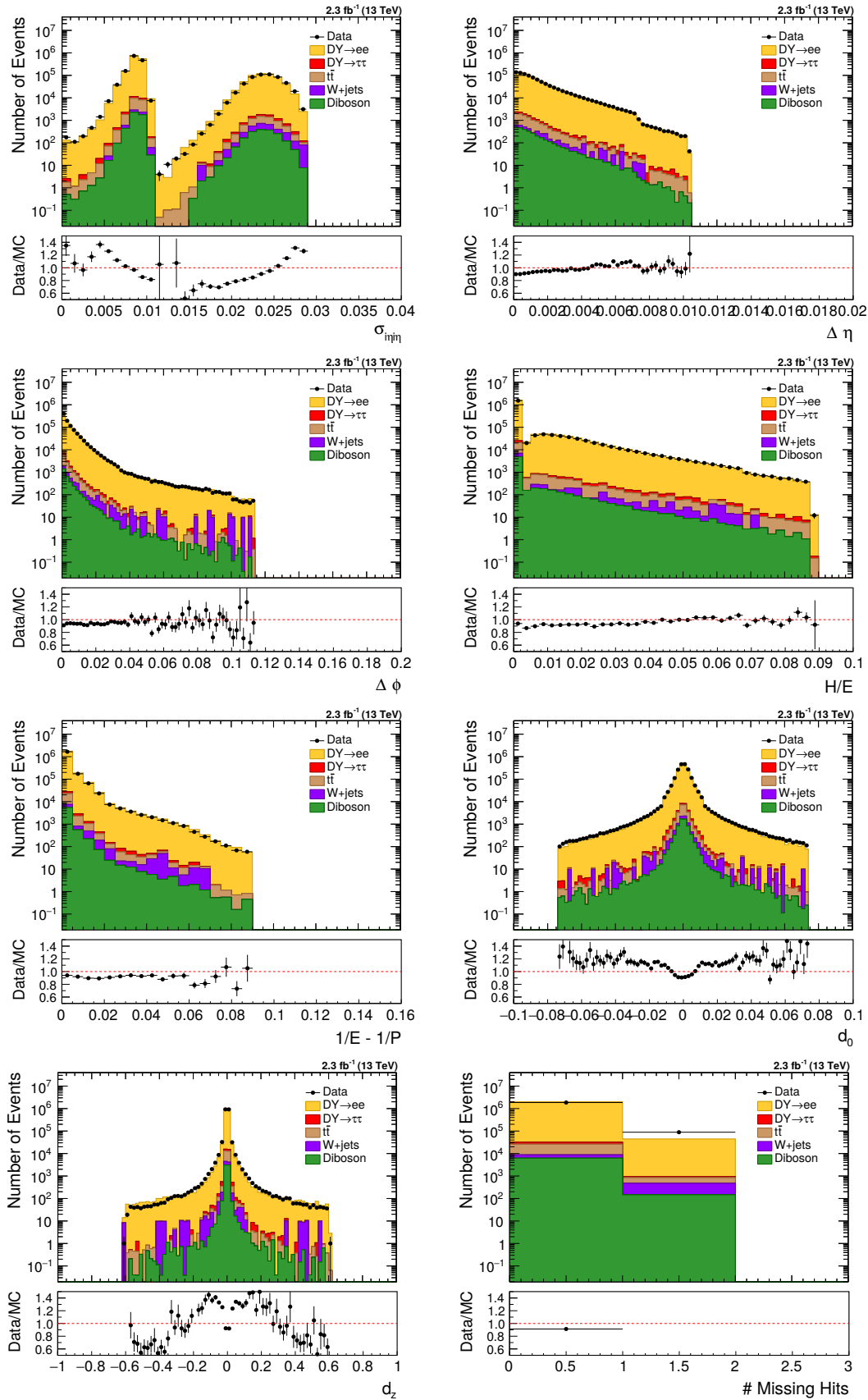


Figure 5.10: Electron identification variables for data (black circles) and Monte-Carlo prediction (stacked histograms) listed in Table 5.3.

Table 5.3: Summary of Medium Working Point for the electron identification [110] using cut-based approach in the barrel and endcap regions.

Variable	Barrel	Endcap
$\sigma_{i\eta i\eta} <$	0.0101	0.0283
$\Delta\eta_{\text{In}} <$	0.0103	0.00733
$\Delta\phi_{\text{In}} <$	0.0336	0.114
$H/E <$	0.0876	0.0678
PF Isolation $<$	0.0766	0.0678
$1/E - 1/P <$	0.0174	0.0898
$ d_0 <$	0.0118	0.0739
$ d_z <$	0.373	0.602
Missing Inner Hits \leq	2	1
Pass Conversion Veto	yes	yes

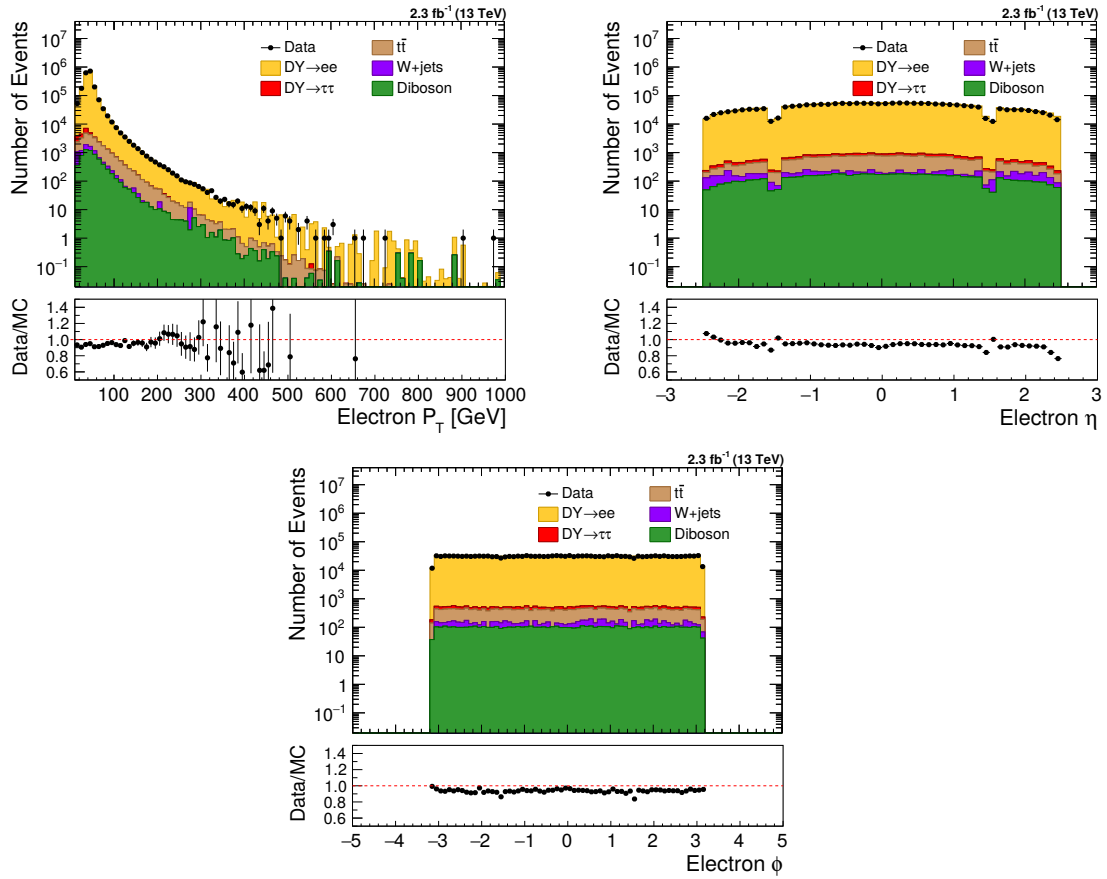


Figure 5.11: Electron kinematic variables p_T , η and ϕ after pre-selection (kinematic and identification cuts) in data (black circles) and Monte-Carlo prediction (stacked histograms).

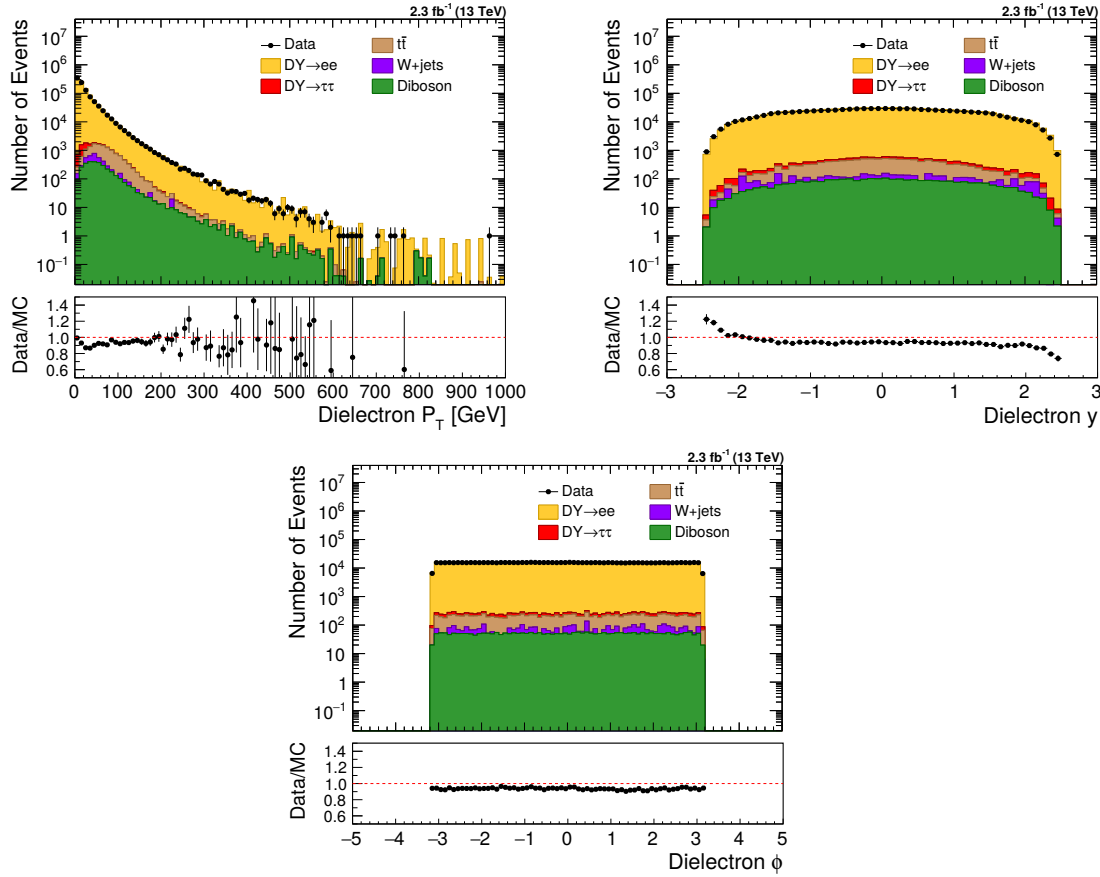


Figure 5.12: Dielectron kinematic variables p_T , y and ϕ after pre-selection (kinematic and identification cuts) in data (black circles) and Monte-Carlo prediction (stacked histograms).

5.4 Background Estimation

The potential sources of background in the DY analysis can be seen in Fig. 5.13. The composition of these backgrounds depends on the dielectron invariant mass region. From the MC prediction, dominant contribution over the entire mass range comes from $t\bar{t}$ whereas the production of $\tau\tau$ pairs from the DY process contributes maximal in the low mass region up to ~ 70 GeV. Other backgrounds with comparatively smaller contributions include dibosons (WW , WZ and ZZ), single-top (tW and $\bar{t}W$), QCD and W +jets as already discussed in Sec. 5.1.3. The prediction for these backgrounds is fairly reliable and we can consider using the MC prediction

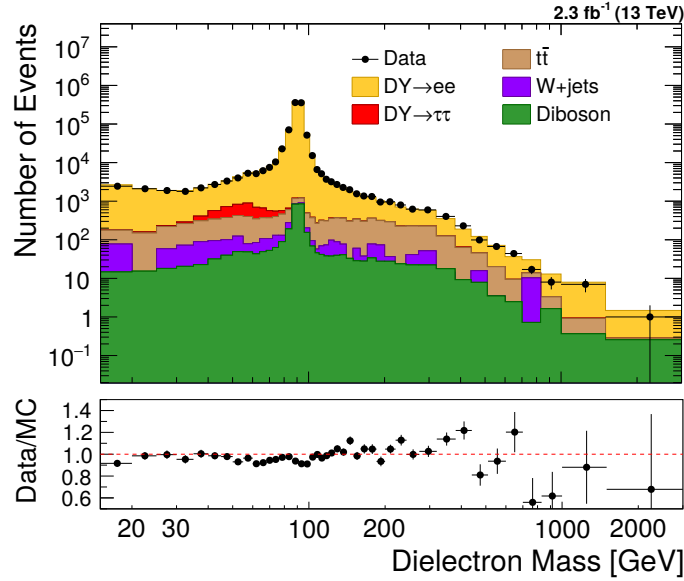


Figure 5.13: Drell-Yan mass distribution in data (black circles) and Monte-Carlo prediction (stacked histograms) in the dielectron invariant mass range 15 GeV to 3000 GeV.

for background subtraction in order to obtain the signal yield. However, the data-driven techniques are used to cross-check the level of background from the MC-based analysis and to assess the systematic errors described later.

5.4.1 Measurement of Dielectron Background using $e\mu$ Method

The data-driven technique which is based on the reconstruction of $e\mu$ pairs is used to estimate the true electron background sources namely top quark production (single or in pairs), WW and $DY \rightarrow \tau\tau$. These background processes being flavour symmetric, decay to $e\mu$ pair at twice the rate of dielectron events and hence the contribution of dielectron backgrounds can be scaled properly by the $e\mu$ events after accounting for detector acceptance and efficiency. The W +jets background which contains only one real electron can mimic $e\mu$ final state and thus treated as a background to the $e\mu$ events.

The relationship between the number of e^+e^- and $e\mu$ events can be expressed as:

$$N_{e^+e^-}^{Est} = \frac{A}{2} \cdot \frac{1}{1+R} \cdot N_{e\mu}^{Obs} \quad (5.2)$$

where,

- $A = 2N_{ee}/N_{e\mu}$, N_{ee} and $N_{e\mu}$ are the numbers of e^+e^- and $e\mu$ events reconstructed in MC. Therefore, A is a ratio of detector acceptance times efficiency for e^+e^- relative to $e\mu$ selection.
- R is the ratio of W +jets background to $e\mu$ events, i.e. $(N_{W+jets})/(N_{DY \rightarrow \tau\tau} + N_{t\bar{t}} + N_{tW} + N_{\bar{t}W} + N_{WW})$. $R = 0$ when there is no $e\mu$ background.
- $N_{e\mu}^{Obs}$ is the observed number of $e\mu$ events in data and $N_{e^+e^-}^{Est}$ is the expected number of e^+e^- background.

$N_{e^+e^-}^{Est}$ is calculated on a bin by bin basis since A and R calculated using the above formulae vary as a function of invariant mass, as described in Table A.1. The electron candidate is required to satisfy the offline selection as described in Sec. 5.3. The muon candidate which lies in the detector acceptance region $|\eta| < 2.4$, passing tight identification criteria and the particle flow isolation [111] defined within a cone of $\Delta R < 0.3$ is selected. The selection requirement applied on the muon candidate is explained in the Table 5.4. The $e\mu$ events in data and MC are selected using an electron-muon trigger *HLT_Mu8_TrkIsoVVL_Ele17_CaloIdL_TrackIdL_IsoVL*, having a p_T requirement of 17 GeV and 8 GeV, respectively on the HLT electron and muon objects. An opposite charge requirement is applied in order to select the $e\mu$ pair. The electron and muon selected by the electron-muon trigger are required to have $p_T > 25$ GeV and $p_T > 15$ GeV, respectively. The kinematic variables p_T , η and ϕ for the electron and muon candidates are shown in Fig. 5.14.

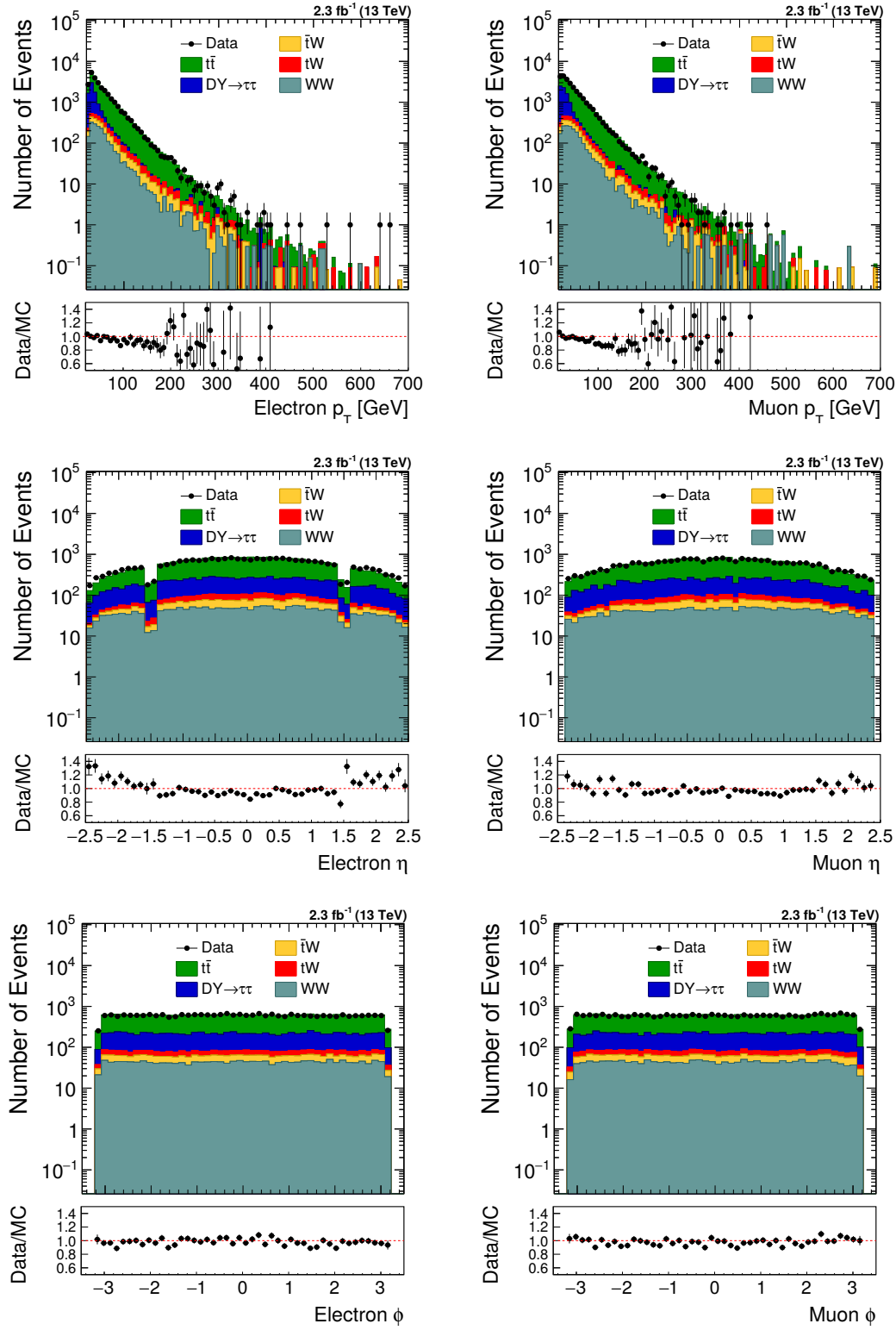


Figure 5.14: Kinematic variables p_T , η and ϕ for electron (left) and muon (right) candidates after pre-selection (kinematic and identification cuts for $e\mu$ selection) in data (black circles) and Monte-Carlo prediction (stacked histograms).

Table 5.4: Summary of Tight Identification and Particle Flow Isolation for the selection of muon [111] in the $e\mu$ method.

Selection	Cut threshold
Muon identification	Each muon should be Global Muon $N_{pixel} > 0$ $N_{muon} > 0$ $N_{matchedstations} > 1$ $N_{trk.layers} > 5$ $ d_{xy}(PV) < 2 \text{ mm}$ $ d_z(PV) < 5 \text{ mm}$
PF Isolation	$\sum_{\Delta R < 0.3} (p_T)/p_T(\mu) < 0.15$
Vertex fit	$\chi^2 < 10$

The $e\mu$ method is validated by performing a Closure test using the MC samples. In this test, the $e\mu$ events are counted directly from MC and e^+e^- events are estimated from the same MC samples using the technique described above. Figure 5.15 (left plot) shows the comparison between the number of e^+e^- events obtained from background MC samples and the number of e^+e^- events estimated from $e\mu$ MC. Since, the factor A is calculated on bin by bin basis, we expect an exact agreement between observed and estimated e^+e^- events obtained from MC. The results of validation test are reported in the Table 5.5.

To estimate the e^+e^- background events from $e\mu$ data, the sample of $e\mu$ events in data and simulation is compared both for the number of events and the shape of invariant mass spectrum. The mass spectra of $e\mu$ events obtained is shown in Fig. 5.15 (right plot) concluding that the simulation describes the data quite well. The number of $e\mu$ events 26629 ± 163 (stat) in data compared to 27605 ± 166 (stat) events in MC accounts to a difference 4% between data and MC.

To calculate the e^+e^- background, the $e\mu$ method is applied to $e\mu$ data events. Figure 5.16 shows the comparison of the number of observed e^+e^- events in MC simulation and the number of estimated e^+e^- events obtained from $e\mu$ data. The

Table 5.5: Total number of $e\mu$ and e^+e^- events observed in data and Monte-Carlo prediction and the estimated number of e^+e^- events from data and Monte-Carlo simulation, where all errors are statistical.

#Events	Obs. $e\mu$	Obs. e^+e^-	Est. e^+e^-
data	26629 ± 163	–	11899 ± 109
mc	27605 ± 166	13066 ± 114	13066

estimation procedure yields 11899 ± 109 (stat) e^+e^- events. The average difference per bin between the estimated e^+e^- background and MC prediction is 10%, which is considered as the systematic error on the $e\mu$ method.

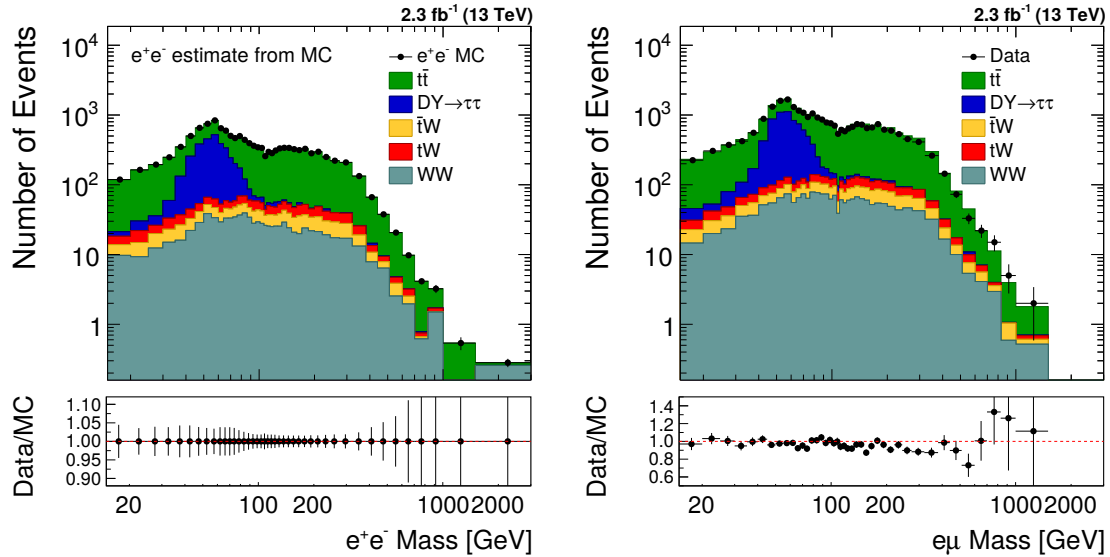


Figure 5.15: Left: The number of observed e^+e^- events from Monte-Carlo prediction (stacked histograms) and the number of estimated e^+e^- events obtained from $e\mu$ MC (black circles). Right: The number of observed $e\mu$ events in data (black circles) and Monte-Carlo prediction (stacked histograms).

5.4.2 Measurement of Dielectron Background using Fake Rate Method

In addition to real dielectron events from electroweak processes, there are QCD multijet and W +jet events which contain at least one misidentified electron. These

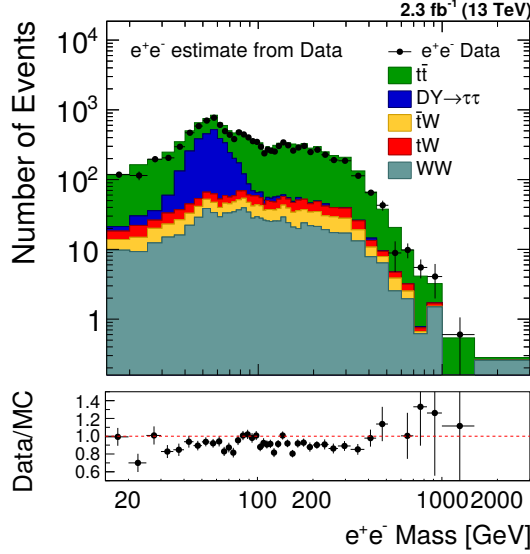


Figure 5.16: The number of observed e^+e^- events from Monte-Carlo prediction (stacked histograms) and the number of estimated e^+e^- events obtained from $e\mu$ data (black circles) using the $e\mu$ method.

backgrounds with fake dielectron events can be estimated using the misidentification rate technique called the fake rate method. In this method, the fake rate is calculated from single photon data sample by measuring the probability for a jet which gets reconstructed as an electron by passing the DY selection, described in Sec. 5.3. The events used to measure the fake rate are selected using single photon trigger $HLT_PhotonX$, where $X = 22, 30, 36, 50, 75, 90, 120, 175$ and corresponds to different E_T thresholds. Here, $X = 175$ is the only unrescaled trigger available in this study. An ‘OR’ combination of these triggers is used in order to correctly calculate the trigger decision and prescale at the HLT level. Figure 5.17 shows the E_T distribution of the HLT photon object obtained from data, before and after applying the trigger prescale. It is observed that the distribution before (red) applying trigger prescale becomes smooth after (black) correctly applying the prescale.

In order to calculate jet to electron faking ratio, in addition to the trigger requirement, a set of cuts are applied on data and MC to ensure that the sample used to measure the fake rate is dominated by jets. The sample obtained is then referred to as jet sample. The cuts applied to select the jet sample are listed below:

- No. of electrons passing DY selection ≤ 1
- Particle Flow MET < 20 GeV
- No. of missing inner hits = 0
- $\Delta R \left(= \sqrt{\Delta\eta^2 + \Delta\phi^2} \right) < 0.5$

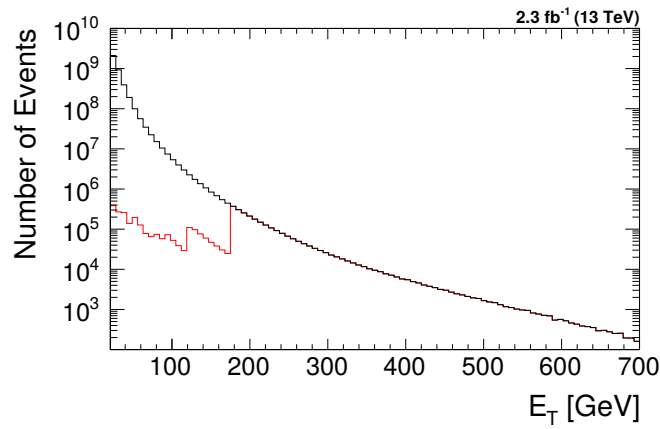


Figure 5.17: E_T distribution of the HLT photon object before (red) and after (black) applying the trigger prescale. The distribution is common after $E_T = 175$ GeV, which is the maximum threshold of single photon trigger.

The condition applied on the number of electrons passing the DY selection, rejects the real dielectron events. A cut on the MET removes the contamination from W +jets events. The missing hits condition and ΔR (between the fake able electron and HLT photon object) cut, ensures that the contamination from photons is removed, which can otherwise lead to photon-to-electron fake rate. The remaining contribution from photons is removed by subtracting the photon events in data from γ +jets MC simulation. Similarly, the contamination from electroweak processes ($\text{DY} \rightarrow ee$, $\text{DY} \rightarrow \tau\tau$, $t\bar{t}$, single-top and dibosons) is removed from data by subtracting same events selected from MC.

The fake rate obtained after electroweak subtraction as a function of electron p_T is shown in Fig. 5.18 and is defined as the fraction of electrons that can be selected from jet sample using the DY selection. In order to account for η dependence, the

fake rate is calculated separately in barrel ($|\eta| < 1.4442$) and endcap ($1.566 < |\eta| < 2.5$) region and agrees within the statistical uncertainty.

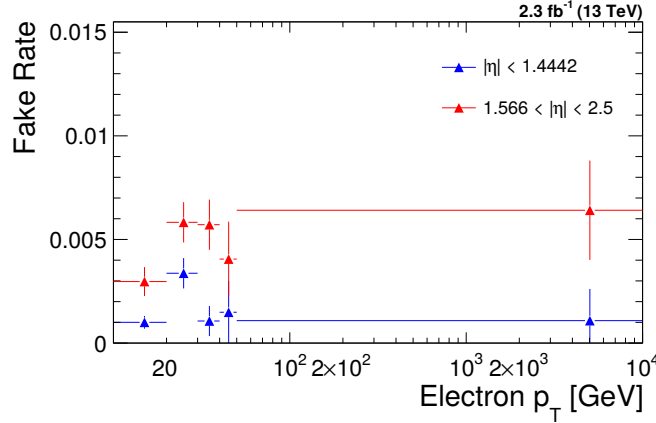


Figure 5.18: Electron fake rate obtained as a function of p_T in barrel and endcap regions, after performing the electroweak subtraction from Monte-Carlo prediction.

In order to estimate QCD and W +jets backgrounds, a sample of events is obtained from the single electron data sample. For QCD, the sample contains two electrons which fail the DY selection, while for W +jets the sample constitutes an electron that fails and another that passes the selection, each multiplied by a factor $\left(\frac{f}{1-f} \times \frac{f'}{1-f'}\right)$ and $\left(\frac{f}{1-f}\right)$, respectively. Here f and f' correspond to the fake rate of two electrons that fail the DY selection and are measured as a function of p_T and η of the respective electron. The contribution from electroweak processes which contaminate the above selection is subtracted from data using MC simulation. Additionally, the contamination from QCD events is also removed while estimating W +jets background. The formula used for the estimation procedure is presented in eq. 5.3-5.4 for QCD and W +jets backgrounds, respectively. Figure 5.19 shows the estimated dielectron mass spectrum obtained from the fake rate method. The estimated number of fake events are assigned 50% systematic error, since the level of fake backgrounds is relatively low and hence this error is not a dominant source of uncertainty. Additionally, a study to compare the number of dielectron events obtained from MC prediction and data-driven estimate is found to match within 50%

for W +jets and is reported in Table 5.6. The QCD MC prediction is not used in this analysis, since the number of events left after applying the dielectron selection is very small and hence the result from simulation is not reliable.

$$(N_{2F}^{data} - N_{2F}^{MC}) \cdot \frac{f}{1-f} \cdot \frac{f'}{1-f'} \quad (5.3)$$

$$(N_{1P+1F}^{data} - N_{1P+1F}^{MC}) \cdot \frac{f}{1-f} - 2 \cdot (N_{2F}^{data} - N_{2F}^{MC}) \cdot \frac{f}{1-f} \cdot \frac{f'}{1-f'} \quad (5.4)$$

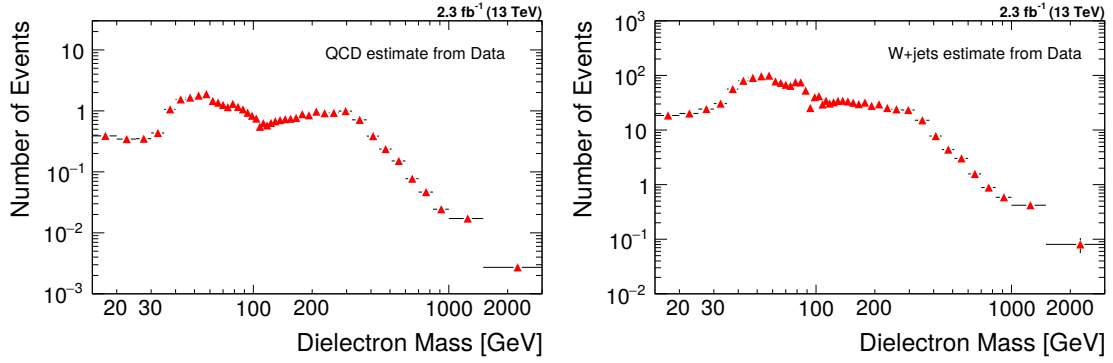


Figure 5.19: The number of dielectron events for QCD (left) and W +jets (right) backgrounds estimated from data using the fake rate method.

Table 5.6: Total number of dielectron events observed in Monte-Carlo prediction and the estimated number of dielectron events from data.

Dielectron events	QCD	W +jets
data	33	1532
mc	—	1500

While, all the backgrounds are estimated using data-driven techniques discussed above, WZ and ZZ diboson backgrounds are estimated from MC prediction since their contribution to the DY mass spectrum is not large. In order to take into account the difference between data and MC, a correction factor, which will

be discussed later, is applied to the WZ and ZZ mass distributions before their contribution is subtracted from data.

The $\gamma\gamma$ -initiated production of same-flavour lepton pairs is estimated with FEWZ 3.1 program [112], using LUXqed photon PDF set [113]. The effects are negligibly small for most of the mass range except for high mass region [114], which is smaller in comparison to the size of uncertainties from other sources in that region. Hence, the PI contribution is not considered in this analysis.

The expected dielectron yields in the bins of invariant mass obtained after performing background estimation from data-driven methods is shown in Fig. 5.20. The contribution of each background process to the DY mass spectrum is obtained in Fig. 5.21. From this plot, it can be seen that the major contribution comes from $DY \rightarrow \tau\tau$ in the low mass region while in the high mass region, the backgrounds $t\bar{t}$, tW , $\bar{t}W$ and WW are dominant.

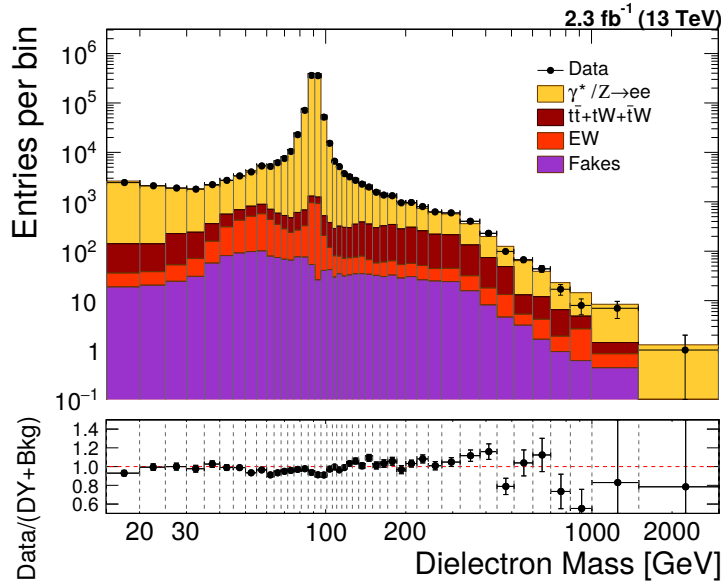


Figure 5.20: The observed dielectron invariant mass spectra for data (black circles) and Monte-Carlo (stacked histograms) events and the corresponding ratio of observed to expected yields. EW means the contribution from WW, WZ, ZZ and $DY \rightarrow \tau\tau$, Fakes correspond to the contribution from QCD and W +jets.

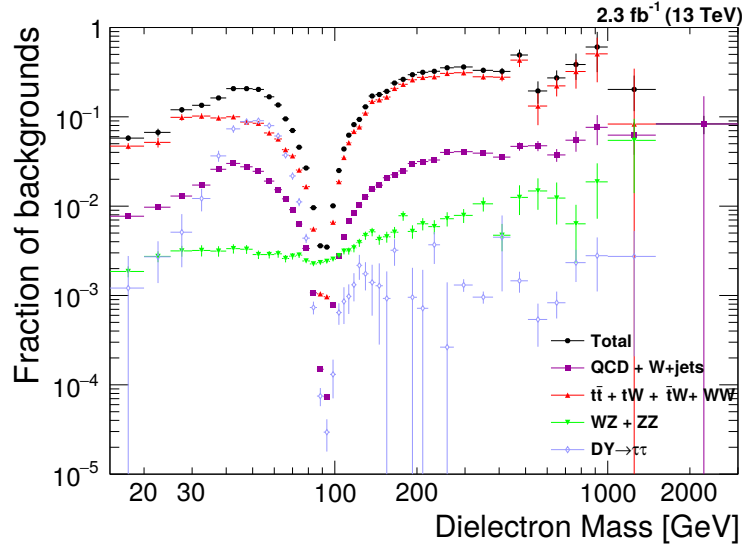


Figure 5.21: The fraction of the number of dielectron events from each background process with respect to the total observed number of data events. ‘Total’ corresponds to the combined fraction for all the backgrounds estimated from data-driven techniques and Monte-Carlo simulation.

5.5 Corrections

The reconstructed dielectron mass distribution obtained by background subtraction, does not take into account the loss of events due to detector resolution, detector acceptance, reconstruction and selection inefficiencies and the FSR, a process not included in the MC calculations. In the following text, we refer post-FSR and pre-FSR to anything defined before and after the FSR effects. As a result of these limitations, the measured yield cannot be directly compared with the SM theoretical expectations. The measurement of differential cross section therefore, requires a four-step correction procedure. The measured distribution is first corrected for the detector resolution effects by an unfolding technique. The unfolded distribution is then corrected for detector acceptance (A) and efficiency (ϵ). After these corrections, the mass spectra is corrected by a scale factor (ρ), to account for the difference in efficiency between data and simulation. As a last step, the pre-FSR dielectron mass distribution is obtained by correcting for the radiation effects which can then be compared to various theoretical predictions.

5.5.1 Unfolding

The experimental results are often distorted due to limited detector resolution which can bias the cross section measurement. In order to correct the migration effects, an unfolding procedure [115] is implemented which uses the invariant mass distribution from simulation. This technique maps the true dielectron distribution obtained at the generator-level, to the measured one, while considering the migration of events among the analysis bins.

The migration effects are parameterized by using a response matrix which is determined from electrons passing the kinematic cuts and detector acceptance. For 1-dimensional measurement, the response matrix element T_{ik} represents the fraction of events from bin k of true distribution (N_k^{true}) that ends up reconstructed in bin i of observed distribution (N_i^{obs}) in the limit of no background. These are related to each other as shown in eq. 5.5. The true invariant mass spectrum is then obtained by the inversion of response matrix using eq. 5.6.

$$N_i^{\text{obs}} = \sum T_{ik} N_k^{\text{true}} \quad (5.5)$$

$$N_k^{\text{true}} = \sum (T_{ik})^{-1} N_i^{\text{obs}} \quad (5.6)$$

The true mass is defined as the generator-level dielectron invariant mass and is obtained from the post-FSR electrons. The observed mass is calculated by electrons which pass the full DY selection at the reconstruction-level. The correction procedure is implemented by using a RooUnfold software package. This package provides several algorithms among which iterative D'Agostini method [116] has been used to unfold the experimental results in this analysis. This method can be used until convergence. The number of iterations is obtained by unfolding the observed mass distribution using (i)th and (i+1)th iterations, separately. The relative difference

of the number of events in each mass bin is calculated between the two unfolded distributions, as specified in eq. 5.7. The iteration ‘i’ for which this difference is smaller than 0.1% determines the number of iterations used for unfolding.

$$\frac{|n^i - n^{(i+1)}|}{n^i} < 0.1\% \quad (5.7)$$

Here, n^i is the number of events in a mass bin after unfolding with ‘i’ iteration. Using this technique we obtain $i = 21$.

Figure 5.22 shows the correlation plot between the generator-level and reconstruction-level dielectron mass which is used to unfold the background subtracted yield. The horizontal band extending towards left can be traced to the events which experience radiation effects in the Z -peak region due to which the generated mass has a lesser value compared to reconstructed mass. The electron reconstruction algorithm picks up radiated photons as a result of which the reconstructed dielectron mass becomes close to the pre-FSR mass and can be different from the post-FSR generator-level dielectron mass.

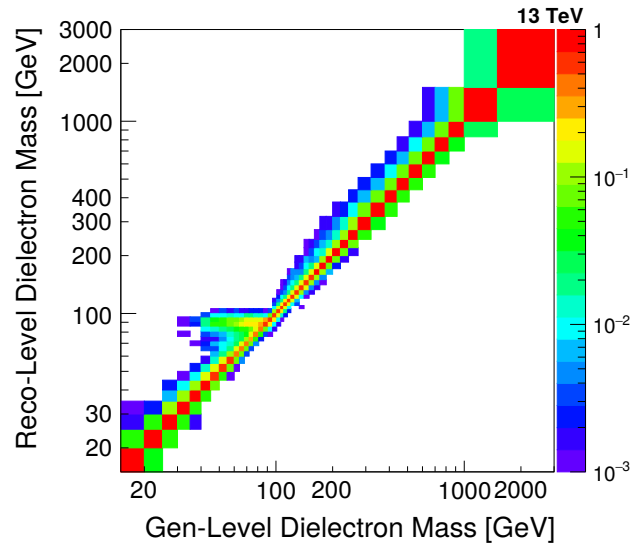


Figure 5.22: The response matrix computed within the detector acceptance from aMC@NLO simulation to unfold the background subtracted yield.

The validity of the unfolding method is first tested on signal MC sample. A closure test is performed in which reconstruction-level mass distribution from the simulation is unfolded using the technique discussed above. Figure 5.23 shows that the resulting unfolded yield from simulation is in perfect agreement with the generator-level mass distribution which validates the D’Agostini’s iteration procedure used in this analysis.

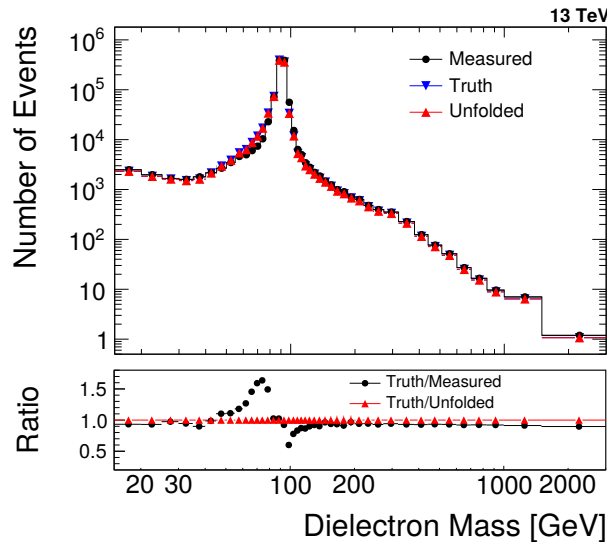


Figure 5.23: Closure test: The comparison of measured (reconstruction-level) distribution and unfolded yield from Monte-Carlo simulation to the true (generator-level) distribution in bins of dielectron invariant mass using D’Agostini’s iteration method with 21 iterations.

After validating the unfolding procedure, the background subtracted yield i.e ($N_{obs} - N_{bkg}$) is corrected for the detector effects using the above obtained response matrix. The largest effect of unfolding $\sim 50\%$ can be seen in the Z -peak region with minor effect at high invariant masses.

5.5.2 Acceptance and Efficiency

Due to the detector geometry, some of the particles produced in proton-proton collisions, might remain undetected. Additionally, there might be few particles which lie within the detector acceptance but do not pass the efficiency selection. In

order to compensate for the loss of such particles, the unfolded yield is corrected for acceptance and efficiency selection.

The detector acceptance is defined as the fraction of simulated signal events when both electrons pass the kinematic: $p_T > 30$ (10) GeV for leading (sub-leading) electrons and geometric: $|\eta_{sc}| < 2.5$ (excluding the ECAL gap region) requirements. It is calculated with respect to full phase space. The efficiency is defined as the fraction of events in the DY MC sample that lie inside the detector acceptance passing the full event selection of this analysis. Figure 5.24 shows A , ϵ and $A \times \epsilon$ as a function of dielectron invariant mass. The following equation provides the definition of acceptance and event efficiency discussed above:

$$A \times \epsilon = \frac{N^A}{N^{\text{gen}}} \cdot \frac{N^\epsilon}{N^A} \quad (5.8)$$

where,

- N^{gen} is the total number of generated signal events in a given invariant mass bin
- N^A is the number of events inside the geometrical and kinematic acceptance region
- N^ϵ is the number of events passing the analysis selection

5.5.3 Selection Efficiency

There is a probability that a poorly reconstructed electron gets misidentified at the selection stage. In order to correct for this effect, reconstruction, identification and trigger selection efficiencies have been computed using a data-driven approach called the tag and probe method [117]. This technique selects those events in which a good electron (tag) passing tight selection criteria and a loosely identified electron (probe)

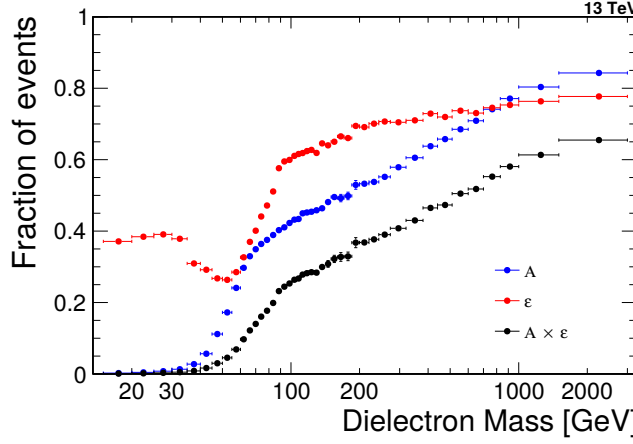


Figure 5.24: Detector acceptance, event efficiency and their product as a function of post-FSR dielectron invariant mass.

are reconstructed with an invariant mass compatible with a well measured Z mass resonance. The efficiency is measured as a function of p_T and η , by counting the number of probe as follows:

$$\epsilon(p_T, \eta) = \frac{N_{Pass}^{Probes}}{N_{Pass}^{Probes} + N_{Fail}^{Probes}} \quad (5.9)$$

where, N_{Pass}^{Probes} is the number of probes passing the selection requirement and $N_{Pass}^{Probes} + N_{Fail}^{Probes}$ is the total number of probes. For this analysis, the tag and probe pairs with $60 < M_Z < 120$ GeV mass window are selected to measure the electron efficiency factors in data and simulation. If there exist more than one pair, the one with mass closer to the Z mass is selected.

In order to determine the number of passing and failing probes, counting or fitting methods can be used. Counting method is applicable when the background is small, but since the efficiencies here are being computed using a loose Z mass window, there is a possibility of background contamination under the Z -peak. Hence, proper handling of background becomes necessary. Therefore, in order to take into account the effect of background, fitting method has been used to estimate the ef-

ficiency. The details of the functions used to fit the signal and background can be found in [118].

In a Z -peak event, a well reconstructed electron candidate, the tag, passes the trigger and identification requirements while the other candidate, the probe, is required to pass a specific condition, for which the efficiency is being measured in each step. The efficiency is then calculated as the fraction of probe electrons which pass the required selection criteria to the total number of probe electrons as described in eq. 5.9. The efficiencies determined from data and MC are divided to compute the scale factors: $\rho = \epsilon_{data}/\epsilon_{MC}$ which are used to account for the difference in efficiency between data and MC.

5.5.3.1 Reconstruction Efficiency

For measuring the reconstruction efficiency, the probe is defined as a supercluster. The invariant mass of the pair is calculated by constructing the four-momentum of the supercluster by assigning it the mass of an electron. The pass condition is the existence of matched electron in the electron collection without any further requirement on that electron. The efficiency and scale factors as a function of electron p_T and supercluster η_{sc} can be seen in Fig. 5.25.

5.5.3.2 Identification and Isolation Efficiency

The probe is defined as an electron which is present in the default collection of reconstructed electrons after passing the reconstruction algorithm, with no further selection applied. The pass sample contains only those electrons which survive the full identification and isolation requirements. Table 5.7 summarizes the selection applied on the tag and probe electron candidates. The identification and isolation efficiency and the corresponding scale factors obtained from the tag and probe method are shown in Fig. 5.26.

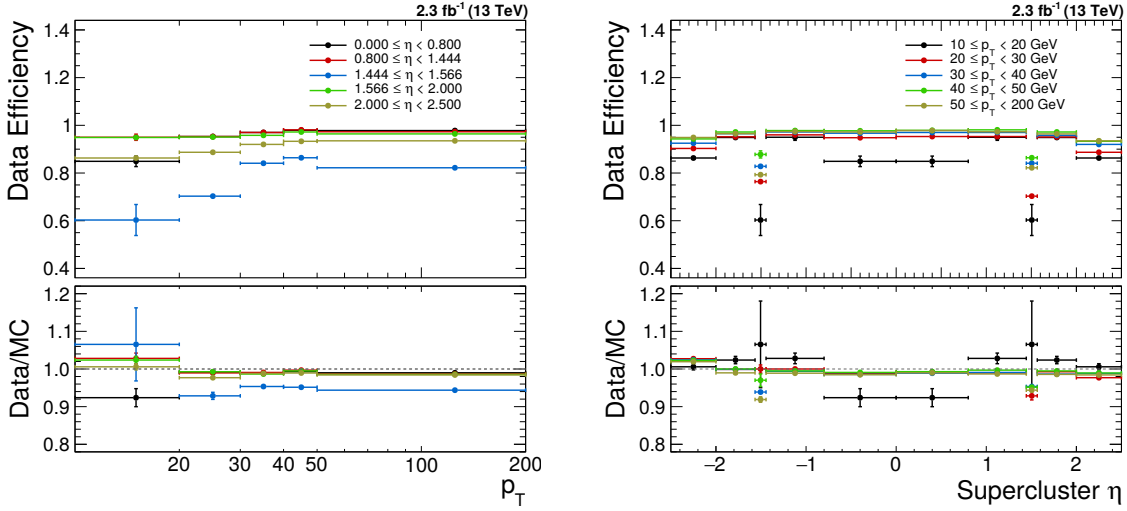


Figure 5.25: Reconstruction Efficiency in data and the corresponding scale factors obtained after dividing the efficiencies for data and Monte-Carlo simulation as a function of p_T (left) and supercluster η_{sc} (right).

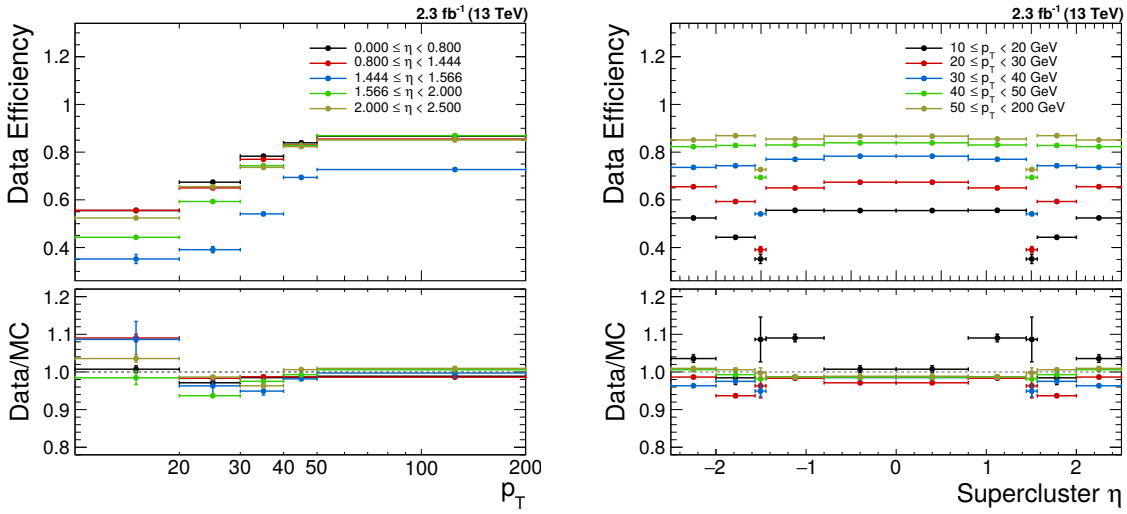


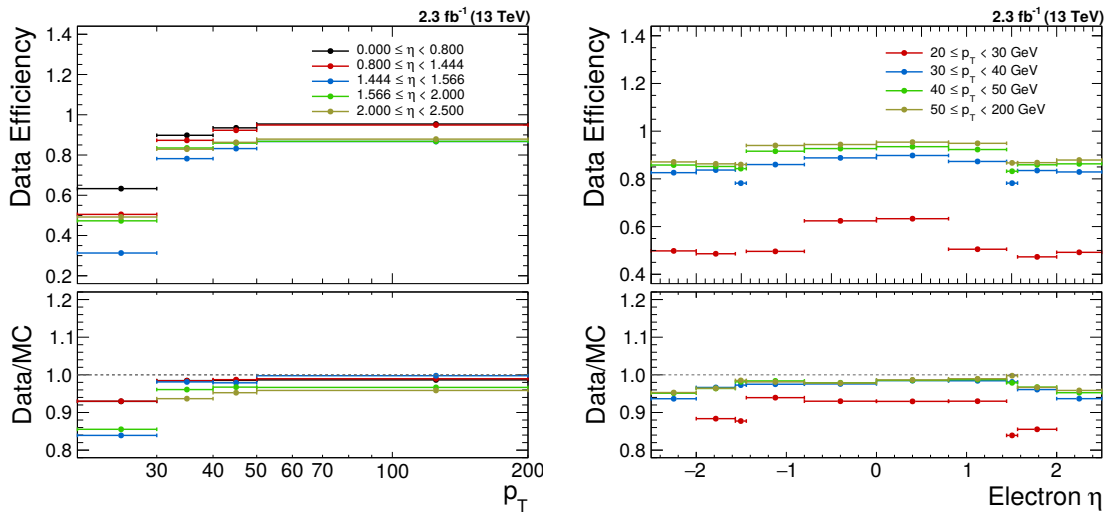
Figure 5.26: Electron Identification and Isolation Efficiency in data and the corresponding scale factors obtained after dividing the efficiencies for data and Monte-Carlo simulation as a function of p_T (left) and supercluster η_{sc} (right).

5.5.3.3 Trigger Efficiency

In order to determine HLT efficiency, the probe candidate is required to pass the full electron selection except the condition on ΔR matching between online and offline electron candidates. The probe which then matches the HLT trigger object, is considered to be the passing probe. Figure 5.27 shows the trigger efficiency and

Table 5.7: Tag and Probe selection criteria for measuring the Identification and Isolation efficiency.

Selection	Tag	Probe
p_T	> 30 GeV	> 10 GeV
$ \eta_{sc} $	< 2.5	< 2.5
Identification	Tight	Medium
Trigger	$HLT_Ele23_WPLoose_Gsf$	No trigger applied

Figure 5.27: HLT Efficiency for the trigger $HLT_Ele23_WPLoose_Gsf$ in data and the corresponding scale factors obtained after dividing the efficiencies for data and Monte-Carlo simulation as a function of p_T (left) and electron η (right).

data/MC scale factors as a function of electron p_T and η .

The total event selection efficiency is factorized into individual efficiencies for each electron in an event which passes a particular selection criteria,

$$\epsilon_{event} = \epsilon_{e_1} \cdot \epsilon_{e_2} \cdot \epsilon_{event,trig} \quad (5.10)$$

where, ϵ_e is the single electron efficiency defined as,

$$\epsilon_e = \epsilon_{reco} \cdot \epsilon_{id+iso} \quad (5.11)$$

and $\epsilon_{event,trig}$ corresponds to the trigger efficiency of the event defined as following,

$$\epsilon_{trig} = 1 - ((1 - \epsilon_{1,trig}) \cdot (1 - \epsilon_{2,trig})) \quad (5.12)$$

5.5.4 Final State Radiation Effects

Electrons can radiate photons in a process known as final state electromagnetic radiation (FSR). FSR effect can change the observed invariant mass which is computed from the four-momenta of two electrons. If final state photons having sizable energy are emitted, the observed mass can be substantially lower compared to the propagator mass in the hard interaction. This effect is most dominant just below the Z -peak region, since the radiative events get shifted lower in mass and become significant.

The correction for FSR effects is performed by following the unfolding technique as described in Sec. 5.5.1. However, unlikely for detector resolution effect, the unfolding procedure is applied in full phase space using the response matrix derived from pre-FSR and post-FSR yields in signal simulation. In order to obtain the pre-FSR invariant mass without any generator dependent information, a correction procedure known as dressed lepton is considered, which uses only the post-FSR electrons. In this procedure, the dressed electron four-momentum is recalculated taking into account the hard photon radiation candidates as described below,

$$p_e^{dressed} = p_e^{post-FSR} + \sum p_\gamma^{FSR} \quad (5.13)$$

where, the photon candidates must lie inside a cone of radius $\Delta R < 0.1$ constructed around the post-FSR electron candidate. No additional acceptance cuts or requirement on generator information inside the cone is needed.

Unfolding for FSR uses the D'Agostini's iteration method with 21 iteration number as obtained from eq. 5.7. The response matrix and closure test for the

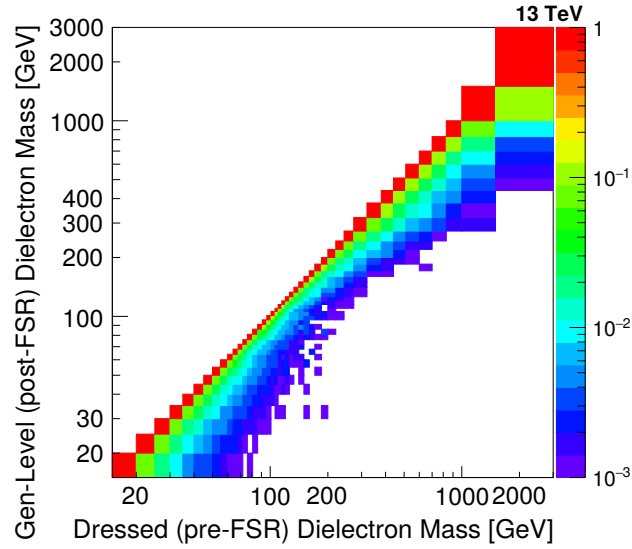


Figure 5.28: The response matrix computed in full phase space from aMC@NLO simulation to correct for the Final State Radiation (FSR) effects using the iterative D’Agostini unfolding method.

unfolding method are shown in Fig. 5.28 and 5.29, respectively. Closure test confirms the validity of the above procedure applied to correct for the radiation effects, showing a perfect agreement between the post-FSR and pre-FSR (dressed) distribution. The level of correction from the post-FSR to dressed definition is found to be between $\sim 30\text{-}50\%$ and is dominant below the Z -peak region.

5.6 Systematic Uncertainties

Systematic uncertainties have been obtained for each step in the determination of dielectron invariant mass spectrum. The various sources of uncertainties are discussed in this section.

5.6.1 Luminosity Uncertainty

The luminosity delivered to the CMS detector by the LHC in proton-proton collisions is measured by using the silicon pixel cluster counting method [119]. The uncertainty

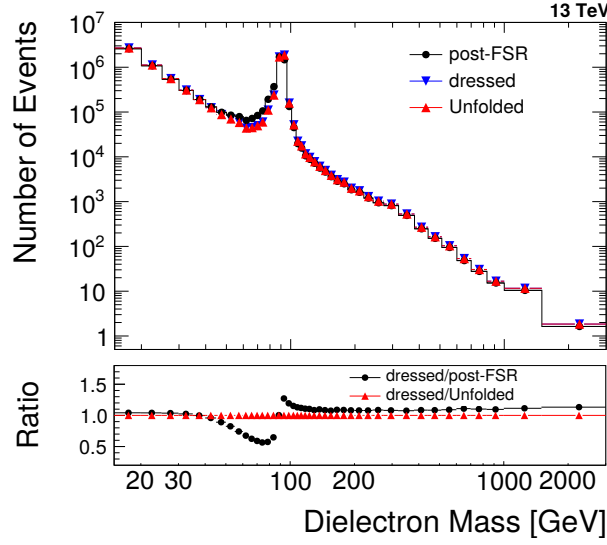


Figure 5.29: Closure test: The comparison of generator-level (post-FSR) invariant mass distribution and FSR corrected unfolded yield from Monte-Carlo simulation to the dressed mass (pre-FSR) distribution in bins of dielectron invariant mass using D’Agostini’s iteration method with 21 iterations.

on the luminosity measurement is estimated to be 2.3% for the whole data-taking period in 2015. The luminosity uncertainty propagates directly to the cross section measurement. Hence, a total systematic uncertainty of 2.3% is considered across all the invariant mass bins.

5.6.2 Statistical Uncertainty

The statistical uncertainty is estimated by randomizing the observed yield distribution (N_{obs}). In order to randomize N_{obs} within its statistical uncertainty, 1000 yield distributions are produced by randomly varying the number of events in each mass bin following the Poisson law and calculating the differential cross section corresponding to each randomized yield. Relative difference with the central cross section is calculated and a Gaussian fitting is performed for each mass bin. The sigma of the fitted distribution is assigned as the statistical uncertainty corresponding to a mass bin.

This method takes into account the correlation between bins, which mostly comes from the unfolding procedure used for correcting detector resolution and FSR effects. Statistical uncertainty for the differential cross section varies depending upon the phase space in which the measurement is performed, since the correlation between the mass bins becomes different in each case.

5.6.3 Scale Correction

The systematic uncertainty from these corrections is determined by scaling the energy and momentum of the electron 100 times within its uncertainty. This uses three different values of sigma, which further has two independent components: rho (ρ) and phi (ϕ). Variation in energy and momentum is calculated for $\sigma \pm \rho$ and $\sigma - \phi$ [120] to obtain the measured dielectron distributions. Each distribution is used to recalculate the response matrix for correcting the detector effects and finally, multiple cross sections are obtained corresponding to each unfolded yield. The maximum standard deviation from the Gaussian fitting applied on the relative difference distribution with the central cross section, is assigned as systematic uncertainty in each mass bin.

5.6.4 Background Estimation

The uncertainty for the background estimation is mainly driven by the statistical uncertainty of each background source which is treated as systematic uncertainty. For the backgrounds that are estimated from MC and data-driven methods, the additional source of uncertainty considered is (1) the uncertainty of cross section and (2) the difference between estimation from data and simulation, respectively. For the fake electron backgrounds, QCD and W +jets, which are estimated using the fake rate method, the statistical uncertainty on the fake rate is propagated by varying the fake rate within its uncertainty and performing the estimation procedure. The difference obtained with respect to the nominal estimation result is assigned as

the systematic uncertainty on each fake background.

After the uncertainty on the background events is calculated, the uncertainty on the differential cross section is estimated. For each background process, 1000 background distributions are obtained by randomizing it within the uncertainty on events in each mass bin. When the uncertainty from statistical component is measured, each mass bin is randomized independently, while for the uncertainty from systematic components, denoted as (1) and (2), the mass bins are randomized using same random number for each process. Based on each randomized background distribution, 1000 cross sections are calculated and the variance of randomized cross section with respect to the central value is assigned as the uncertainty from corresponding background process. Finally, the total uncertainty from background estimation is obtained as the quadrature sum of uncertainty from each background process.

5.6.5 Detector Resolution

The uncertainty associated with the unfolding procedure comes mainly from the uncertainty in the response matrix elements due to imperfection in the simulation of detector resolution. Instead of calculating the systematic uncertainty specifically on detector resolution unfolding, the cumulative result of resolution effects on all the analysis steps is measured. In this analysis, two kinds of sources are considered (1) Statistical uncertainty on the response matrix due to the finite size of MC sample and (2) Systematic uncertainty on the response matrix from deficiencies in the model. Uncertainty from the first source is estimated by using the diagonal term of a matrix namely covariance matrix, produced by randomizing the response matrix within the statistical uncertainty of the signal MC sample. Second source of uncertainty is estimated by calculating the unfolding correction using a reweight technique. In this method, the generator-level MC mass spectrum is scaled by the ratio of FEWZ and aMC@NLO DY signal mass distributions, to obtain an alternate

generator-level distribution and a corresponding weighted response matrix. The weighted matrix is then used to unfold the background subtracted data distribution. Finally, the difference between unfolded yield obtained using the D’Agostini’s unfolding technique applied to the weighted response matrix and the nominal yield is assigned as systematic uncertainty associated with the response matrix.

5.6.6 Acceptance Correction

The uncertainty from the acceptance correction contributes to the theoretical uncertainty and is estimated from three kinds of sources:

- *The uncertainty from imperfect knowledge of the non-perturbative PDFs* participating in the hard scattering is estimated by FEWZ calculation with NNLO using a reweight technique with LHAGLUE interface to the PDF library LHAPDF as described in [121–123]. The estimation also includes NLO EW corrections [2].
- *The factorization and renormalization scales* for which theoretical cross section is first calculated using the reference value of the coupling constant 0.118 and then with 0.117 and 0.119. The difference of the cross section with respect to the reference value is assigned as the theoretical uncertainty. Effect of the scale variation is about 1-2% level on the cross section.
- *The difference between aMC@NLO and NNLO* which is taken into account by assigning the difference in acceptance between aMC@NLO and NNLO prediction (calculated by FEWZ).

5.6.7 Efficiency Correction

The uncertainty from efficiency scale factor correction is an important source of uncertainty in this analysis. As discussed in Sec. 5.5.3, three different types of single

electron efficiencies are measured with the data-driven method and are combined into event efficiency scale factors. This procedure determines the efficiency and a corresponding statistical uncertainty. However, a variety of possible systematic biases from the tag and probe method which can effect the electron efficiencies, such as dependence on the shape of signal and background considered in the fit model, variation in tag selection, and others are studied. Afterwards, an appropriate systematic uncertainty to the single electron efficiency scale factors is assigned. Finally, the total systematic uncertainty on the cross section is evaluated by combining the statistical and systematic uncertainties obtained from the event scale factors. The different sources of efficiency correction systematic uncertainty are discussed below.

- *Uncertainty in line shape modeling:* This uncertainty is estimated by performing the signal and background fitting using alternate fit functions. A comparison is made between the efficiencies extracted with two signal hypotheses [118]: (1) Monte-Carlo templates smeared with Gaussian and (2) Crystal Ball fit function. For the background [118], (1) CMSShape and (2) Exponential fit functions are compared.
- *Uncertainty from Monte-Carlo simulation:* This uncertainty is estimated by comparing the efficiencies calculated from two different signal samples. We use (1) NLO and (2) LO MC samples to determine different efficiencies of each type in order to evaluate the systematic uncertainty. The effect of this uncertainty is minimal and covered by the larger statistical uncertainty.
- *Uncertainty from other sources in tag and probe method:* In the efficiency measurement using tag and probe method, a selection criteria for the kinematic and identification requirements is applied on the tag. To estimate the systematic uncertainty from the variation in selection parameters, the efficiencies are recalculated after changing the value of each parameter. Difference of the efficiency value for each $p_T - \eta$ bin with the central value is assigned as the

systematic uncertainty. The contribution to the total uncertainty from this source is found to be small.

The above uncertainties are evaluated by computing the cross section multiple times using a collection of single electron efficiency maps such that the entries are modified randomly within $\pm 1\sigma$ of uncertainties in $p_T - \eta$ bins. When the uncertainty from statistical efficiency is considered, each $p_T - \eta$ bin is randomized independently. However, when the uncertainty from systematic uncertainty of tag and probe efficiency is estimated, all $p_T - \eta$ bins are randomized in the same direction and magnitude for each efficiency map in order to move them coherently. We consider 500 efficiency correction maps obtained with the map variation technique to calculate the efficiency corrections, which are applied as weights per electron, to determine multiple final differential cross sections. The sigma of the spread of these cross sections is obtained by Gaussian fitting per mass bin which is used as an estimate of systematic uncertainty in each mass bin.

5.6.8 FSR Correction

Uncertainty from the unfolding procedure for FSR correction is considered from two sources: (1) Statistical uncertainty on the response matrix due to the finite size of MC sample and (2) Uncertainty from model dependence of FSR correction. The uncertainty from first source is estimated by following the same procedure as described for detector resolution. The second source of uncertainty is obtained by comparison with different FSR simulation using PHOTOS [124] generator and assigning the variation of the FSR corrected result as the systematic uncertainty.

5.6.9 Total Uncertainty

After the estimation of uncertainties from all possible sources is performed, the systematic uncertainties from the background estimation, detector resolution and

FSR correction are smoothed to reduce bin by bin fluctuations. The total systematic uncertainty is obtained by taking the quadrature sum of individual uncertainties described in Sec. 5.6.3-5.6.8, except the uncertainty from acceptance correction. The systematic uncertainties from scale corrections and detector resolution are combined since both of these effect the unfolded yield distribution. The effect of uncertainties on the differential cross section measurement as a function of dielectron invariant mass is shown in Fig. 5.30 and the exact values of different systematic uncertainties are summarized in Table A.2.

The systematic uncertainties are the dominant source of uncertainty for the invariant mass region $m < 400$ GeV. The efficiency scale factor is the most significant source of systematic uncertainty below and in the Z -peak region, varying between 8.92-11.43% and 5.11-8.66%, respectively. However, in the high mass region above $m > 200$ GeV, the systematic uncertainty from the background estimation goes up to 100%, driving the total systematic uncertainty.

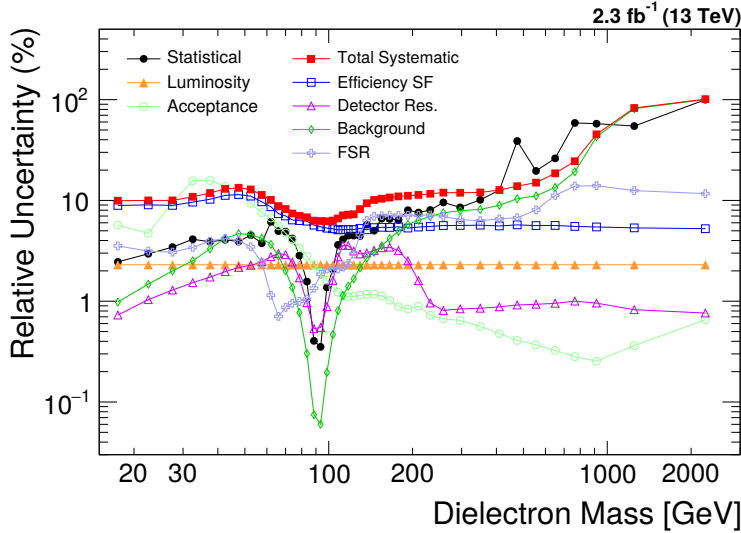


Figure 5.30: The statistical, luminosity, acceptance and the total systematic uncertainties obtained in the bins of dielectron invariant mass.

5.7 Results

The DY cross section measurement is performed after correcting for various effects discussed in the previous sections. The cross section is measured in the Z -peak region $60 < m < 120$ GeV as well as in the bins of dilepton invariant mass, within the range $15 < m < 3000$ GeV.

The DY differential cross section has already been measured in the dimuon final state [7] using the collision data collected by the CMS experiment at a center-of-mass energy $\sqrt{s} = 13$ TeV, corresponding to an integrated luminosity of 2.8 fb^{-1} . The differential cross section measurement obtained in the dielectron and dimuon channels are combined for a greater precision, using the technique known as Best Linear Unbiased Estimate (BLUE) method [125]. The combined estimate of the measured quantities obtained using the BLUE method takes into account all the correlations by considering covariance matrix of the input data. These correlations may arise due to the use of data from the same experiment or even the same theoretical models. The measurement results are discussed in the following sections.

5.7.1 Z -peak Cross Section Measurement

The Z boson production cross section in the peak region $60 < m < 120$ GeV is calculated as following:

$$\sigma_Z = \frac{1}{\mathcal{L}} \left\{ \frac{N_u^{\text{norm}}}{A^{\text{norm}} \cdot \epsilon^{\text{norm}} \cdot \rho^{\text{norm}}} \right\} \quad (5.14)$$

where, N_u^{norm} is the number of events obtained after performing background subtraction and applying unfolding method for the detector resolution and FSR corrections, A^{norm} and ϵ^{norm} are the acceptance and efficiency correction factors in the Z -peak region, ρ^{norm} is efficiency scale factor and \mathcal{L} is the total integrated luminosity.

The absolute cross section measurement in the dielectron final state for full

phase space and fiducial region (within detector acceptance) is summarized in Table 5.8. The combined cross section in the dielectron and dimuon channels is also obtained for the full phase space. The experimental cross sections are found to be in good agreement with NNLO prediction (a typical NNLO prediction is 1870^{+50}_{-40} pb) for the full phase space region.

Table 5.8: Absolute cross section measurements in full phase space and fiducial region (within the detector acceptance) for the Z -peak region $60 < m < 120$ GeV along with the associated uncertainties.

Electron Channel	Cross section in Z -peak region
Full Phase Space	$1949 \pm 2(\text{stat.}) \pm 96(\text{exp. syst.}) \pm 47(\text{th. syst.}) \pm 45(\text{lum.})$ pb
Fiducial	$760 \pm 1(\text{stat.}) \pm 38(\text{exp. syst.}) \pm 17(\text{lum.})$ pb
Combined Channel	Cross section in Z -peak region
Full Phase Space	$1908 \pm 1(\text{stat.}) \pm 25(\text{exp. syst.}) \pm 37(\text{th. syst.}) \pm 44(\text{lum.})$ pb

5.7.2 Differential Cross Section Measurement

The cross section measurement in the bins of dilepton invariant mass is an important measurement performed in this analysis and is defined as,

$$\sigma^i = \frac{N_u^i}{A^i \cdot \epsilon^i \cdot \rho^i \cdot \mathcal{L}} \quad (5.15)$$

where, each quantity is calculated in a given invariant mass bin i . The result in each bin is divided by the corresponding bin width, Δm^i which defines the shape $\sigma^i / \Delta m^i$. The following section describes the results on the differential cross section obtained in the dielectron and combined channels.

5.7.2.1 Dielectron Channel

The DY differential cross section is measured in full phase space in the dielectron decay channel after applying a set of corrections discussed in the Sec. 5.6 and presented

in Fig. 5.31. The results are compared to the NNLO theoretical prediction which is calculated using FEWZ 3.1 including the NLO EW correction and the NLO MADGRAPH5_AMC@NLO. These predictions are calculated using NNPDF3.0 PDF set. The ratio between experimental data and theory can be seen in the middle and bottom plots in which the colored bands represent theoretical uncertainty while the shaded bands represent the total uncertainty, obtained as the combination of statistical, systematic and luminosity uncertainties added in quadrature. Detailed numbers for the central value of the cross section and the associated uncertainties are available in Table A.3. The results are found to be in good agreement with both theoretical predictions within the uncertainties.

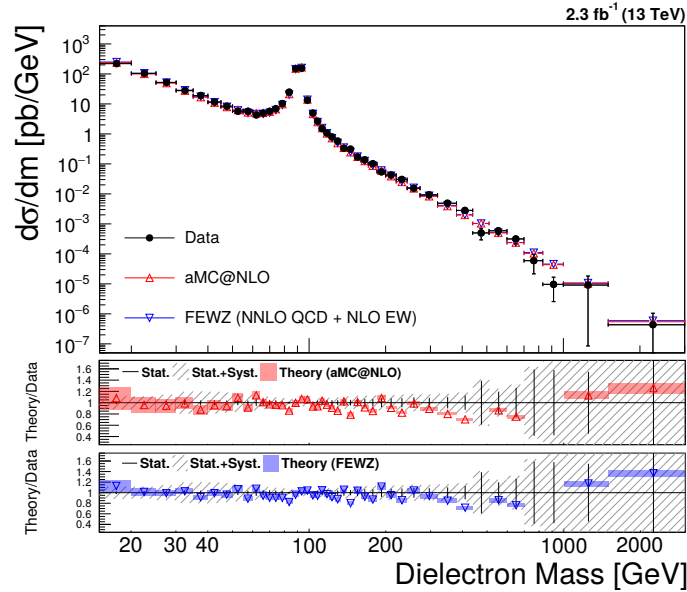


Figure 5.31: The Drell-Yan differential cross section measurement corrected for radiation effects in full phase space as a function of dielectron invariant mass compared to the NNLO theoretical prediction from FEWZ (blue) and the NLO prediction from MADGRAPH5_AMC@NLO (red). The coloured band in the middle and bottom plots denotes theoretical uncertainty and the shaded band denotes total uncertainty which is the combination of statistical, systematic and luminosity uncertainties.

The differential cross section in the fiducial region, defined by the p_T and η requirements on the electrons after the radiation effects have taken place, is also calculated in addition to the fully corrected DY cross section measurement. The fiducial

cross section measurement is performed within the detector acceptance which minimizes the effect of acceptance as well as the FSR correction. The fiducial results are presented in Fig. 5.32 which shows the comparison of experimental data with the NLO theoretical prediction from MADGRAPH5_AMC@NLO. The results are found to be in good agreement with the prediction. Detailed numbers for the central value of the fiducial cross section and the associated uncertainties are shown in Table A.4.

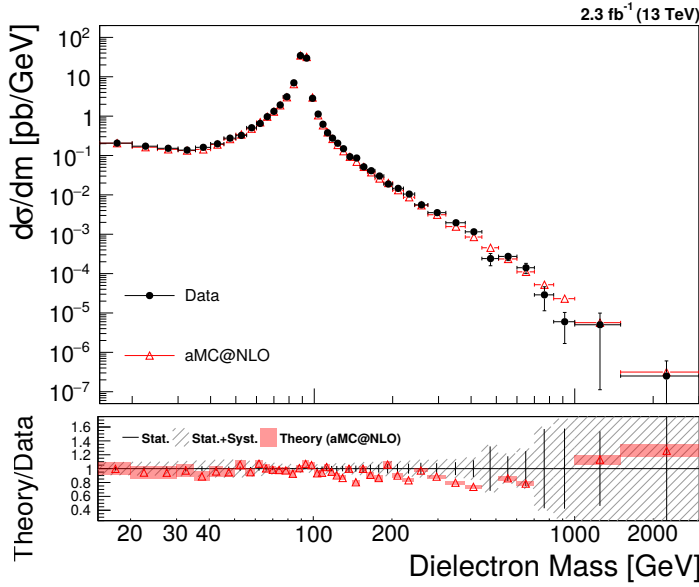


Figure 5.32: The Drell-Yan differential cross section measurement performed in the fiducial region without FSR correction as a function of dielectron invariant mass compared to the NLO theoretical prediction from MADGRAPH5_AMC@NLO. The red band in the bottom plot denotes theoretical uncertainty and the shaded band denotes total uncertainty which is the combination of statistical, systematic and luminosity uncertainties.

The experimental result is compared to the NNLO theoretical prediction calculated from FEWZ in which the data x-coordinate is computed as explained in [126], and is shown in the Fig. 5.33. The ratio between data and NNLO prediction in the mass range $m < 200$ GeV and $200 < m < 3000$ GeV is presented in the left and right plots, respectively in the Fig. 5.34. The blue band, in these plots represent the theoretical uncertainty. The right plot additionally includes the contribution from PI background which is estimated by FEWZ 3.1 with LUXqed PDF set [113].

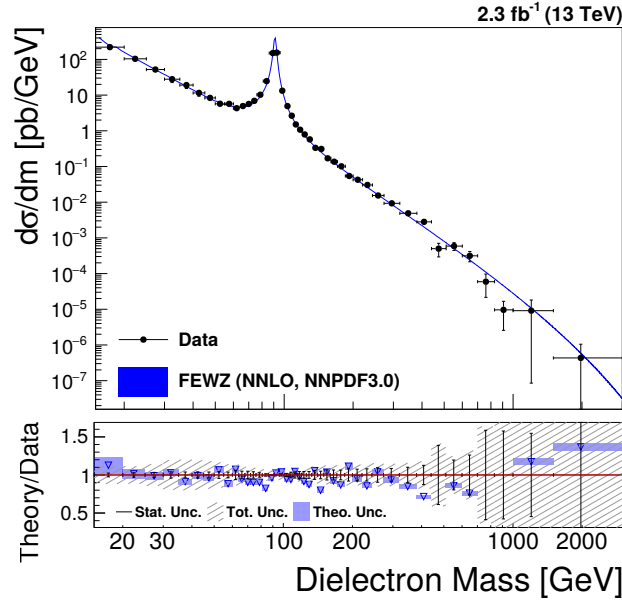


Figure 5.33: The Drell-Yan differential cross section measurement performed as a function of dielectron invariant mass compared to the NNLO theoretical prediction from FEWZ for the full phase space. The data point abscissas are obtained according to eq. (6) in [126]. The bottom plot shows the ratio between data and theoretical prediction where the coloured box denotes theoretical uncertainty.

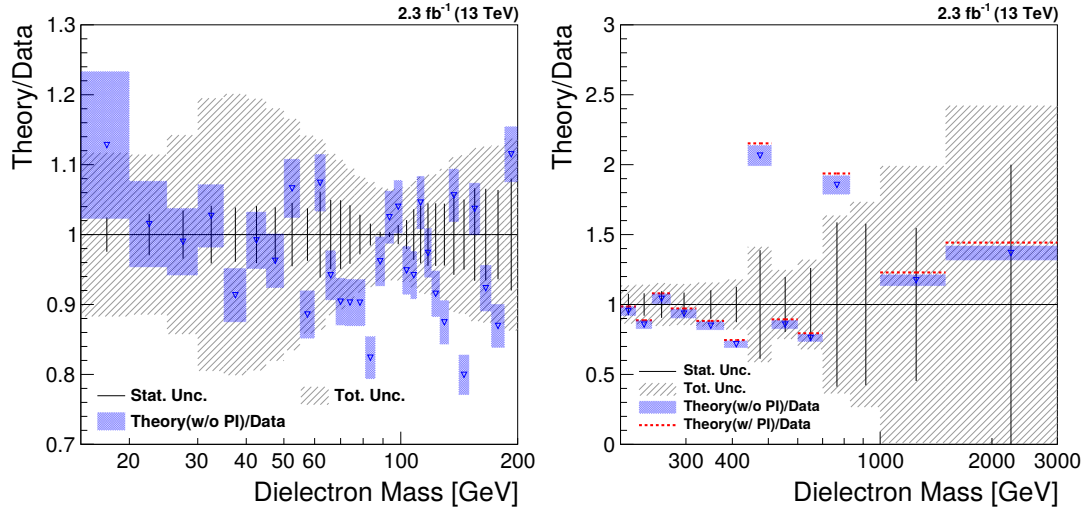


Figure 5.34: Ratio of theory to experimental data for the differential cross section as a function of dielectron invariant mass in the range $m < 200$ GeV (left) and $m > 200$ GeV (right). The blue band denotes the theoretical uncertainty on the ratio. In the right plot, the contribution from Photon-Induced backgrounds is shown in red colour and has a visible effect in the high mass region.

In order to check the dependence of PDFs in the high mass region $m > 200$ GeV, FEWZ calculation is obtained using various PDF sets. Figure 5.35 shows the ratio of theoretical prediction from different PDFs and the experimental data above 200 GeV. All the theoretical predictions are consistent amongst themselves as well as in agreement with the experimental result within the uncertainties.

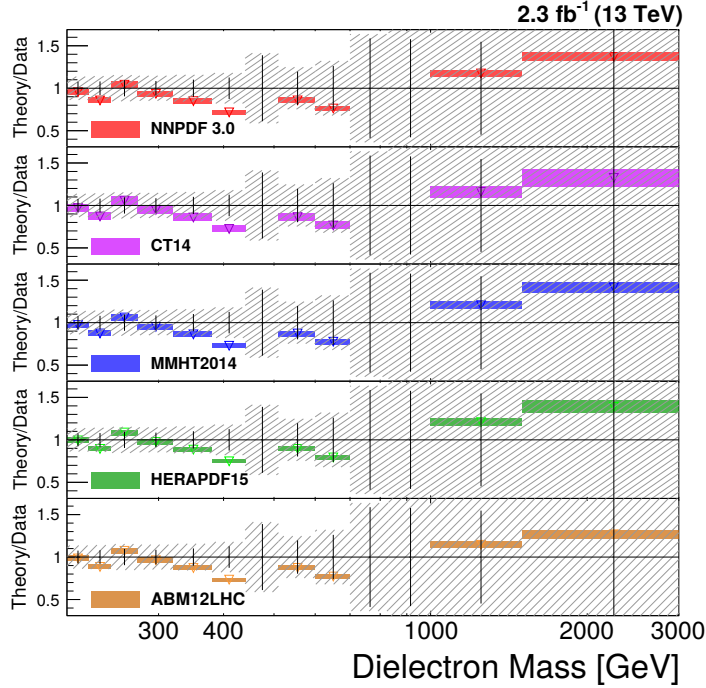


Figure 5.35: Ratio between experimental result and theoretical prediction from various PDFs for $m > 200$ GeV. The coloured band in the plot denotes theoretical uncertainty and the shaded band denotes total experimental uncertainty.

5.7.2.2 Combined Channel

To calculate the full phase space differential cross section in the combined channel, all the uncertainties are considered to be uncorrelated between the dielectron and dimuon channels, with an exception to the luminosity uncertainty and the systematic uncertainty from acceptance correction. The acceptance uncertainty is treated as correlated, since in each channel this uncertainty is based on theoretical calculations which use same PDF (NNPDF3.0) set.

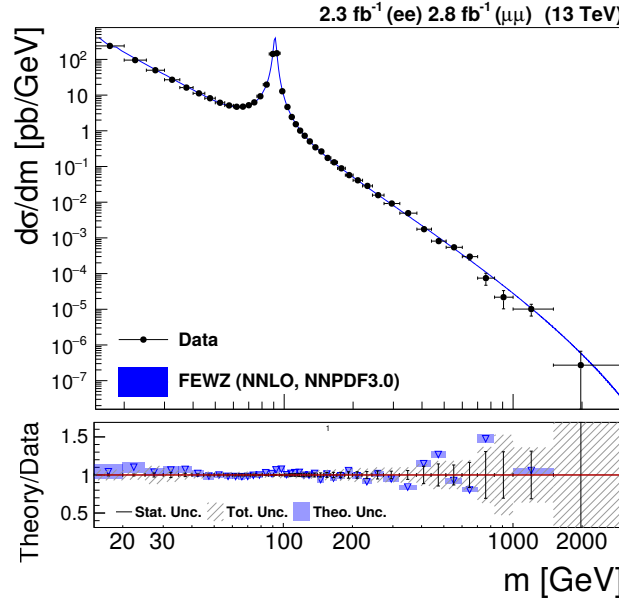


Figure 5.36: The Drell-Yan differential cross section measurement performed as a function of combined invariant mass compared to the NNLO theoretical prediction from FEWZ for the full phase space. The data point abscissas are obtained according to eq. (6) in [126]. The bottom plot shows the ratio between data and theoretical prediction where the coloured box denotes theoretical uncertainty.

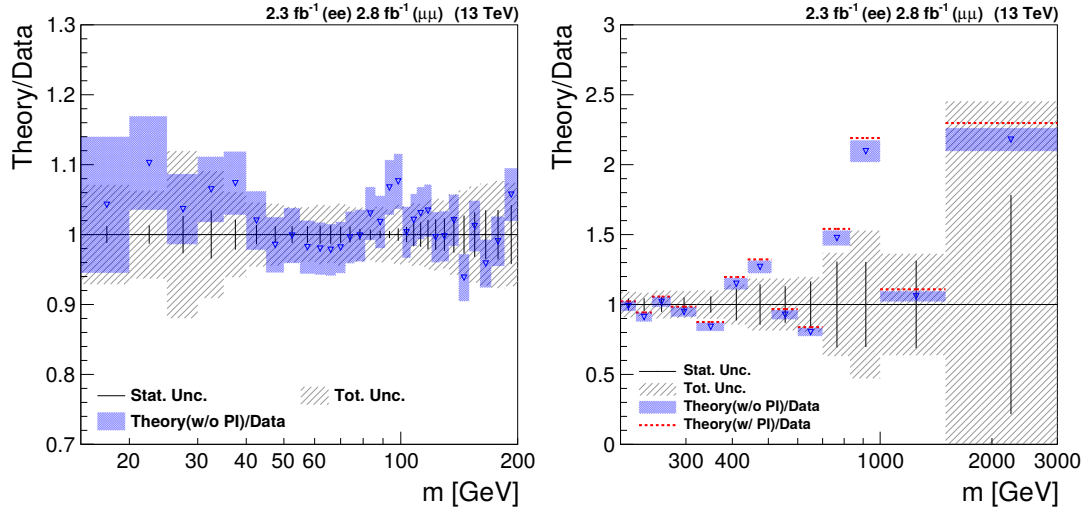


Figure 5.37: Ratio of theory to experimental data for the differential cross section as a function of combined invariant mass in the range $m < 200$ GeV (left) and $m > 200$ GeV (right). The blue band denotes the theoretical uncertainty on the ratio. In the right plot, the contribution from Photon-Induced backgrounds is shown in red colour and has a visible effect in the high mass region.

The correlation between the mass bins is however, treated differently for each type of uncertainty discussed in Sec. 5.6, while constructing the covariance matrix. The statistical uncertainty on the measured yield is considered as correlated between the mass bins. The systematic uncertainty, arising from the limitation of data or MC statistics is regarded as the uncertainty from statistical source and hence, considered to be correlated. The systematic uncertainties which are estimated by comparing different MC models, are however, assumed to be uncorrelated between the mass bins.

The result for the DY cross section measurement performed in the combined channel in full phase space region is presented in Fig. 5.36 and compared to theoretical prediction which uses the fixed-order NNLO QCD calculation and NLO EW correction to the DY production. Detailed numbers for the differential cross section in the combined channel are available in Table A.5. Figure 5.37 shows the

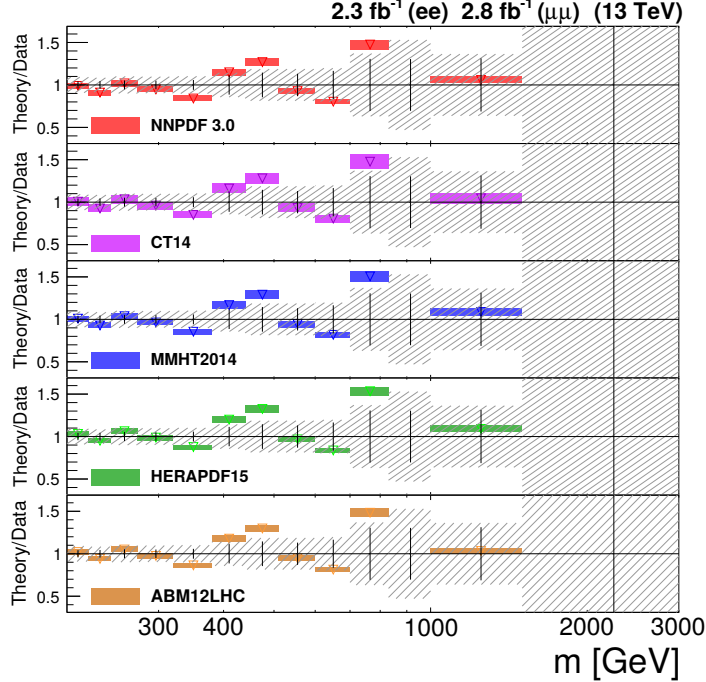


Figure 5.38: Ratio between experimental result and theoretical prediction from various PDFs for $m > 200$ GeV. The coloured band in the plot denotes theoretical uncertainty and the shaded band denotes total experimental uncertainty.

ratio between data and theoretical prediction in the mass range $m < 200$ GeV and $200 < m < 3000$ GeV. The result in the combined channel is found to be in good agreement with the NNLO theoretical predictions.

Similar to dielectron channel, in order to check the dependence of PDFs in the high mass region $m > 200$ GeV, FEWZ calculation is obtained using various PDF sets. Figure 5.38 shows the ratio of theoretical prediction from the PDFs and the combined experimental result above 200 GeV. It can be seen that all the theoretical predictions are consistent amongst themselves as well as in agreement with the measured result within the uncertainties.

Chapter 6

Summary

In this thesis, the Drell-Yan differential cross section $d\sigma/dm$ measurement is presented using proton-proton collision data collected with the CMS experiment at the LHC during the year 2015 corresponding to an integrated luminosity of 2.3 fb^{-1} . The cross section is measured in the dielectron final state over a wide range of invariant mass region $15 < m < 3000 \text{ GeV}$. Signal events are characterized by the presence of two electrons consistent with the Z boson decay. There are various background processes which can mimic the signal and contribute to the final state depending on the dielectron mass region. The dominant background processes in the entire mass range are $t\bar{t}$ along with single-top, while $\text{DY} \rightarrow \tau\tau$ contributes in the low mass, below the Z -peak region. Other sub-dominant background processes include WW , WZ , ZZ and W +jets and the QCD hadronic decay which contributes mainly in the high mass region. To reduce the contamination from these background processes, events triggered with a single electron trigger, having a minimum threshold on the transverse momentum (p_T) are selected. A kinematical requirement based on the p_T of leading and sub-leading electrons is applied. The electrons which get misreconstructed and misidentified (jet faking as an electron) in the detector acceptance are rejected by applying an efficient and effective identification criteria and a requirement to pass the particle flow isolation. The efficiencies for the trigger selection,

reconstruction and identification of electrons are computed using a data-driven approach called the tag and probe method. Measured efficiencies obtained from the data are found to be in good agreement with the Monte-Carlo simulations.

Although, the background contribution obtained from Monte-Carlo prediction is found to be reliable, main backgrounds are estimated using data-driven control samples. The electroweak processes namely $t\bar{t}$, single-top (tW and $\bar{t}W$), DY production of $\tau\tau$ pairs and diboson (WW) are estimated from the $e\mu$ control sample, based on the reconstruction of $e\mu$ pair normalized to e^+e^- final state. The e^+e^- background events estimated from the data correspond to a total of 26629 ± 163 and are in good agreement with 27605 ± 166 events predicted by Monte-Carlo simulation. The QCD and W +jets, with at least one misidentified electron are estimated by measuring the probability of a jet to fake an electron using a sample dominated by the jets. The fake rate is found to vary up to 0.5% and is applied on two different control samples prepared from electrons, passing or failing the selection criteria used in this analysis, in order to estimate QCD and W +jets. The other remaining backgrounds WZ and ZZ with only a small contribution to the dielectron mass spectrum are estimated from Monte-Carlo prediction.

The Z boson production cross section in the peak region $60 < m < 120$ GeV and the differential cross section $d\sigma/dm$ in the bins of invariant mass within the range $15 < m < 3000$ GeV are obtained from the experimental data in the full phase space and the fiducial region calculated within the detector acceptance. The measurement is corrected for limited detector resolution causing migration of events between mass bins, acceptance to take into account the coverage of CMS detector, difference in reconstruction, identification and trigger efficiencies between the data and the Monte-Carlo simulation and the final state radiation effects where the radiating photons can lead to smaller observed mass compared to pre-FSR mass.

The Drell-Yan cross section obtained in the muonic and electronic final states are compatible to each other and hence, the results are combined using the BLUE

method. This technique takes into account the correlation between uncertainties on the measured data. The statistical and systematic uncertainties are considered to be uncorrelated, except the uncertainties from luminosity measurement and acceptance correction. The treatment on the correlation between the mass bins depends on the type of uncertainty. The statistical uncertainty and the systematic uncertainties arising from the limitation of statistics in data or MC are considered to be correlated between the mass bins. However, the systematic uncertainties estimated by the comparison of different MC models, are taken to be uncorrelated.

The absolute Z -peak cross section in full phase space is found to be 1949 ± 2 (stat.) ± 96 (exp. syst.) ± 47 (th. syst.) ± 45 (lum.) pb in the dielectron channel and 1908 ± 1 (stat.) ± 25 (exp. syst.) ± 37 (th. syst.) ± 44 (lum.) pb in the combined channel. The differential cross section measurement in the dielectron channel is compared bin-by-bin with the Standard Model theoretical predictions at (1) NNLO prediction calculated with FEWZ 3.1 using NNPDF3.0 parton distribution function, as shown in Fig. 5.31 and (2) NLO prediction calculated with MADGRAPH5_AMC@NLO, as shown in Fig. 5.32. The corrected experimental results are found to be in good agreement with the theoretical predictions. The combined cross section is compared to the theoretical prediction available at NNLO calculated with FEWZ 3.1 using NNPDF3.0 parton distribution function, as can be seen in Fig. 5.36. A good agreement is observed with the theory.

The measurement of the differential cross section from the experimental data, can allow for a more precise determination of parton distribution functions and a better understanding of their uncertainties, which is essential to make predictions for physical cross sections. The study performed in this analysis leads to a confirmation of the predictions associated with the Standard Model. It is of utmost importance for building new models related to the physics of dark matter particles, to incorporate the full theory of gravitation, unification of strong and electroweak forces and other studies which go beyond the Standard Model predictions.

Chapter 7

Hardware and Software Activities Undertaken

The physics program at the LHC began in 2009 with proton-proton collisions at a center-of-mass energy of 7 TeV. By the year 2012, the energy was increased to 8 TeV. Throughout this period known as Run-I, the LHC operated with a bunch spacing of 50 ns. The CMS provided an excellent performance and collected the collision data with an integrated luminosity of 6.1 fb^{-1} and 23.3 fb^{-1} at center-of-mass energies of 7 TeV and 8 TeV, respectively. In early 2013, the CERN accelerator complex was shut down for two years for a planned maintenance and reinforcement, in order to meet the original performance goal to operate at an instantaneous luminosity of $10^{34} \text{ cm}^{-2} \text{ s}^{-1}$ with 25 ns bunch spacing. The period from 2013-2015 is referred to as the Long Shutdown 1 (LS1). The upgrade prepared the experiments, accelerators and electronics for running the LHC at a higher energy of 13 TeV and supported full performance of the CMS experiment at the high instantaneous luminosity.

During LS1, we participated in the upgrade of the photodetectors used to detect the scintillating light in the Hadron Outer (HO) sub-system of the Hadron Calorimeter (HCAL) as well as in the replacement of the back-end electronics system of the HCAL at the CMS detector.

7.1 Upgrade of Hadron Outer Calorimeter

In the original design, the wavelength shifted scintillator light produced in the HCAL was read out by Hybrid Photo Diodes (HPDs) [127], which were later found to be pessimal in the run conditions during the CMS operation, due to the following reasons:

- Affected by the fringe magnetic field of the solenoid
- Low photon detection efficiency
- Low signal to noise resolution

A drop-in replacement for the front-end electronics was based on the Silicon Photo Multiplier (SiPM) [128, 129] technology. The new photodetectors developed by the CMS HCAL group are insensitive to the magnetic interference, have high photon detection efficiency and better signal to noise ratio over the previously used HPDs.

7.1.1 Silicon Photo Multipliers

The SiPM used for the HO is the Hamamatsu Multi-Pixel Photon Counter (MPPC) device with a cell pitch of 50 μm and an active area of $3 \times 3 \text{ mm}$. These devices have 3600 micro pixels which correspond to a dynamic range of 2500 photo-electrons (pe). The MPPC has a photon detection efficiency (PDE) of 25% to 30%, which is better than 15% PDE for the HPDs at a wavelength of about 500 nm. The operating voltage is of the order of 70 V with a gain that is around 6×10^5 when operated 1 V above the breakdown voltage (BV). The gain in MPPS depends linearly on the temperature and corresponds to a maximal relative dependence of 8% gain shift per degree C at an operating point of 1.5 V over-voltage.

The MPPC photodetector and front-end electronics are arranged in crates (RBX) installed inside the magnet return yoke. The photodetectors and the electronics housed in the crates form independent Readout Modules (RMs). The drop-in

control system consists of a stack of three printed circuit boards (PCB). The mounting board (MB) which holds an array of 18 SiPMs and a Peltier cooler to regulate constant temperature of the SiPM is shown in Fig. 7.1. The control board (CB) monitors the operation of the individual SiPM and the Peltier. Lastly, the bias board (BB) generates the operating voltage for the SiPM.

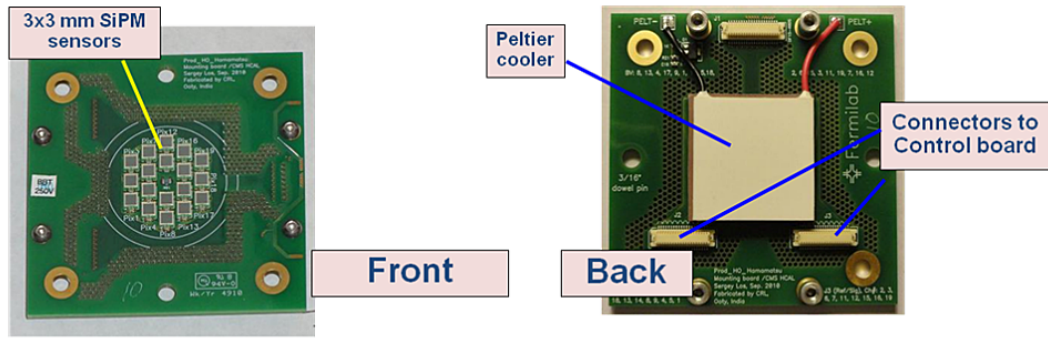


Figure 7.1: Photographs of the two sides of the Mounting Board. Taken from [129].

The old photodetectors were replaced by SiPMs in the RMs which were then installed in the five rings of the HO detector. We participated in the installation of RMs as a part of upgrade project for the HO front-end electronics.

7.1.2 SiPM Operation

The proper functioning of the new photo-sensors is of critical importance. It includes the optimization of the operation voltage which needs to be stable at the level of 15 mV in order to achieve a gain stability of 1%, variation of the BV with the temperature of the device and a need to control the temperature of the SiPM to be regulated better than 0.1^0 C. Hence, the measurement and verification of the SiPM operational parameters is performed. In this work, the study of the relative variation in gain and BV was carried out as described in the following sections.

7.1.2.1 Relative Variation in Gain

The relative variation of gain is monitored using a number of pedestal (PED) runs for which the SiPM signal is digitized corresponding to the LHC clock. The relative difference is obtained with respect to a reference PED run and found to be within 3% for all the SiPMs, as can be seen in Fig. 7.2. This demonstrates the stability of gain during the SiPM operation.

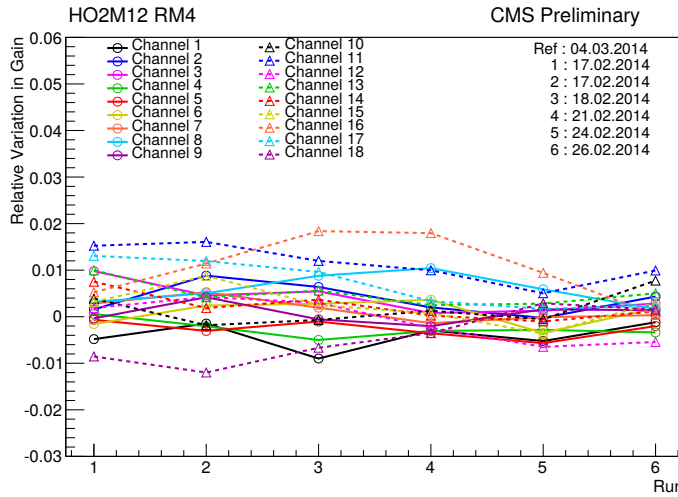


Figure 7.2: Relative variation of the gain determined over time using the pedestal method for one Readout Module (18 channels)³⁰.

7.1.2.2 Relative Variation in Breakdown Voltage

The relative variation of the BV is determined by considering an LED system which monitors the stability of the SiPMs outside the collisions. The LED light is adjusted such that the intensity is low enough to avoid saturation of SiPMs and the average signal from all SiPMs is uniform. The difference in the BV is presented in Fig. 7.3 calculated with respect to a reference LED run and the measurement is found to be stable within 50 mV. These results were presented at the CALOR 2014 conference [130].

³⁰Source : CMS Internal Detector Note, CMS DN-14-019.

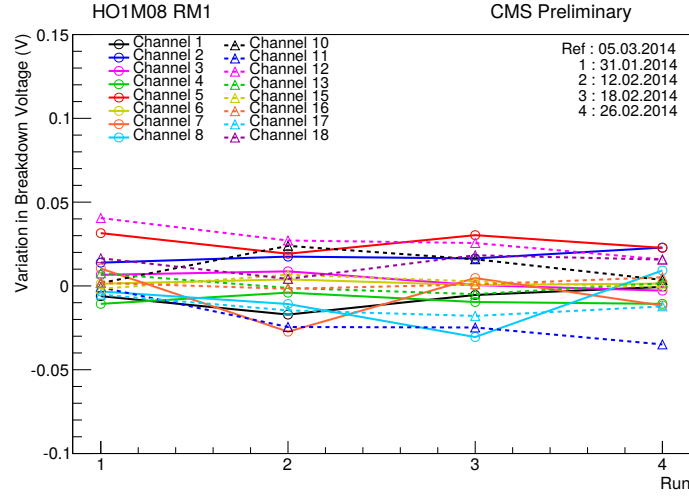


Figure 7.3: Relative variation of the breakdown voltage determined over time using LED settings for one Readout Module (18 channels)³¹.

Along with the contribution to the study of SiPM operational properties, we participated in taking a number of runs with PED and LED settings using an online software program.

7.2 HCAL Back-End Upgrade

During Run-I, the HCAL back-end electronics utilized VERSABus Memory card (VME) based system for the collection of data. However, with an increase in the center-of-mass energy from 8 TeV to 13 TeV, there was a need for high speed and continued acquisition of large amount of data, due to an increase in the number of interactions per bunch crossing (pileup). Since, VME based technology was unable to serve this purpose because of their limited data taking speed, the immediate solution was to replace the VME system with microTCA (μ TCA). The μ TCA technology provides an optical data rate of 4.8 Gbps over 1.6 Gbps from VME system, thus providing a high speed data transfer with efficient and long functional lifetime.

³¹Source : CMS Internal Detector Note, CMS DN-14-019.

7.2.1 MicroTCA

The μ TCA stands for Micro Telecommunication and Computing Architecture [131]. The μ TCA standard [132] was developed by the telecommunication industry and is based on the Advanced Mezzanine Card (AMC) standard [133].

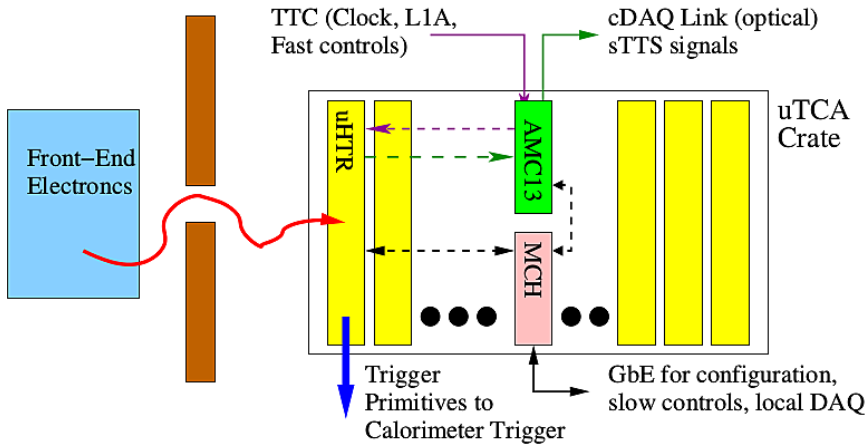


Figure 7.4: The μ TCA crate layout showing the data links from front-end electronics to the μ HTR cards, connections between the μ HTR cards and the calorimeter trigger and data acquisition system connected to the AMC13. Taken from [131].

It allows up to twelve standard AMC cards, known as the Micro HCAL and Readout (μ HTR) cards and two μ TCA Carrier Hub (MCH) sites in a μ TCA crate. The primary MCH site is occupied by a commercial MCH card responsible for crate management, while the secondary site is occupied by a CMS-common card, known as AMC13 card, responsible for data acquisition and distribution of LHC clock. When a μ HTR card is inserted into the crate, the MCH starts a communication via I2C³² protocol with a sub-component of the AMC called the Mezzanine Management Controller (MMC). A 12 V payload power to AMC is turned on by the MCH, once it is confirmed that the required electrical power is available. The power consumed by the electronic components on each μ HTR card is provided by a set of three power mezzanines (PM) and two auxiliary power mezzanines (APM).

³²I2C stands for Inter Integrated Circuit.

A specific electronics program was designed for the review of the μ HTR cards. It demonstrated that the designed electronics will be able to meet the upgrade requirements as well as validate the stable operation of the data links and latency in the front-end/back-end data link. The testing of the μ HTR cards ensured that:

- Sufficient power is supplied to the MCH card
- Proper communication is established between the MCH and the μ TCA crate
- A 12 V supply is provided to the μ HTR cards

As a part of this project, a μ TCA set-up was installed at the Department of Physics, Panjab University (Chandigarh) to perform the testing of the μ HTR cards.

7.2.2 Testing of Power Mezzanines

The voltage to various parts of the μ HTR card is provided by the power mezzanine (PM/APM). The working of mezzanines is crucial to ensure a high data collection efficiency. In order to test its stability, a power mezzanine testing program was designed as shown in Fig. 7.5, to rigorously monitor the functioning of PM/APM for a period of 39 hours. During the test, the mezzanines were inserted into the appropriate slots on the test board, consisting of three/two slots for PM/APM. The test was performed in four stages:

- Marginal up (1/2 hour) and Marginal down (1/2 hour)
- Nominal (19 hour) and High Load Nominal (19 hour)

The marginal mode was used by setting the output voltage 5% up or down, followed by the long test of the nominal settings. During each test, the output parameters: voltage, current, power and temperature of the modules were recorded in an output database after every 10 seconds. At the end of every test, average and extremum values of each parameter were used to evaluate the stability of the mezzanines.

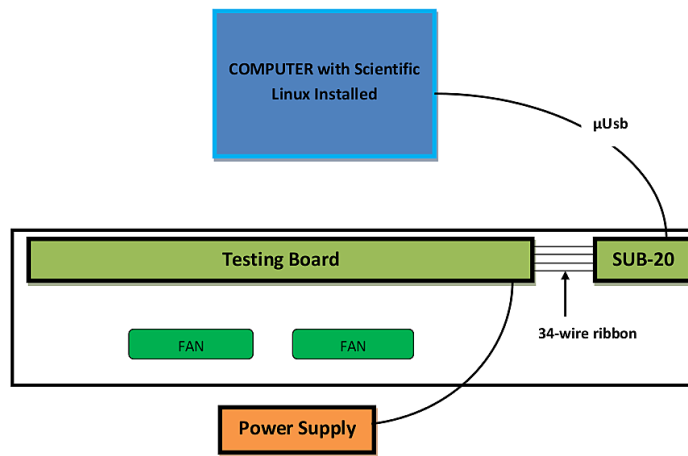


Figure 7.5: The set-up used for the testing of power mezzanines and auxiliary power mezzanines for a period of 39 hours. The communication between the test board and the computer is enabled through SUB-20³³ module via I2C protocol.

We successfully tested three sets of PM/APM using the set-up installed at the Department of Physics, Panjab University (Chandigarh), as shown in Fig. 7.6. During the CERN visits, we also participated in the testing of these cards at 904 building of CMS. The tested μ HTR cards were then installed in μ TCA crates at the CMS P5 site.

7.3 Other Activities

In addition to the activities discussed in the above sections, we participated in taking online Data Acquisition (DAQ) shifts at the CMS control room for the collection of data by the CMS and offline Muon DOC3 shifts for the certification of data collected by the muon sub-systems.

Apart from this, we also participated in the certification of data collected by the LHC and recorded by the CMS detector. The aim of the data certification activity is to deliver high quality data which can be used to perform physics analysis by various groups in the CMS collaboration. The data is defined as good if all the

³³Source : <http://www.xdimax.com/sub20/sub20.html>

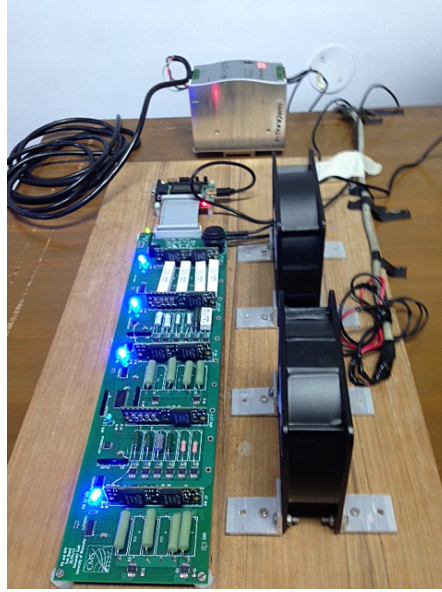


Figure 7.6: The power mezzanine (PM/AMP) testing set-up installed at the Department of Physics, Panjab University (Chandigarh).

sub-detectors, trigger and reconstructed physics objects which includes tracking, electron, photon, muon, jet and MET, show the expected performance. This work is carried out by the Data Certification (DC) and Data Quality Monitoring (DQM) group under the Physics Performance and Dataset (PPD) organization. In order to accomplish the certification task, the DC group prepares a list of data runs which are certified by the Detector Physics Group (DPG) and Physics Object Group (POG) certification experts. Once the individual groups complete the certification of runs, the central DC group produces a file in JSON (Java Script Object Notation) format that describes which luminosity sections in which runs are good for physics. As a part of this activity, we participated in the certification of runs collected during the year 2016 and 2017 at a center-of-mass energy $\sqrt{s} = 13$ TeV. Figure 7.7 shows the total luminosity delivered by the LHC, recorded by the CMS and validated as good for physics analysis in these two years³⁴. During 2016, LHC delivered 40.82 fb^{-1} of proton-proton collision data, out of which CMS recorded 37.76 fb^{-1} and validated

³⁴Source : <https://twiki.cern.ch/twiki/bin/viewauth/CMS/DataQuality>

35.92 fb⁻¹ data. Similarly in 2017, LHC delivered 49.98 fb⁻¹ of collision data, out of which CMS recorded 45.14 fb⁻¹ and validated 41.86 fb⁻¹ data.

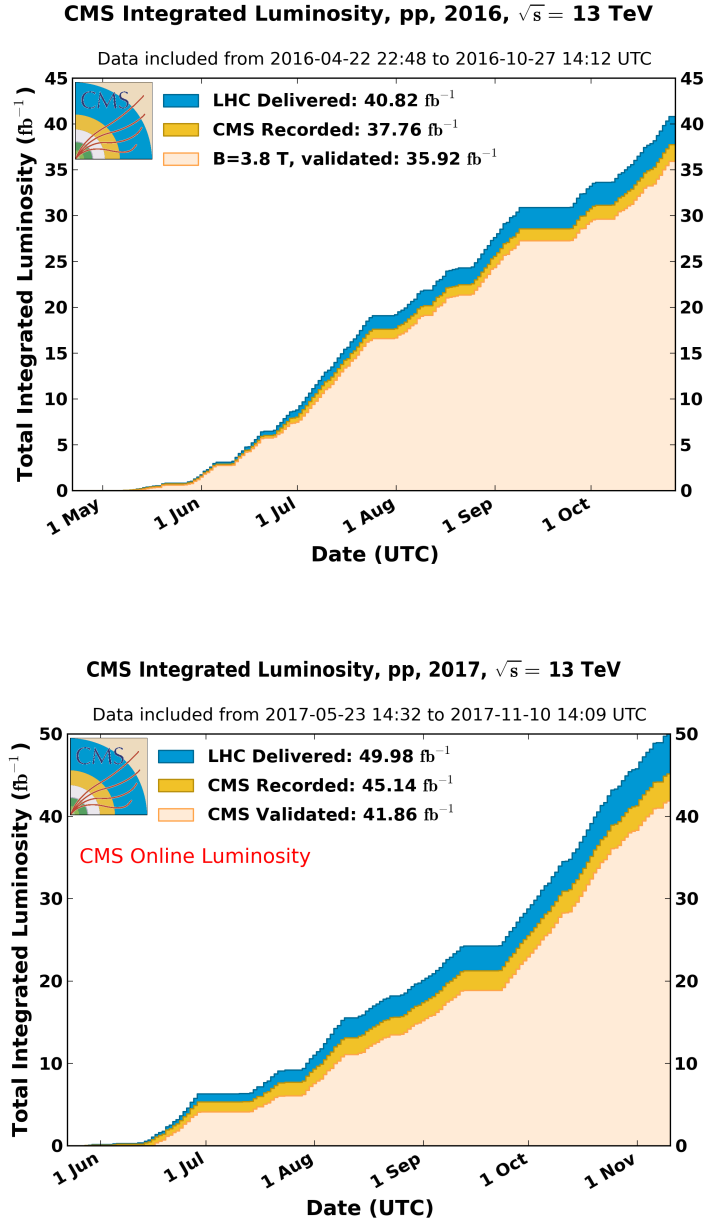


Figure 7.7: The plots show the total luminosity delivered by LHC, recorded by CMS and certified as good for physics analysis during the year 2016 (up) and 2017 (down). The luminosity validated for performing physics analysis corresponds to data recorded at center-of-mass energy $\sqrt{s} = 13$ TeV, with all sub-detectors and physics objects showing good performance.

Appendix A

A.1 A and R in data-driven $e\mu$ Method

Table A.1: The values of A and R obtained as a function of dielectron invariant mass. These numbers are used to estimate the true dielectron backgrounds from the data-driven $e\mu$ method by using the formulae described in Sec. 5.4.1.

m (GeV)	A	R
120-126	0.446	0.053
126-133	0.451	0
133-141	0.441	-0.024
141-150	0.448	0.021
150-160	0.436	0.036
160-171	0.447	0.012
171-185	0.446	0.038
185-200	0.442	0.043
200-220	0.452	0
220-243	0.452	0.025
243-273	0.439	0.017
273-320	0.449	-0.007
320-380	0.444	0.009
380-440	0.454	0
440-510	0.464	-0.116
510-600	0.457	0.202
600-700	0.447	0
700-830	0.367	0
830-1000	0.815	0
1000-1500	0.300	0
1500-3000	0	0

m (GeV)	A	R
15-20	0.512	-0.013
20-25	0.551	0.191
25-30	0.524	-0.004
30-35	0.557	0.062
35-40	0.625	0.076
40-45	0.581	0.041
45-50	0.478	0.032
50-55	0.457	0.018
55-60	0.492	0.029
60-64	0.488	0.019
64-68	0.478	0.048
68-72	0.444	0.041
72-76	0.458	0.054
76-81	0.479	0.026
81-86	0.485	0.001
86-91	0.479	0.009
91-96	0.456	-0.002
96-101	0.460	0.001
101-106	0.469	0.051
106-110	0.477	0.035
110-115	0.455	0.014
115-120	0.461	0.016

A.2 Systematic Uncertainties

Table A.2: Systematic uncertainties for $d\sigma/dm$ measurement in the dielectron channel. ‘Total’ refers to the quadrature sum of all sources of uncertainties except for the uncertainty from the acceptance correction.

m (GeV)	Scale (%)	Eff. SF (%)	Det. Res. (%)	Bkg. Est. (%)	FSR (%)	Total (%)	Acc. (%)
120-126	3.14	5.14	0.25	1.67	2.94	6.91	1.11
126-133	2.93	5.29	0.29	2.15	4.56	7.87	1.14
133-141	2.99	5.11	0.33	2.69	6.33	9.08	1.17
141-150	3.17	5.37	0.36	3.06	6.96	9.84	1.17
150-160	3.37	5.41	0.36	3.54	7.05	10.15	1.13
160-171	3.42	5.40	0.29	4.18	7.12	10.45	1.02
171-185	3.18	5.47	0.20	4.92	7.12	10.73	0.88
185-200	2.51	5.32	0.16	5.77	7.12	10.89	0.84
200-220	1.59	5.44	0.16	6.35	7.13	11.10	0.89
220-243	0.93	5.52	0.21	6.90	7.16	11.41	0.73
243-273	0.75	5.64	0.31	7.55	6.94	11.73	0.67
273-320	0.76	5.64	0.36	7.92	6.44	11.70	0.64
320-380	0.77	5.68	0.36	8.13	6.30	11.78	0.56
380-440	0.80	5.58	0.36	8.96	6.57	12.46	0.48
440-510	0.84	5.72	0.36	10.38	6.73	13.66	0.41
510-600	0.86	5.63	0.36	11.10	8.04	14.84	0.37
600-700	0.86	5.65	0.41	13.46	11.22	18.43	0.33
700-830	0.86	5.52	0.51	19.25	13.88	24.39	0.28
830-1000	0.77	5.45	0.57	42.63	14.01	45.21	0.25
1000-1500	0.59	5.34	0.57	81.43	12.52	82.57	0.36
1500-3000	0.51	5.24	0.57	100.29	11.68	101.11	0.66

m (GeV)	Scale (%)	Eff. SF (%)	Det. Res. (%)	Bkg. Est. (%)	FSR (%)	Total (%)	Acc. (%)
15-20	0.72	8.92	0.12	0.98	3.54	9.67	5.69
20-25	1.01	9.03	0.22	1.48	3.14	9.73	4.71
25-30	1.25	8.93	0.32	2.00	3.07	9.74	9.52
30-35	1.47	9.62	0.42	2.52	3.42	10.63	15.65
35-40	1.64	10.27	0.56	3.31	3.95	11.62	15.79
40-45	1.86	11.22	0.64	4.19	4.20	12.84	13.81
45-50	2.10	11.43	0.51	4.67	4.00	13.16	11.51
50-55	2.25	11.03	0.28	4.59	3.47	12.64	9.39
55-60	2.45	9.69	0.19	4.21	2.41	11.11	7.57
60-64	2.73	8.66	0.41	3.66	1.15	9.87	6.68
64-68	2.87	7.40	0.77	2.80	0.71	8.48	5.59
68-72	2.72	7.01	0.98	2.00	0.87	7.89	4.74
72-76	2.28	6.40	0.89	1.37	0.96	7.05	4.04
76-81	1.59	6.31	0.61	0.77	0.99	6.65	3.39
81-86	0.88	6.23	0.39	0.30	1.05	6.39	2.79
86-91	0.43	5.68	0.31	0.07	1.35	5.87	2.31
91-96	0.41	5.48	0.36	0.06	1.85	5.81	1.93
96-101	0.73	5.30	0.49	0.20	2.09	5.77	1.62
101-106	1.50	5.23	0.57	0.47	2.09	5.88	1.37
106-110	2.70	5.11	0.51	0.81	2.09	6.22	1.23
110-115	3.56	5.13	0.37	1.14	2.18	6.72	1.13
115-120	3.55	5.15	0.26	1.41	2.38	6.84	1.11

A.3 Full Phase Space Measurement

Table A.3: Full phase space $d\sigma/dm$ measurement in the dielectron channel. ‘Total’ refers to quadrature sum of statistical, experimental and theoretical uncertainties.

m (GeV)	Central value (pb/GeV)	Stat. Unc. (pb/GeV)	Exp. Unc. (pb/GeV)	Theo. Unc. (pb/GeV)	Total Unc. (pb/GeV)
120-126	7.9×10^{-1}	3.5×10^{-2}	5.8×10^{-2}	8.8×10^{-3}	6.8×10^{-2}
126-133	5.8×10^{-1}	2.5×10^{-2}	4.7×10^{-2}	6.6×10^{-3}	5.4×10^{-2}
133-141	3.3×10^{-1}	1.9×10^{-2}	3.1×10^{-2}	3.9×10^{-3}	3.7×10^{-2}
141-150	3.1×10^{-1}	1.6×10^{-2}	3.1×10^{-2}	3.6×10^{-3}	3.5×10^{-2}
150-160	1.7×10^{-1}	1.1×10^{-2}	1.8×10^{-2}	1.9×10^{-3}	2.1×10^{-2}
160-171	1.4×10^{-1}	8.9×10^{-3}	1.5×10^{-2}	1.4×10^{-3}	1.7×10^{-2}
171-185	1.0×10^{-1}	6.5×10^{-3}	1.1×10^{-2}	9.0×10^{-4}	1.3×10^{-2}
185-200	5.4×10^{-2}	4.3×10^{-3}	6.1×10^{-3}	4.6×10^{-4}	7.5×10^{-3}
200-220	4.3×10^{-2}	3.2×10^{-3}	4.8×10^{-3}	3.8×10^{-4}	5.8×10^{-3}
220-243	3.0×10^{-2}	2.4×10^{-3}	3.5×10^{-3}	2.2×10^{-4}	4.3×10^{-3}
243-273	1.5×10^{-2}	1.5×10^{-3}	1.8×10^{-3}	1.0×10^{-4}	2.4×10^{-3}
273-320	9.3×10^{-3}	7.9×10^{-4}	1.1×10^{-3}	6.0×10^{-5}	1.4×10^{-3}
320-380	4.9×10^{-3}	5.0×10^{-4}	5.9×10^{-4}	2.7×10^{-5}	7.7×10^{-4}
380-440	2.8×10^{-3}	3.6×10^{-4}	3.6×10^{-4}	1.3×10^{-5}	5.0×10^{-4}
440-510	5.0×10^{-4}	1.9×10^{-4}	6.9×10^{-5}	2.0×10^{-6}	2.1×10^{-4}
510-600	5.9×10^{-4}	1.2×10^{-4}	8.9×10^{-5}	2.2×10^{-6}	1.5×10^{-4}
600-700	3.1×10^{-4}	8.2×10^{-5}	5.8×10^{-5}	1.0×10^{-6}	1.0×10^{-4}
700-830	5.9×10^{-5}	3.5×10^{-5}	1.5×10^{-5}	1.7×10^{-7}	3.8×10^{-5}
830-1000	9.6×10^{-6}	5.6×10^{-6}	4.4×10^{-6}	2.5×10^{-8}	7.1×10^{-6}
1000-1500	9.1×10^{-6}	5.0×10^{-6}	7.5×10^{-6}	3.3×10^{-8}	9.0×10^{-6}
1500-3000	4.3×10^{-7}	4.3×10^{-7}	4.4×10^{-7}	2.8×10^{-9}	6.2×10^{-7}

m (GeV)	Central value (pb/GeV)	Stat. Unc. (pb/GeV)	Exp. Unc. (pb/GeV)	Theo. Unc. (pb/GeV)	Total Unc. (pb/GeV)
15-20	2.2×10^2	5.4×10^0	2.2×10^1	1.3×10^1	2.6×10^1
20-25	1.0×10^2	3.1×10^0	1.0×10^1	4.9×10^0	1.2×10^1
25-30	5.2×10^1	1.8×10^0	5.2×10^0	5.0×10^0	7.4×10^0
30-35	2.8×10^1	1.2×10^0	3.0×10^0	4.4×10^0	5.4×10^0
35-40	1.9×10^1	7.4×10^{-1}	2.3×10^0	3.0×10^0	3.8×10^0
40-45	1.2×10^1	4.7×10^{-1}	1.5×10^0	1.6×10^0	2.2×10^0
45-50	8.4×10^0	3.3×10^{-1}	1.1×10^0	9.6×10^{-1}	1.5×10^0
50-55	5.7×10^0	2.6×10^{-1}	7.4×10^{-1}	5.4×10^{-1}	9.5×10^{-1}
55-60	5.7×10^0	2.1×10^{-1}	6.5×10^{-1}	4.3×10^{-1}	8.1×10^{-1}
60-64	4.3×10^0	2.6×10^{-1}	4.4×10^{-1}	2.9×10^{-1}	5.9×10^{-1}
64-68	4.9×10^0	2.4×10^{-1}	4.3×10^{-1}	2.8×10^{-1}	5.7×10^{-1}
68-72	5.7×10^0	2.8×10^{-1}	4.6×10^{-1}	2.7×10^{-1}	6.0×10^{-1}
72-76	6.9×10^0	2.9×10^{-1}	5.1×10^{-1}	2.8×10^{-1}	6.5×10^{-1}
76-81	1.0×10^1	2.9×10^{-1}	7.2×10^{-1}	3.5×10^{-1}	8.5×10^{-1}
81-86	2.5×10^1	3.9×10^{-1}	1.7×10^0	6.9×10^{-1}	1.9×10^0
86-91	1.5×10^2	6.1×10^{-1}	9.5×10^0	3.5×10^0	1.0×10^1
91-96	1.5×10^2	5.5×10^{-1}	9.7×10^0	3.0×10^0	1.0×10^1
96-101	1.3×10^1	1.8×10^{-1}	8.2×10^{-1}	2.1×10^{-1}	8.7×10^{-1}
101-106	4.9×10^0	1.0×10^{-1}	3.1×10^{-1}	6.7×10^{-2}	3.3×10^{-1}
106-110	2.6×10^0	9.6×10^{-2}	1.8×10^{-1}	3.3×10^{-2}	2.0×10^{-1}
110-115	1.5×10^0	6.2×10^{-2}	1.1×10^{-1}	1.7×10^{-2}	1.2×10^{-1}
115-120	1.1×10^0	4.8×10^{-2}	7.8×10^{-2}	1.2×10^{-2}	9.2×10^{-2}

A.4 Fiducial Measurement

Table A.4: Fiducial $d\sigma/dm$ measurement in the dielectron channel. ‘Total’ refers to quadrature sum of statistical and experimental uncertainties.

m (GeV)	Central value (pb/GeV)	Stat. Unc. (pb/GeV)	Exp. Unc. (pb/GeV)	Total Unc. (pb/GeV)
120-126	2.0×10^{-1}	7.9×10^{-3}	1.4×10^{-2}	1.6×10^{-2}
126-133	1.5×10^{-1}	5.8×10^{-3}	1.0×10^{-2}	1.2×10^{-2}
133-141	9.3×10^{-2}	4.5×10^{-3}	6.4×10^{-3}	7.9×10^{-3}
141-150	8.6×10^{-2}	3.8×10^{-3}	6.3×10^{-3}	7.4×10^{-3}
150-160	5.2×10^{-2}	2.9×10^{-3}	3.9×10^{-3}	4.9×10^{-3}
160-171	4.1×10^{-2}	2.3×10^{-3}	3.3×10^{-3}	4.0×10^{-3}
171-185	3.0×10^{-2}	1.7×10^{-3}	2.5×10^{-3}	3.0×10^{-3}
185-200	1.9×10^{-2}	1.3×10^{-3}	1.6×10^{-3}	2.1×10^{-3}
200-220	1.5×10^{-2}	9.7×10^{-4}	1.3×10^{-3}	1.6×10^{-3}
220-243	1.0×10^{-2}	7.5×10^{-4}	9.6×10^{-4}	1.2×10^{-3}
243-273	5.6×10^{-3}	4.7×10^{-4}	5.4×10^{-4}	7.2×10^{-4}
273-320	3.5×10^{-3}	2.8×10^{-4}	3.5×10^{-4}	4.5×10^{-4}
320-380	2.0×10^{-3}	1.8×10^{-4}	2.0×10^{-4}	2.7×10^{-4}
380-440	1.2×10^{-3}	1.4×10^{-4}	1.2×10^{-4}	1.9×10^{-4}
440-510	2.4×10^{-4}	7.7×10^{-5}	2.9×10^{-5}	8.2×10^{-5}
510-600	2.7×10^{-4}	4.9×10^{-5}	3.5×10^{-5}	6.0×10^{-5}
600-700	1.4×10^{-4}	3.5×10^{-5}	2.1×10^{-5}	4.1×10^{-5}
700-830	2.9×10^{-5}	1.6×10^{-5}	5.8×10^{-6}	1.7×10^{-5}
830-1000	6.0×10^{-6}	3.5×10^{-6}	2.6×10^{-6}	4.3×10^{-6}
1000-1500	5.0×10^{-6}	2.7×10^{-6}	4.1×10^{-6}	4.9×10^{-6}
1500-3000	2.5×10^{-7}	2.5×10^{-7}	2.5×10^{-7}	3.6×10^{-7}

m (GeV)	Central value (pb/GeV)	Stat. Unc. (pb/GeV)	Exp. Unc. (pb/GeV)	Total Unc. (pb/GeV)
15-20	2.1×10^{-1}	4.8×10^{-3}	1.9×10^{-2}	2.0×10^{-2}
20-25	1.7×10^{-1}	4.8×10^{-3}	1.6×10^{-2}	1.7×10^{-2}
25-30	1.5×10^{-1}	4.9×10^{-3}	1.5×10^{-2}	1.5×10^{-2}
30-35	1.4×10^{-1}	5.0×10^{-3}	1.4×10^{-2}	1.5×10^{-2}
35-40	1.6×10^{-1}	5.6×10^{-3}	1.8×10^{-2}	1.9×10^{-2}
40-45	2.0×10^{-1}	6.7×10^{-3}	2.4×10^{-2}	2.5×10^{-2}
45-50	2.8×10^{-1}	8.3×10^{-3}	3.5×10^{-2}	3.6×10^{-2}
50-55	3.2×10^{-1}	1.0×10^{-2}	4.0×10^{-2}	4.1×10^{-2}
55-60	5.1×10^{-1}	1.2×10^{-2}	5.6×10^{-2}	5.8×10^{-2}
60-64	6.5×10^{-1}	2.0×10^{-2}	6.6×10^{-2}	6.9×10^{-2}
64-68	9.7×10^{-1}	2.5×10^{-2}	8.5×10^{-2}	8.8×10^{-2}
68-72	1.3×10^0	3.1×10^{-2}	1.1×10^{-1}	1.1×10^{-1}
72-76	1.9×10^0	3.7×10^{-2}	1.4×10^{-1}	1.5×10^{-1}
76-81	3.1×10^0	4.2×10^{-2}	2.2×10^{-1}	2.2×10^{-1}
81-86	7.0×10^0	6.2×10^{-2}	4.7×10^{-1}	4.8×10^{-1}
86-91	3.5×10^1	1.1×10^{-1}	2.1×10^0	2.1×10^0
91-96	3.0×10^1	1.0×10^{-1}	1.8×10^0	1.8×10^0
96-101	2.8×10^0	3.6×10^{-2}	1.7×10^{-1}	1.7×10^{-1}
101-106	1.1×10^0	2.1×10^{-2}	6.7×10^{-2}	7.0×10^{-2}
106-110	6.2×10^{-1}	1.9×10^{-2}	3.9×10^{-2}	4.4×10^{-2}
110-115	3.8×10^{-1}	1.3×10^{-2}	2.6×10^{-2}	2.9×10^{-2}
115-120	2.8×10^{-1}	1.1×10^{-2}	1.9×10^{-2}	2.2×10^{-2}

A.5 Full Phase Space Measurement

Table A.5: Full phase space $d\sigma/dm$ measurement in the combined channel. ‘Total’ refers to quadrature sum of statistical, experimental and theoretical uncertainties without luminosity uncertainty.

m (GeV)	Central value (pb/GeV)	Total Unc. (pb/GeV)
120-126	7.3×10^{-1}	3.7×10^{-2}
126-133	5.0×10^{-1}	2.5×10^{-2}
133-141	3.4×10^{-1}	2.0×10^{-2}
141-150	2.6×10^{-1}	1.7×10^{-2}
150-160	1.7×10^{-1}	1.2×10^{-2}
160-171	1.3×10^{-1}	9.6×10^{-3}
171-185	8.9×10^{-2}	6.8×10^{-3}
185-200	5.7×10^{-2}	4.2×10^{-3}
200-220	4.1×10^{-2}	3.8×10^{-3}
220-243	2.9×10^{-2}	2.4×10^{-3}
243-273	1.6×10^{-2}	1.6×10^{-3}
273-320	9.2×10^{-3}	8.9×10^{-4}
320-380	4.9×10^{-3}	5.0×10^{-4}
380-440	1.8×10^{-3}	2.5×10^{-4}
440-510	8.1×10^{-4}	1.5×10^{-4}
510-600	5.4×10^{-4}	1.0×10^{-4}
600-700	3.0×10^{-4}	5.9×10^{-5}
700-830	7.5×10^{-5}	2.8×10^{-5}
830-1000	2.2×10^{-5}	1.2×10^{-5}
1000-1500	1.0×10^{-5}	3.7×10^{-6}
1500-3000	2.7×10^{-7}	4.0×10^{-7}

m (GeV)	Central value (pb/GeV)	Total Unc. (pb/GeV)
15-20	2.4×10^2	1.7×10^1
20-25	9.6×10^1	6.0×10^0
25-30	5.0×10^1	5.9×10^0
30-35	2.7×10^1	2.4×10^0
35-40	1.6×10^1	9.9×10^{-1}
40-45	1.1×10^1	5.1×10^{-1}
45-50	8.2×10^0	3.6×10^{-1}
50-55	6.1×10^0	2.4×10^{-1}
55-60	5.1×10^0	2.0×10^{-1}
60-64	4.7×10^0	2.0×10^{-1}
64-68	4.8×10^0	1.9×10^{-1}
68-72	5.2×10^0	2.3×10^{-1}
72-76	6.3×10^0	2.5×10^{-1}
76-81	9.3×10^0	3.6×10^{-1}
81-86	2.0×10^1	7.2×10^{-1}
86-91	1.4×10^2	5.6×10^0
91-96	1.5×10^2	5.3×10^0
96-101	1.3×10^1	5.5×10^{-1}
101-106	4.7×10^0	1.9×10^{-1}
106-110	2.4×10^0	1.1×10^{-1}
110-115	1.5×10^0	6.7×10^{-2}
115-120	1.0×10^0	5.0×10^{-2}

Bibliography

- [1] G. Bozzi, S. Catani and G. Ferrera *et al.*, “Transverse-momentum resummation: A Perturbative study of Z production at the Tevatron”, Nucl. Phys. B **815**, 174 (2009) doi:10.1016/j.nuclphysb.2009.02.014 arXiv:0812.2862 [hep-ph].
- [2] Y. Li and F. Petriello, “Combining QCD and electroweak corrections to dilepton production in FEWZ”, Phys. Rev. D **86**, 094034 (2012) doi:10.1103/PhysRevD.86.094034 arXiv:1208.5967 [hep-ph].
- [3] CMS Collaboration, “Forward-backward asymmetry of DrellYan lepton pairs in pp collisions at $\sqrt{s} = 8$ TeV”, Eur. Phys. J. C **76**, no. 6, 325 (2016) doi:10.1140/epjc/s10052-016-4156-z arXiv:1601.04768 [hep-ex].
- [4] CMS Collaboration, “Measurement of the Drell-Yan Cross Section in pp Collisions at $\sqrt{s} = 7$ TeV”, JHEP **1110**, 007 (2011) doi:10.1007/JHEP10(2011)007 arXiv:1108.0566 [hep-ex].
- [5] CMS Collaboration, “Measurement of the differential and double-differential Drell-Yan cross sections in proton-proton collisions at $\sqrt{s} = 7$ TeV”, JHEP **1312**, 030 (2013) doi:10.1007/JHEP12(2013)030 arXiv:1310.7291 [hep-ex].
- [6] CMS Collaboration, “Measurements of differential and double-differential Drell-Yan cross sections in proton-proton collisions at 8 TeV”, Eur. Phys. J. C **75**, no. 4, 147 (2015) doi:10.1140/epjc/s10052-015-3364-2 arXiv:1412.1115 [hep-ex].

- [7] CMS Collaboration, “Measurement of the differential Drell-Yan cross section in proton-proton collisions at 13 TeV”, CMS-PAS-SMP-16-009.
- [8] D. Griffiths, “Introduction to Elementary Particles”, New York, USA: Wiley (1987).
- [9] D. Perkins, “Introduction to high energy physics”, Cambridge, UK: Cambridge University Press (1982).
- [10] M. Gaillard, P. Grannis and F. Sciulli, “The standard model of particle physics”, Rev. Mod. Phys. **71**, S96 (1999).
- [11] Particle Data Group, “Review of Particle Physics (RPP)”, Phys. Rev. D **86**, 010001 (2012) doi:10.1103/PhysRevD.86.010001.
- [12] M. Gell-Mann, “A Schematic Model of Baryons and Mesons”, Phys. Lett. **8**, 214 (1964) doi:10.1016/S0031-9163(64)92001-3.
- [13] S. Weinberg, “A Model of Leptons”, Phys. Rev. Lett. **19**, 1264 (1967) doi:10.1103/PhysRevLett.19.1264.
- [14] R. Ellis, W. Stirling and B. Webber, “QCD and Collider Physics”, Cambridge Monographs on Particle Physics, Nuclear Physics and Cosmology, Cambridge University Press (2003).
- [15] G. Dissertori, I. Knowles and M. Schmelling, Quantum Chromodynamics: High Energy Experiments and Theory, International Series of Monographs on Physics, OUP Oxford (2009).
- [16] A. Salam, “Gauge Unification of Fundamental Forces” Rev. Mod. Phys. **52**, 525 (1980) doi:10.1103/RevModPhys.52.525.
- [17] S. L. Glashow, “Towards a Unified Theory: Threads in a Tapestry”, Rev. Mod. Phys. **52**, 539 (1980) doi:10.1103/RevModPhys.52.539.

-
- [18] G. A. Blair, “Precision SUSY and the GUT Scale”, eConf C **0507252**, T031 (2005).
- [19] P. W. Higgs, “Broken Symmetries and the Masses of Gauge Bosons”, Phys. Rev. Lett. **13**, 508 (1964) doi:10.1103/PhysRevLett.13.508.
- [20] F. Englert and R. Brout, “Broken Symmetry and the Mass of Gauge Vector Mesons”, Phys. Rev. Lett. **13**, 321 (1964) doi:10.1103/PhysRevLett.13.321.
- [21] G. S. Guralnik, C. R. Hagen and T. W. B. Kibble, “Global Conservation Laws and Massless Particles”, Phys. Rev. Lett. **13**, 585 (1964) doi:10.1103/PhysRevLett.13.585.
- [22] ATLAS Collaboration, “Observation of a new particle in the search for the Standard Model Higgs boson with the ATLAS detector at the LHC”, Phys. Lett. B **716** (2012) 1 doi:10.1016/j.physletb.2012.08.020 arXiv:1207.7214 [hep-ex].
- [23] CMS Collaboration, “Observation of a new boson at a mass of 125 GeV with the CMS experiment at the LHC”, Phys. Lett. B **716**, 30 (2012) doi:10.1016/j.physletb.2012.08.021 arXiv:1207.7235 [hep-ex].
- [24] J. Goldstone, A. Salam and S. Weinberg, “Broken Symmetries”, Phys. Rev. **127**, 965 (1962) doi:10.1103/PhysRev.127.965.
- [25] A. Pich, “The Standard Model of Electroweak Interactions”, arXiv:1201.0537 [hep-ph].
- [26] S. D. Drell and T. M. Yan, “Partons and their Applications at High-Energies”, Annals Phys. **66**, 578 (1971) doi:10.1016/0003-4916(71)90071-6.
- [27] J. C. Collins and D. E. Soper, “The Theorems of Perturbative QCD”, Ann. Rev. Nucl. Part. Sci. **37**, 383 (1987) doi:10.1146/annurev.ns.37.120187.002123.

- [28] A. V. Lipatov, M. A. Malyshev and N. P. Zotov, “Drell-Yan lepton pair production at high energies in the k_t -factorization approach”, JHEP **1112**, 117 (2011) doi:10.1007/JHEP12(2011)117 arXiv:1110.6582 [hep-ph].
- [29] R. P. Feynman, “Very high-energy collisions of hadrons”, Phys. Rev. Lett. **23**, 1415 (1969) doi:10.1103/PhysRevLett.23.1415.
- [30] G. F. Sterman, “QCD and jets”, arXiv:hep-ph/0412013.
- [31] V. D. Barger and R. J. N. Phillips, “Collider Physics”, REDWOOD CITY, USA: ADDISON-WESLEY (1987) 592 P.
- [32] Y. L. Dokshitzer, “Calculation of the Structure Functions for Deep Inelastic Scattering and $e^+ e^-$ Annihilation by Perturbation Theory in Quantum Chromodynamics.”, Sov. Phys. JETP **46**, 641 (1977).
- [33] V. N. Gribov and L. N. Lipatov, “Deep inelastic $e p$ scattering in perturbation theory”, Sov. J. Nucl. Phys. **15**, 438 (1972).
- [34] G. Altarelli and G. Parisi, “Asymptotic Freedom in Parton Language”, Nucl. Phys. B **126**, 298 (1977) doi:10.1016/0550-3213(77)90384-4.
- [35] F. Halzen and A. D. Martin, “Quarks And Leptons: An Introductory Course In Modern Particle Physics”, New York, USA: Wiley (1984).
- [36] J. Pumplin, D. R. Stump and J. Huston *et al.*, “New generation of parton distributions with uncertainties from global QCD analysis”, JHEP **0207**, 012 (2002) doi:10.1088/1126-6708/2002/07/012 arXiv:[hep-ph/0201195].
- [37] A. D. Martin, W. J. Stirling and R. S. Thorne *et al.*, “Parton distributions for the LHC”, Eur. Phys. J. C **63**, 189 (2009) doi:10.1140/epjc/s10052-009-1072-5 arXiv:0901.0002 [hep-ph].

- [38] ZEUS and H1 Collaborations, “Extraction of the proton parton density functions using a NLO-QCD fit of the combined H1 and ZEUS inclusive DIS cross sections” doi:10.3360/dis.2008.25 arXiv:0808.1854 [hep-ph].
- [39] R. D. Ball, L. Del Debbio and S. Forte *et al.*, “A first unbiased global NLO determination of parton distributions and their uncertainties”, Nucl. Phys. B **838**, 136 (2010) doi:10.1016/j.nuclphysb.2010.05.008 arXiv:1002.4407 [hep-ph].
- [40] NNPDF Collaboration, “Parton distributions for the LHC Run II”, JHEP **1504**, 040 (2015) doi:10.1007/JHEP04(2015)040 arXiv:1410.8849 [hep-ph].
- [41] CDF Collaboration, “Studying the Underlying Event in Drell-Yan and High Transverse Momentum Jet Production at the Tevatron”, Phys. Rev. D **82**, 034001 (2010) doi:10.1103/PhysRevD.82.034001 arXiv:1003.3146 [hep-ex].
- [42] Y. K. Kim and U. K. Yang, “Initial State Gluon Radiation in Drell-Yan Dilepton Production”, CDF/PHYS/CDFR/6804 (2004).
- [43] J. M. Campbell, J. W. Huston and W. J. Stirling, “Hard Interactions of Quarks and Gluons: A Primer for LHC Physics”, Rept. Prog. Phys. **70**, 89 (2007) doi:10.1088/0034-4885/70/1/R02 arXiv:[hep-ph/0611148].
- [44] T. Sjostrand and M. van Zijl, “A Multiple Interaction Model for the Event Structure in Hadron Collisions”, Phys. Rev. D **36**, 2019 (1987) doi:10.1103/PhysRevD.36.2019.
- [45] S. D. Drell and T. M. Yan, “Massive Lepton Pair Production in Hadron-Hadron Collisions at High-Energies”, Phys. Rev. Lett. **25**, 316 (1970) doi:10.1103/PhysRevLett.25.316.
- [46] R. Field, “Applications of perturbative QCD Frontiers in physics”, Addison-Wesley, The Advanced Book Program (1989).

- [47] J. C. Collins, D. E. Soper and G. F. Sterman, “Factorization of Hard Processes in QCD”, *Adv. Ser. Direct. High Energy Phys.* **5**, 1 (1989) doi:10.1142/9789814503266_0001 arXiv:[hep-ph/0409313].
- [48] B. Delamotte, “A Hint of renormalization”, *Am. J. Phys.* **72**, 170 (2004) doi:10.1119/1.1624112 arXiv:[hep-th/0212049].
- [49] K. Melnikov and F. Petriello, “Electroweak gauge boson production at hadron colliders through $O(\alpha(s)^2)$ ”, *Phys. Rev. D* **74**, 114017 (2006) doi:10.1103/PhysRevD.74.114017 arXiv:[hep-ph/0609070].
- [50] U. Baur, O. Brein and W. Hollik *et al.*, “Electroweak radiative corrections to neutral current Drell-Yan processes at hadron colliders”, *Phys. Rev. D* **65**, 033007 (2002) doi:10.1103/PhysRevD.65.033007 arXiv:[hep-ph/0108274].
- [51] S. Moretti, M. R. Nolten and D. A. Ross, “Weak corrections to four-parton processes”, *Nucl. Phys. B* **759**, 50 (2006) doi:10.1016/j.nuclphysb.2006.09.028 [hep-ph/0606201].
- [52] L. Evans and P. Bryant, “LHC Machine”, *JINST* **3**, S08001 (2008) doi:10.1088/1748-0221/3/08/S08001.
- [53] ATLAS Collaboration, “The ATLAS Experiment at the CERN Large Hadron Collider”, *JINST* **3**, S08003 (2008) doi:10.1088/1748-0221/3/08/S08003.
- [54] CMS Collaboration, “The CMS Experiment at the CERN LHC”, *JINST* **3**, S08004 (2008) doi:10.1088/1748-0221/3/08/S08004.
- [55] TOTEM Collaboration, “The TOTEM experiment at the CERN Large Hadron Collider”, *JINST* **3**, S08007 (2008) doi:10.1088/1748-0221/3/08/S08007.
- [56] LHCf Collaboration, “The LHCf detector at the CERN Large Hadron Collider”, *JINST* **3**, S08006 (2008) doi:10.1088/1748-0221/3/08/S08006.

-
- [57] ALICE Collaboration, “The ALICE experiment at the CERN LHC”, JINST **3**, S08002 (2008) doi:10.1088/1748-0221/3/08/S08002.
- [58] LHCb Collaboration, “The LHCb Detector at the LHC”, JINST **3**, S08005 (2008) doi:10.1088/1748-0221/3/08/S08005.
- [59] W. Herr and B. Muratori, “Concept of luminosity”.
- [60] CMS Collaboration, “CMS Physics : Technical Design Report Volume 1: Detector Performance and Software”, CERN-LHCC-2006-001 <http://cds.cern.ch/record/922757>.
- [61] CMS Collaboration, “The CMS magnet project : Technical Design Report”, CERN-LHCC-97-010 <http://cds.cern.ch/record/331056>.
- [62] CMS Collaboration, “The CMS tracker system project : Technical Design Report”, CERN-LHCC-98-006 <http://cds.cern.ch/record/368412>.
- [63] CMS Collaboration, “The CMS tracker : addendum to the Technical Design Report”, CERN-LHCC-2000-016 <http://cds.cern.ch/record/490194>.
- [64] CMS Collaboration, “The CMS electromagnetic calorimeter project : Technical Design Report”, CERN-LHCC-97-033 <https://cds.cern.ch/record/349375>.
- [65] CMS Collaboration, “Changes to CMS ECAL electronics : addendum to the Technical Design Report”, CERN-LHCC-2002-027 <http://cds.cern.ch/record/581342>.
- [66] P. Lecoq *et al.*, “Lead tungstate (PbWO₄) scintillators for LHC EM calorimetry”, Nucl. Instrum. Meth. A **365**, 291 (1995) doi:10.1016/0168-9002(95)00589-7.

-
- [67] A. A. Annenkov, M. V. Korzhik and P. Lecoq, “Lead tungstate scintillation material”, Nucl. Instrum. Meth. A **490**, 30 (2002) doi:10.1016/S0168-9002(02)00916-6.
- [68] CMS Collaboration, “Avalanche photodiodes and vacuum phototriodes for the electromagnetic calorimeter of the CMS experiment at the Large Hadron Collider”, Nucl. Instrum. Meth. A **604**, 193 (2009) doi:10.1016/j.nima.2009.01.089.
- [69] P. Adzic *et al.*, “Energy resolution of the barrel of the CMS electromagnetic calorimeter”, JINST **2**, P04004 (2007) doi:10.1088/1748-0221/2/04/P04004.
- [70] CMS Collaboration, “The CMS hadron calorimeter project : Technical Design Report”, CERN-LHCC-97-031 <https://cds.cern.ch/record/357153>.
- [71] CMS Collaboration, “Performance of the CMS Hadron Calorimeter with Cosmic Ray Muons and LHC Beam Data”, JINST **5**, T03012 (2010) doi:10.1088/1748-0221/5/03/T03012 arXiv:0911.4991 [physics.ins-det].
- [72] CMS Collaboration, “The CMS muon project : Technical Design Report”, CERN-LHCC-97-032 <https://cds.cern.ch/record/343814>.
- [73] CMS Collaboration, “CMS TriDAS project : Technical Design Report, Volume 1: The Trigger Systems”, CERN-LHCC-2000-038 <https://cds.cern.ch/record/706847>.
- [74] N. Metropolis and S. Ulam, “The Monte Carlo Method”, Journal of the American Statistical Association **44** 247, 335-441 (1949) doi:10.1080/01621459.1949.10483310.
- [75] B. Andersson, G. Gustafson and G. Ingelman *et al.*, “Parton Fragmentation and String Dynamics”, Phys. Rept. **97**, 31 (1983) doi:10.1016/0370-1573(83)90080-7.

- [76] B. Andersson, G. Gustafson and B. Soderberg, “A General Model for Jet Fragmentation”, *Z. Phys. C* **20**, 317 (1983) doi:10.1007/BF01407824.
- [77] T. Sjostrand, “The Merging of Jets”, *Phys. Lett.* **142B**, 420 (1984) doi:10.1016/0370-2693(84)91354-6.
- [78] B. R. Webber, “A QCD Model for Jet Fragmentation Including Soft Gluon Interference”, *Nucl. Phys. B* **238**, 492 (1984) doi:10.1016/0550-3213(84)90333-X.
- [79] J. Alwall *et al.*, “MadGraph/MadEvent v4: The New Web Generation”, *JHEP* **0709**, 028 (2007) doi:10.1088/1126-6708/2007/09/028 arXiv:0706.2334 [hep-ph].
- [80] J. Alwall, M. Herquet and F. Maltoni *et al.*, “MadGraph 5 : Going Beyond”, *JHEP* **1106**, 128 (2011) doi:10.1007/JHEP06(2011)128 arXiv:1106.0522 [hep-ph].
- [81] S. Frixione and B. R. Webber, “Matching NLO QCD computations and parton shower simulations”, *JHEP* **0206**, 029 (2002) doi:10.1088/1126-6708/2002/06/029 arXiv:[hep-ph/0204244].
- [82] J. Alwall *et al.*, “The automated computation of tree-level and next-to-leading order differential cross sections, and their matching to parton shower simulations”, *JHEP* **1407**, 079 (2014) doi:10.1007/JHEP07(2014)079 arXiv:1405.0301 [hep-ph].
- [83] CMS Collaboration, “Event generator tunes obtained from underlying event and multiparton scattering measurements”, *Eur. Phys. J. C* **76**, no. 3, 155 (2016) doi:10.1140/epjc/s10052-016-3988-x arXiv:1512.00815 [hep-ex].
- [84] R. Frederix and S. Frixione, “Merging meets matching in MC@NLO”, *JHEP* **1212**, 061 (2012) doi:10.1007/JHEP12(2012)061 arXiv:1209.6215 [hep-ph].

-
- [85] T. Sjostrand, S. Mrenna and P. Z. Skands, “PYTHIA 6.4 Physics and Manual”, JHEP **0605**, 026 (2006) doi:10.1088/1126-6708/2006/05/026 arXiv:[hep-ph/0603175].
- [86] T. Sjostrand *et al.*, “An Introduction to PYTHIA 8.2”, Comput. Phys. Commun. **191**, 159 (2015) doi:10.1016/j.cpc.2015.01.024 arXiv:1410.3012 [hep-ph].
- [87] P. Nason, “A New method for combining NLO QCD with shower Monte Carlo algorithms”, JHEP **0411**, 040 (2004) doi:10.1088/1126-6708/2004/11/040 arXiv:[hep-ph/0409146].
- [88] S. Frixione, P. Nason and C. Oleari, “Matching NLO QCD computations with Parton Shower simulations: the POWHEG method”, JHEP **0711**, 070 (2007) doi:10.1088/1126-6708/2007/11/070 arXiv:0709.2092 [hep-ph].
- [89] S. Alioli, P. Nason and C. Oleari *et al.*, “A general framework for implementing NLO calculations in shower Monte Carlo programs: the POWHEG BOX”, JHEP **1006**, 043 (2010) doi:10.1007/JHEP06(2010)043 arXiv:1002.2581 [hep-ph].
- [90] S. Alioli, P. Nason and C. Oleari *et al.*, “NLO vector-boson production matched with shower in POWHEG”, JHEP **0807**, 060 (2008) doi:10.1088/1126-6708/2008/07/060 arXiv:0805.4802 [hep-ph].
- [91] [GEANT4 Collaboration], “GEANT4: A Simulation toolkit”, Nucl. Instrum. Meth. A **506**, 250 (2003) doi:10.1016/S0168-9002(03)01368-8.
- [92] J. Allison *et al.*, “Geant4 developments and applications”, IEEE Trans. Nucl. Sci. **53**, 270 (2006) doi:10.1109/TNS.2006.869826.
- [93] CMS Collaboration, “The fast simulation of the CMS detector at LHC”, J. Phys. Conf. Ser. **331**, 032049 (2011) doi:10.1088/1742-6596/331/3/032049

-
- [94] K. Rose, “Deterministic annealing for clustering, compression, classification, regression, and related optimization problems”, *Proceedings of the IEEE* **86** 2210 (1998) doi:10.1109/5.726788.
- [95] CMS Collaboration, “Energy Calibration and Resolution of the CMS Electromagnetic Calorimeter in pp Collisions at $\sqrt{s} = 7$ TeV”, *JINST* **8**, P09009 (2013) doi:10.1088/1748-0221/8/09/P09009 arXiv:1306.2016 [hep-ex].
- [96] CMS Collaboration, “Performance of Electron Reconstruction and Selection with the CMS Detector in Proton-Proton Collisions at $s = 8$ TeV”, *JINST* **10**, no. 06, P06005 (2015) doi:10.1088/1748-0221/10/06/P06005 arXiv:1502.02701 [physics.ins-det].
- [97] R. Fruhwirth, “Application of Kalman filtering to track and vertex fitting”, *Nucl. Instrum. Meth. A* **262**, 444 (1987) doi:10.1016/0168-9002(87)90887-4.
- [98] H. Bethe and W. Heitler, “On the Stopping of fast particles and on the creation of positive electrons”, *Proc. Roy. Soc. Lond. A* **146**, 83 (1934) doi:10.1098/rspa.1934.0140.
- [99] T. Speer, R. Fruhwirt, “A Gaussian-sum filter for vertex reconstruction”, *Computer Physics Communications* **174** 935 (2006) doi:10.1016/j.cpc.2006.01.005.
- [100] CMS Collaboration, “Energy smearing and scale correction”, URL: <https://twiki.cern.ch/twiki/bin/viewauth/CMS/EGMSmearer> (visited on 2016-02-18).
- [101] CMS Collaboration, “Particle-Flow Event Reconstruction in CMS and Performance for Jets, Taus, and MET”, CMS-PAS-PFT-09-001.
- [102] CMS Collaboration, “Commissioning of the Particle-flow Event Reconstruction with the first LHC collisions recorded in the CMS detector”, CMS-PAS-PFT-10-001.

- [103] M. Cacciari and G. P. Salam, “Pileup subtraction using jet areas”, *Phys. Lett. B* **659**, 119 (2008) doi:10.1016/j.physletb.2007.09.077 arXiv:0707.1378 [hep-ph].
- [104] M. Cacciari, G. P. Salam and G. Soyez, “The Catchment Area of Jets”, *JHEP* **0804**, 005 (2008) doi:10.1088/1126-6708/2008/04/005 arXiv:0802.1188 [hep-ph].
- [105] M. Cacciari, G. P. Salam and G. Soyez, “FastJet User Manual”, *Eur. Phys. J. C* **72**, 1896 (2012) doi:10.1140/epjc/s10052-012-1896-2 arXiv:1111.6097 [hep-ph].
- [106] M. Cacciari, G. P. Salam and G. Soyez, “The Anti-k(t) jet clustering algorithm”, *JHEP* **0804**, 063 (2008) doi:10.1088/1126-6708/2008/04/063 arXiv:0802.1189 [hep-ph].
- [107] CMS Collaboration, “CMS computing : Technical Design Report”, CERN-LHCC-2005-023 <https://cds.cern.ch/record/838359>.
- [108] I. Bird *et al.*, “LHC computing Grid : Technical Design Report”, CERN-LHCC-2005-024 <http://cds.cern.ch/record/840543>.
- [109] CMS Collaboration, “Standard Model Cross Sections for CMS at 13 TeV”, <https://twiki.cern.ch/twiki/bin/viewauth/CMS/StandardModelCrossSectionsat13TeV> (visited on 2017-08-17).
- [110] CMS Collaboration, “Cut Based Electron ID for Run 2”, <https://twiki.cern.ch/twiki/bin/view/CMS/CutBasedElectronIdentificationRun2> (visited on 2015-12-22).
- [111] CMS Collaboration, “Baseline muon selections for Run-II”, <https://twiki.cern.ch/twiki/bin/view/CMS/SWGuideMuonIdRun2> (visited on 2016-07-04).

- [112] R. Gavin, Y. Li, F. Petriello and S. Quackenbush, “FEWZ 2.0: A code for hadronic Z production at next-to-next-to-leading order”, *Comput. Phys. Commun.* **182**, 2388 (2011) doi:10.1016/j.cpc.2011.06.008 arXiv:1011.3540 [hep-ph].
- [113] A. V. Manohar, P. Nason and G. P. Salam, “The Photon Content of the Proton”, *JHEP* **1712**, 046 (2017) doi:[https://doi.org/10.1007/JHEP12\(2017\)046](https://doi.org/10.1007/JHEP12(2017)046) arXiv:1708.01256 [hep-ph].
- [114] D. Bourilkov, “Photon-induced Background for Dilepton Searches and Measurements in pp Collisions at 13 TeV”, arXiv:1606.00523 [hep-ph].
- [115] V. Blobel, “An Unfolding method for high-energy physics experiments”, arXiv:hep-ex/0208022.
- [116] G. D’Agostini, “A Multidimensional unfolding method based on Bayes’ theorem”, *Nucl. Instrum. Meth. A* **362**, 487 (1995) doi:10.1016/0168-9002(95)00274-X.
- [117] CMS Collaboration, “Measurement of the Inclusive W and Z Production Cross Sections in pp Collisions at $\sqrt{s} = 7$ TeV”, *JHEP* **1110**, 132 (2011) doi:10.1007/JHEP10(2011)132 arXiv:1107.4789 [hep-ex].
- [118] CMS Collaboration, “Details of the Tag and Probe procedure for Egamma”, <https://twiki.cern.ch/twiki/bin/viewauth/CMS/ElectronScaleFactorsRun2> (visited on 2016-06-26).
- [119] CMS Collaboration, “CMS Luminosity Measurement for the 2015 Data Taking Period”, CMS-PAS-LUM-15-001.
- [120] CMS Collaboration, “Energy smearing and scale correction”, <https://twiki.cern.ch/twiki/bin/viewauth/CMS/EGMSmearer> (visited on 2018-02-14).

-
- [121] M. R. Whalley, D. Bourilkov and R. C. Group, “The Les Houches accord PDFs (LHAPDF) and LHAGLUE”, arXiv:hep-ph/0508110.
- [122] D. Bourilkov, R. C. Group and M. R. Whalley, “LHAPDF: PDF use from the Tevatron to the LHC”, arXiv:hep-ph/0605240.
- [123] A. Buckley, J. Ferrando and S. Lloyd *et al.*, “LHAPDF6: parton density access in the LHC precision era”, Eur. Phys. J. C **75**, 132 (2015) doi:10.1140/epjc/s10052-015-3318-8 arXiv:1412.7420 [hep-ph].
- [124] E. Barberio and Z. Was, “PHOTOS: A Universal Monte Carlo for QED radiative corrections. Version 2.0”, Comput. Phys. Commun. **79**, 291 (1994) doi:10.1016/0010-4655(94)90074-4.
- [125] A. Valassi, “Combining correlated measurements of several different physical quantities”, Nucl. Instrum. Meth. A **500**, 391 (2003) doi:10.1016/S0168-9002(03)00329-2.
- [126] G. D. Lafferty and T. R. Wyatt, “Where to stick your data points: The treatment of measurements within wide bins”, Nucl. Instrum. Meth. A **355**, 541 (1995) doi:10.1016/0168-9002(94)01112-5.
- [127] P. B. Cushman and A. H. Heering, “CMS HCAL hybrid photodiode design and quality assurance stations”, ICFA Instrum. Bull. **25**, 1 (2002).
- [128] J. Freeman, “Silicon Photomultipliers for the CMS Hadron Calorimeter”, Nucl. Instrum. Meth. A **617**, 393 (2010), doi:10.1016/j.nima.2009.10.132.
- [129] CMS Collaboration, “Upgrade of the CMS Hadron Outer Calorimeter with SIPMs”, Phys. Procedia **37**, 72 (2012), doi:10.1016/j.phpro.2012.02.358.
- [130] CMS Collaboration, “MPPC photon sensor operational experience in CM”, Proceedings of 16th International Conference on Calorimetry in High

- Energy Physics (CALOR 2014) 587, 12022 (2015) doi:10.1088/1742-6596/587/1/012022.
- [131] CMS Collaboration, “CMS Technical Design Report for the Phase 1 Upgrade of the Hadron Calorimeter”, doi:10.2172/1151651.
- [132] PICMG, MicroTCA Specification, Technical Report MTCA.0/R1.0, (2006).
- [133] PICMG, AdvancedTCA Base Specification, Technical Report ATCA.0/R3.0, (2008).

List of Publications/Conferences

- **CMS Public Documents**

1. CMS Collaboration, “Measurement of the differential Drell-Yan cross section in proton-proton collisions at 13 TeV”, **CMS-PAS-SMP-16-009** (2016).

- **CMS Internal Documents**

- **Analysis Notes**

1. R. Chawla *et al.*, “Measurement of the differential DY cross section at $\sqrt{s} = 13$ TeV”, **CMS AN-2015/324** (2015).

- **Detector Note**

1. R. Chawla *et al.*, “Commissioning and performance of the CMS Hadron Outer Calorimeter”, **CMS DN-14-019** (2014).

- **Papers in Refreed Journals**

1. R. Chawla and M. Kaur, “Shifted Gompertz PDF for multiplicities in high energy leptonic and hadronic collisions”, arXiv:1801.00278 [hep-ph].
2. R. Chawla *et al.*, “Differential cross section measurement of the Drell-Yan process at 13 TeV proton-proton collisions with the CMS detector”, Springer Proc. Phys. **203** (2018) doi:10.1007/978-3-319-73171-1.

- **Papers presented in Conferences, Workshops and Symposiums**

1. R. Chawla *et al.*, “Precision Measurements of Drell-Yan production”, **SM@LHC 2017: Standard Model at the LHC 2017**, 2-5 May, 2017, Amsterdam, Netherlands.
2. R. Chawla *et al.*, “Drell-Yan differential cross section measurement in pp collisions with the CMS detector”, **11th Chandigarh Science Congress, CHASCON 2017**, 9-11 March, 2017, Panjab University, Chandigarh, India.
3. R. Chawla *et al.*, “Differential cross section measurement of the Drell-Yan process at 13 TeV proton-proton collisions with the CMS detector”, **XXII DAE-BRNS High Energy Physics Symposium 2016**, 12-16 December, 2016, Delhi, India.
4. R. Chawla *et al.*, “Data Certification Report ”, **CMS Week 2016**, 14-18 November, 2016, Mumbai, India.
5. R. Chawla *et al.*, “Drell-Yan Differential Cross Section Measurement at $\sqrt{s} = 13$ TeV with p-p collisions in the CMS Detector”, **International Workshop on Frontiers in Electroweak Interactions of Leptons and Hadrons**, 2-6 November, 2016, Aligarh, India.
6. R. Chawla *et al.*, “HCAL Back-End Upgradation at CMS Detector”, **9th Chandigarh Science Congress, CHASCON 2017**, 25-27 February, 2015, Panjab University, Chandigarh, India.

- **Conferences, Schools and Workshops attended**

1. **Workshop on Upgrade of the CMS Calorimeter**, 23-24 November, 2015, Tata Institute of Fundamental Research, Mumbai, India.
2. **Workshop on High Performance Computing**, 16-17 March, 2015, Panjab University, Chandigarh, India.

3. **IX SERC SCHOOL ON EXPERIMENTAL HIGH ENERGY PHYSICS**, 2-21 November, 2013, Indian Institute of Technology Madras, Chennai, India.
4. **CMS Data Analysis School (CMSDAS)**, 7-11 November, 2013, Saha Institute of Nuclear Physics, Kolkata, India.

• CMS Publications³⁵

1. CMS Collaboration, “Observation of electroweak production of same-sign W boson pairs in the two jet and two same-sign lepton final state in proton-proton collisions at $\sqrt{s} = 13$ TeV”, Phys. Rev. Lett. **120**, no. 8, 081801 (2018).
2. CMS Collaboration, “Measurement of vector boson scattering and constraints on anomalous quartic couplings from events with four leptons and two jets in proton-proton collisions at $\sqrt{s} = 13$ TeV”, Phys. Lett. B **774**, 682 (2017).
3. CMS Collaboration, “Measurement of the differential cross sections for the associated production of a W boson and jets in proton-proton collisions at $\sqrt{s} = 13$ TeV”, Phys. Rev. D **96**, no. 7, 072005 (2017).
4. CMS Collaboration, “Measurements of jet charge with dijet events in pp collisions at $\sqrt{s} = 8$ TeV”, JHEP **1710**, 131 (2017).
5. CMS Collaboration, “Measurement of the triple-differential dijet cross section in proton-proton collisions at $\sqrt{s} = 8$ TeV and constraints on parton distribution functions”, Eur. Phys. J. C **77**, no. 11, 746 (2017).
6. CMS Collaboration, “Measurements of the $pp \rightarrow W\gamma\gamma$ and $pp \rightarrow Z\gamma\gamma$ cross sections and limits on anomalous quartic gauge couplings at $\sqrt{s} = 8$ TeV”, JHEP **1710**, 072 (2017).

³⁵I am a co-author of more than 300 Journal Articles with the CMS Collaboration and the full list of publications can be found at http://inspirehep.net/search?ln=en&as=1&m1=e&p1=Ridhi+Chawla&f1=author&op1=a&m2=p&p2=&f2=collaboration&op2=a&m3=a&p3=&f3=&action_search=Search&sf=&so=d&rm=&rg=25&sc=0&of=hb

7. CMS Collaboration, “Search for anomalous couplings in boosted $WW/WZ \rightarrow \ell\nu q\bar{q}$ production in proton-proton collisions at $\sqrt{s} = 8$ TeV”, *Phys. Lett. B* **772**, 21 (2017).
8. CMS Collaboration, “Measurement of the cross section for electroweak production of $Z\gamma$ in association with two jets and constraints on anomalous quartic gauge couplings in proton-proton collisions at $\sqrt{s} = 8$ TeV”, *Phys. Lett. B* **770**, 380 (2017).
9. CMS Collaboration, “Measurement of electroweak-induced production of $W\gamma$ with two jets in pp collisions at $\sqrt{s} = 8$ TeV and constraints on anomalous quartic gauge couplings”, *JHEP* **1706**, 106 (2017).
10. CMS Collaboration, “Measurements of the associated production of a Z boson and b jets in pp collisions at $\sqrt{s} = 8$ TeV”, *Eur. Phys. J. C* **77**, no. 11, 751 (2017).
11. CMS Collaboration, “Measurements of differential production cross sections for a Z boson in association with jets in pp collisions at $\sqrt{s} = 8$ TeV”, *JHEP* **1704**, 022 (2017).
12. CMS Collaboration, “Measurements of differential cross sections for associated production of a W boson and jets in proton-proton collisions at $\sqrt{s} = 8$ TeV”, *Phys. Rev. D* **95**, 052002 (2017).
13. CMS Collaboration, “Measurement of the WZ production cross section in pp collisions at $\sqrt{s} = 7$ and 8 TeV and search for anomalous triple gauge couplings at $\sqrt{s} = 8$ TeV”, *Eur. Phys. J. C* **77**, no. 4, 236 (2017).
14. CMS Collaboration, “Measurement and QCD analysis of double-differential inclusive jet cross sections in pp collisions at $\sqrt{s} = 8$ TeV and cross section ratios to 2.76 and 7 TeV”, *JHEP* **1703**, 156 (2017).
15. CMS Collaboration, “Measurement of the production cross section of a W boson in association with two b jets in pp collisions at $\sqrt{s} = 8$ TeV”, *Eur. Phys. J. C* **77**, no. 2, 92 (2017).

-
16. CMS Collaboration, “Measurement of the ZZ production cross section and $Z \rightarrow \ell^+ \ell^- \ell'^+ \ell'^-$ branching fraction in pp collisions at $\sqrt{s}=13$ TeV”, Phys. Lett. B **763**, 280 (2016), Erratum: [Phys. Lett. B **772**, 884 (2017)].
 17. CMS Collaboration, “Measurement of the WZ production cross section in pp collisions at $\sqrt{s} = 13$ TeV”, Phys. Lett. B **766**, 268 (2017)
 18. CMS Collaboration, “Measurement of electroweak production of a W boson and two forward jets in proton-proton collisions at $\sqrt{s} = 8$ TeV”, JHEP **1611**, 147 (2016).
 19. CMS Collaboration, “Measurement of the transverse momentum spectra of weak vector bosons produced in proton-proton collisions at $\sqrt{s} = 8$ TeV”, JHEP **1702**, 096 (2017)
 20. CMS Collaboration, “Measurement of the double-differential inclusive jet cross section in protonproton collisions at $\sqrt{s} = 13$ TeV”, Eur. Phys. J. C **76**, no. 8, 451 (2016).
 21. CMS Collaboration, “Measurement of the differential cross section and charge asymmetry for inclusive $pp \rightarrow W^\pm + X$ production at $\sqrt{s} = 8$ TeV”, Eur. Phys. J. C **76**, no. 8, 469 (2016).
 22. CMS Collaboration, “Measurement of the $Z\gamma \rightarrow \nu\bar{\nu}\gamma$ production cross section in pp collisions at $\sqrt{s} = 8$ TeV and limits on anomalous ZZ γ and Z $\gamma\gamma$ trilinear gauge boson couplings”, Phys. Lett. B **760**, 448 (2016).
 23. CMS Collaboration, “Measurement of dijet azimuthal decorrelation in pp collisions at $\sqrt{s} = 8$ TeV”, Eur. Phys. J. C **76**, no. 10, 536 (2016).
 24. CMS Collaboration, “Forwardbackward asymmetry of DrellYan lepton pairs in pp collisions at $\sqrt{s} = 8$ TeV”, Eur. Phys. J. C **76**, no. 6, 325 (2016).
 25. CMS Collaboration, “Measurement of the inclusive jet cross section in pp collisions at $\sqrt{s} = 2.76$ TeV”, Eur. Phys. J. C **76**, no. 5, 265 (2016).
 26. CMS Collaboration, “Measurement of the W^+W^- cross section in pp collisions

- at $\sqrt{s} = 8$ TeV and limits on anomalous gauge couplings”, *Eur. Phys. J. C* **76**, no. 7, 401 (2016).
27. CMS Collaboration, “Comparison of the $Z/\gamma + \text{jets}$ to $\gamma + \text{jets}$ cross sections in pp collisions at $\sqrt{s} = 8$ TeV”, *JHEP* **1510**, 128 (2015), Erratum: [*JHEP* **1604**, 010 (2016)].
28. CMS Collaboration, “Search for a pseudoscalar boson decaying into a Z boson and the 125 GeV Higgs boson in $^+ b\bar{b}$ final states”, *Phys. Lett. B* **748**, 221 (2015).
29. CMS Collaboration, “Search for a Higgs boson in the mass range from 145 to 1000 GeV decaying to a pair of W or Z bosons”, *JHEP* **1510**, 144 (2015).
30. CMS Collaboration, “Search for Third-Generation Scalar Leptoquarks in the $t\tau$ Channel in Proton-Proton Collisions at $\sqrt{s} = 8$ TeV”, *JHEP* **1507**, 042 (2015), Erratum: [*JHEP* **1611**, 056 (2016)].